ANL-NE-08/13

Argonne NATIONAL LABORATORY

MONTE CARLO MODELING AND ANALYSES OF YALINA-BOOSTER SUBCRITICAL ASSEMBLY PART 1: ANALYTICAL MODELS AND MAIN NEUTRONICS PARAMETERS

Nuclear Engineering Division

About Argonne National Laboratory

Argonne is a U.S. Department of Energy laboratory managed by UChicago Argonne, LLC under contract DE-AC02-06CH11357. The Laboratory's main facility is outside Chicago, at 9700 South Cass Avenue, Argonne, Illinois 60439. For information about Argonne, see www.anl.gov.

Availability of This Report

This report is available, at no cost, at http://www.osti.gov/bridge. It is also available on paper to the U.S. Department of Energy and its contractors, for a processing fee, from:

U.S. Department of Energy
Office of Scientific and Technical Information
P.O. Box 62
Oak Ridge, TN 37831-0062
phone (865) 576-8401
fax (865) 576-5728
reports@adonis.osti.gov

ANL-NE-08/13

MONTE CARLO MODELING AND ANALYSES OF YALINA-BOOSTER SUBCRITICAL ASSEMBLY PART 1: ANALYTICAL MODELS AND MAIN NEUTRONICS PARAMETERS

by
Alberto Talamo and M. Yousry Gohar
Nuclear Engineering Division, Argonne National Laboratory

work sponsored by
The Office of Globaql Nuclear Material Threat Reduction
US Department of Energy
Under Contract DE-AC02-06CH11357

UChicago ▶ Argonne LLC

Office of Science U.S. DEPARTMENT OF ENERGY

A U.S. Department of Energy laboratory managed by UChicago Argonne, LLC

March 2008 ANL-NE-08/13

MONTE CARLO MODELING AND ANALYSES OF YALINA-BOOSTER SUBCRITICAL ASSEMBLY PART I: ANALYTICAL MODELS AND MAIN NEUTRONICS PARAMETERS

By

Alberto Talamo and Yousry Gohar

Nuclear Engineering Division
Argonne National Laboratory
9700 South Cass Avenue
Argonne, IL 60439

Work supported by the
Office of Global Nuclear Material Threat Reduction
U.S. Department of Energy
Under Contract W-31-109-Eng-38

Table of Contents

List of Figures

List of Tables

Table No. Page

MONTE CARLO MODELING AND ANALYSES OF YALINA-BOOSTER SUBCRITICAL ASSEMBLY PART I: ANALYTICAL MODELS AND MAIN NEUTRONICS PARAMETERS

Abstract

This study was carried out to model and analyze the YALINA-Booster facility, of the Joint Institute for Power and Nuclear Research of Belarus, with the long term objective of advancing the utilization of accelerator driven systems for the incineration of nuclear waste. The YALINA-Booster facility is a subcritical assembly, driven by an external neutron source, which has been constructed to study the neutron physics and to develop and refine methodologies to control the operation of accelerator driven systems. The external neutron source consists of Californium-252 spontaneous fission neutrons, 2.45 MeV neutrons from Deuterium-Deuterium reactions, or 14.1 MeV neutrons from Deuterium-Tritium reactions. In the latter two cases a deuteron beam is used to generate the neutrons. This study is a part of the collaborative activity between Argonne National Laboratory (ANL) of USA and the Joint Institute for Power and Nuclear Research of Belarus. In addition, the International Atomic Energy Agency (IAEA) has a coordinated research project benchmarking and comparing the results of different numerical codes with the experimental data available from the YALINA-Booster facility and ANL has a leading role coordinating the IAEA activity.

The YALINA-Booster facility has been modeled according to the benchmark specifications defined for the IAEA activity without any geometrical homogenization using the Monte Carlo codes MONK and MCNP/MCNPX/MCB. The MONK model perfectly matches the MCNP one. The computational analyses have been extended through the MCB code, which is an extension of the MCNP code with burnup capability because of its additional feature for analyzing source driven multiplying assemblies. The main neutronics parameters of the YALINA-Booster facility were calculated using these computer codes with different nuclear data libraries based on ENDF/B-VI-0, -6, JEF-2.2, and JEF-3.1.

MONTE CARLO MODELING AND ANALYSES OF YALINA-BOOSTER SUBCRITICAL ASSEMBLY PART I: ANALYTICAL MODELS AND MAIN NEUTRONICS PARAMETERS

1. Introduction

YALINA-Booster is an Accelerator Driven System (ADS) consisting of a subcritical assembly driven by an external neutron source. The ADS concept has been proposed by Bowman et al.[1] in 1992 for transmuting the transuranics and the long-lived fission products of the spent nuclear fuel from Light Water Reactors (LWRs). Within this concept, the incineration of LWRs waste takes advantage of the low capture to fission ratio of transuranic isotopes in the fast energy spectrum. The ADS utilization for energy production has been suggested by Rubbia et al.[2] The ADS experimental research has been performed with small research facilities around the world such as MASURCA,[3] TRADE,[4] and YALINA.[5] The present study is focused on characterizing the YALINA-Booster facility as defined in the IAEA benchmark specifications.[5] The analyses include the calculation of the multiplication factor and the main neutronics parameters, such as the effective delayed neutron fraction (β_{eff}), the prompt neutron lifetime (l_p), and generation time (Λ). The YALINA-Booster subcritical research facility[5-6] of Belarus has been investigated by two Monte Carlo codes. MONK9a,[7-8] which is used for licensing nuclear power plants in the United Kingdom and MCNP/MCNPX/MCB,[9-16] which is used all over the world for analyzing nuclear facilities and benchmarking other transport codes. The YALINA-Booster facility has been modeled in details without any geometrical approximation as defined in the IAEA benchmark specifications.[5]

2. The YALINA-Booster Facility

The YALINA-Booster facility has been constructed at the Joint Institute for Power and Nuclear Research SOSNY of Belarus. It is a subcritical assembly driven by an external neutron source. The facility has no active cooling system and it consists of four concentric square zones: a target zone with a side of 8 cm, an inner fast zone with a side of 16.4 cm, an outer fast zone with a side of 49 cm, and a thermal zone with a side of 98 cm. The inner fast zone has high enriched metallic uranium fuel rods with 90% by weight ^{235}U, the outer fast zone contains uranium oxide fuel rods with 36% ^{235}U enrichment, and the thermal zone uses uranium oxide fuel rods with 10% ^{235}U enrichment (EK-10 fuel type). In-between the outer fast and the thermal zones it resides a thermal neutron absorber zone composed of two concentric square shells. The first square shell has natural uranium rods and the second one has natural boron carbide rods. These two absorber shells allow fast neutrons to stream from the fast to the thermal zone but they reduce the opposite streaming because of the high (n,α) thermal cross section of ^{10}B and the epithermal capture resonances of ^{238}U. This assembly configuration is referred as “booster”, since it is composed of an inner fast zone, around the central target, and an outer thermal zone.[17] The matrix material of the fast zones is lead, whereas the thermal zone moderator is polyethylene. The assembly is surrounded by a radial graphite reflector

with a height of 60 cm and a width of 25 cm. In the thermal and the fast zones, a stainless steel grid with a thickness of 0.4 cm and a width of 24 cm, holds the lead and the polyethylene matrix blocks; the steel grid continues in the axial reflectors. At the top and the bottom of all fuels rods, borated polyethylene reflector is used. Along the fuel rods length, half of the target zone has pure lead and the other half accommodates the copper disk, which contains deuterium or tritium for producing Deuterium-Deuterium or Deuterium-Tritium neutrons, the vacuum beam tube, the water cooling channel, and the stainless steel structures. The copper disk of the target is located at the center of the active fuel length, which is 50 cm. The subcritical assembly has ten experimental channels and six measurement channels. The experimental channels are distributed as follows: four channels in the fast zone and three channels in the thermal and reflector zones. The measurements channels are also distributed: two channels in the thermal zone and four channels in the moderator zone. A further detailed description of the YALINA-Booster facility can be found in the IAEA benchmark specifications.[5] As indicated in the benchmark specifications, two configurations of the YALINA-Booster have been considered, which differ only in the number of fuel rods in the thermal zone, 1141 versus 902.

Figures 1 to 4 give three dimensional overviews of the YALINA-Booster facility by the MONK visualization software VISTA-RAY. In these figures, the correspondence between materials and colors is: yellow for air, light-green for borated polyethylene, green for stainless steel, blue for organic glass, gray for iron, light-blue for graphite, purple for polyethylene, pink for lead, and white for polystyrene. Figures 5 to 20 illustrate the details of the YALINA-Booster assembly by the MONK visualization software VISAGE. In these figures, the correspondence between materials and colors is: yellow for air, pale-green for borated polyethylene, light-green for stainless steel, gold for organic glass, red for iron, light-blue for water, purple for polyethylene, pink for lead, blue for the 90% enriched uranium, steel-blue for the 36% enriched uranium, khaki or black for the 10% enriched uranium, green for natural uranium, orange for boron carbide (fast zone) or copper (target zone), brown for polyethylene, magenta for lead (target zone), wheat for graphite, and dark-magenta for aluminum alloy. Figure 5 labels the experimental channels. Figures 21 to 30 show the YALINA-Booster as modeled by MCNP. Both, the MONK and the MCNP models reflect the IAEA benchmark specifications without any geometrical approximation.

Most of the materials utilized in the YALINA-Booster contain many impurities that impact the multiplication factor of the assembly and need to be taken into consideration. In the ENDF/B nuclear data library of MCNP/MCNPX, all nuclides indicated in the IAEA benchmark are available, with exception of ^{204}Pb, which has been modeled as ^{207}Pb since their cross sections are similar as shown in Appendix A. In addition, natural Ba has been modeled as ^{138}Ba. The ^{204}Pb isotope is available in the JEF-2.2 nuclear data library, which has been used for the MCB calculations. However, the nuclear library based on JEF-2.2 does not have the updated S(α,β) scattering function of 2002. This update is available in the library based on ENDF/B-VI for MCNPC4c3, MCNP5, and MCNPX2.6. The cross sections of most of the impurities are available in the MONK nuclear data libraries BINGO, DICE or WIMS. Appendix A gives the material approximations that have been assumed in the different set of MONK simulations. The BINGO nuclear data library is missing ^{75}As, ^{209}Bi, ^{204}Pb, ^{66}Zn, ^{67}Zn, ^{68}Zn, and ^{70}Zn. The DICE nuclear data library is missing: ^{75}As, ^{204}Pb and the scattering function S(α,β) of graphite. The WIMS nuclear data library is

missing ^{75}As, ^{209}Bi, ^{204}Pb, and Sb; moreover, carbon isotope is always treated as carbon bounded in graphite and hydrogen as hydrogen bounded in water.

3. MONK9a versus MCNP5/MCNPX

The Monte Carlo code MONK has been developed by SERCO Assurance and British Nuclear Fuel and it is one of the neutron transport codes used for licensing nuclear power plants in United Kingdom. The code can be used with a continuous energy nuclear data library (BINGO) based on JEF-2.2, a 13193 energy groups library (DICE) based on JEF-2.2, ENDF/B-VI or JENDL-2, or a 172 energy groups WIMS nuclear data library. The latter library is also available in a more compact form using 69 energy groups structure; this latter version has never been used in the present analyses. The major differences between MONK and MCNP/MCNPX include the following:

- MONK can only transport neutrons; MCNP can transport neutrons, electrons, and photons; MCNPX can transport over 34 different types of particles at energies lower and higher than 20 MeV.
- MCNP/MCNPX is designed for parallel platforms in distributed memory systems (PVM and MPI) or in shared memory systems (OPENMP); MONK runs only on single processor.
- MONK can perform burnup calculations; the burnup capability has been embedded in MCNPX by integrating CINDER90 computer code package. In both cases, the burnup is limited to a fission neutron source and it is not applicable to an accelerator driven system.
- MONK can efficiently describe complicated geometries by the Woodcock tracking capability referred to as hole geometry.
- MONK takes advantage of the neutron superhistory variance reduction technique. MCNP/MCNPX takes advantage of the space/energy/time weight window variance reduction technique.
- MONK can calculate the external source neutron multiplication factor (k_{src}) for a subcritical assembly. The calculation of k_{src} for a subcritical core in MCNP/MCNPX is possible only by processing the neutron weight summary table or by tallying the secondary neutrons.
- MCNP/MCNPX can solve time dependent transport problems.
- MCNP/MCNPX can calculate the prompt multiplication factor for a critical core by suppressing the generation of delayed neutrons.
- MONK can define a material mixture as a composition of the previously defined materials.
- MONK allows the utilization of symbolic parameters and math expressions.
- MCNP/MCNPX can superimpose an arbitrary mesh to the geometrical model for tallying and variance reduction purposes.
- For three dimensional visualizations, MONK has VISTA-RAY graphical packages while MCNP/MCNPX requires external software packages.

The majority of deterministic and Monte Carlo nuclear codes utilize the power iteration technique for numerical criticality searches.[18-19] Within this technique the neutron transport

equation is solved according to the scheme illustrated in equations 1-7, where *h* is the power iteration index and the other symbols follow the nomenclature of Duderstadt and Hamilton of Reference 18. The MONK superhistory algorithm[20] follows several generations instead of one as the ordinary power iteration method implemented in MCNP/MCNPX before recalculating the new angular flux, as shown in equation 8 for superhistory equal to L.[21] The convergence rate of the superhistory algorithm of MONK is the same as the ordinary power iteration method of MCNP because there are fewer iterations but a larger number of generations per iteration.[22] The superhistory algorithm reduces the correlation between the iterations, that accelerates the neutron source convergence[8] and reduces the number of normalizations when calculating the error between the flux at iteration *h*+1 and *h*.

$$\vec{\Omega}\cdot\vec{\nabla}\varphi(\vec{r},\vec{\Omega},E)+\Sigma_t(\vec{r},E)\varphi(\vec{r},\vec{\Omega},E)=\int_0^{E_{\max}}dE'\int_{4\pi}d\vec{\Omega}'\Sigma_s(\vec{r},\vec{\Omega}'\to\vec{\Omega},E'\to E)\varphi(\vec{r},\vec{\Omega}',E')+$$

$$+\chi(\vec{r},E)\int_0^{E_{\max}}dE'\left(\frac{\nu(\vec{r},E')}{k_{eff}}\right)\Sigma_f(\vec{r},E')\int_{4\pi}d\vec{\Omega}'\varphi(\vec{r},\vec{\Omega}',E') \qquad (1)$$

$$\hat{L}\varphi(\vec{r},\vec{\Omega},E)\equiv\vec{\Omega}\cdot\vec{\nabla}\varphi(\vec{r},\vec{\Omega},E)+\Sigma_t(\vec{r},E)\varphi(\vec{r},\vec{\Omega},E) \qquad (2)$$

$$\hat{S}\varphi(\vec{r},\vec{\Omega},E)\equiv\int_0^{E_{\max}}dE'\int_{4\pi}d\vec{\Omega}'\Sigma_s(\vec{r},\vec{\Omega}'\to\vec{\Omega},E'\to E)\varphi(\vec{r},\vec{\Omega}',E') \qquad (3)$$

$$\hat{F}\varphi(\vec{r},\vec{\Omega},E)\equiv\chi(\vec{r},E)\int_0^{E_{\max}}dE'\nu(\vec{r},E')\Sigma_f(\vec{r},E')\int_{4\pi}d\vec{\Omega}'\varphi(\vec{r},\vec{\Omega}',E') \qquad (4)$$

$$\hat{L}\varphi(\vec{r},\vec{\Omega},E)=\hat{S}\varphi(\vec{r},\vec{\Omega},E)+\frac{1}{k_{eff}}\hat{F}\varphi(\vec{r},\vec{\Omega},E) \qquad (5)$$

$$\varphi(\vec{r},\vec{\Omega},E)=\frac{1}{k_{eff}}\left(\hat{S}-\hat{L}\right)^{-1}\hat{F}\varphi(\vec{r},\vec{\Omega},E)=\frac{1}{k_{eff}}\hat{A}\varphi(\vec{r},\vec{\Omega},E) \qquad (6)$$

$$\text{MCNP}\qquad\left[\varphi(\vec{r},\vec{\Omega},E)\right]^{h+1}=\frac{1}{\left[k_{eff}\right]^h}\hat{A}\left[\varphi(\vec{r},\vec{\Omega},E)\right]^h \qquad (7)$$

$$\text{MONK (L = } \textit{Superhistory}\text{)}\qquad\left[\varphi(\vec{r},\vec{\Omega},E)\right]^{h+1}=\frac{1}{\left\{\left[k_{eff}\right]^h\right\}^L}\hat{A}^L\left[\varphi(\vec{r},\vec{\Omega},E)\right]^h \qquad (8)$$

4. MCB2β versus MCNP5/MCNPX

The Monte Carlo Continuous Energy Burnup Code (MCB) is an extension of the MCNP4c3 code with burnup capability. The MCB input is the same as MCNP with exceptions of few more lines for the burnup calculation. At present, MCB is the only Monte Carlo code that can perform burnup of a subcritical system driven by an external neutron source. Version 2β of MCB does burnup and transmutation for the selected materials and updates their number densities at each time step. In this process, MCB calculates for each MCNP cell that contains a burnable or transmutable material the neutron flux and the isotopic reaction rates. From this information, MCB calculates the

fission product distributions, decay heat, transmutation rates, and material radiotoxicity. Since MCB performs only neutron transport, the neutron KERMA factors were modified to include the energy of the generated photons. This modification assumes that the generated photons are absorbed at the generation sites. In the present work, the MCB2β code has been only used with JEF-2.2 nuclear data library for calculating k_{src} and the prompt neutron lifetime l_p using its capability to define material mixtures.

5. Multiplication Factor, Delayed Neutron Fraction and Neutron Prompt Lifetime

The obtained results for the neutron multiplication factor, delayed neutron fraction, prompt neutron lifetime and generation time for the 1141 YALINA-Booster configuration are given in Table I. The calculated effective neutron multiplication factor (k_{eff}) of 0.97972 differs only 220 pcm from the recent experimental measurements, which represents a factor 10 improvement relative to similar published results.[6] The MCNP multiplication factor results with ^{204}Pb isotope represented as ^{206}Pb or ^{207}Pb are within the statistical error. The k_{eff} results from the MCNP code version 5 and 4c3 agree with the result from the MCNPX code within the statistical error. In MCNP4c3, the utilization of the ENDF/B-VI.0 nuclear data library instead of ENDF/B-VI.6 increases k_{eff} by about 100 pcm. The utilization of JEFF-3.1 nuclear data library instead of ENDF/B-VI.6 produces similar k_{eff} value.

The delayed neutron fraction β_{eff} has been calculated with the one run method (one simulation by a modified version of MCNP4c3[23]) and with the two runs method (two simulations, one with and one without delayed neutrons). In the latter case, the β_{eff} uses equation 9:

$$\beta_{eff} = \frac{k_{eff} - k_{prompt}}{k_{eff}} \qquad (9)$$

In the analyses, MCNP4c3, MCNP5, and MCNPX always used the same nuclear data library. The delayed neutron fraction β_{eff} obtained by the two runs method is 760 pcm, which is consistent with the value obtained by the one run method which tallies the delayed neutrons during the neutron transport process simulated by MCNP4c3.[23]

Assuming steady state and (n,xn) reactions included in the absorption term of the neutron transport equation with negative sign, the neutron multiplication factor of a subcritical assembly driven by an external neutron source can be expressed as the ratio between the secondary fission neutrons and the secondary fission neutrons plus the source neutrons.[24] k_{src} can be higher or smaller than k_{eff} depending on the spatial distribution and the energy spectrum of the neutron source. If the neutron source is placed in a high neutron importance region, then k_{src} is higher than k_{eff}, because more secondary neutrons are produced. In YALINA-Booster, the neutron source is placed at the center of the assembly to enhance its utilization, which results in k_{src} higher than k_{eff}. If the neutron source is placed in a low neutron importance zone, due to the physical location relative to the fuel assemblies or to high neutron absorber materials, then k_{src} value can be smaller than k_{eff}. The previous situation occurs for the subcritical Gas Turbine - Modular Helium Reactor, if

the neutron source is placed at the center of the inner reflector.[25] Within the framework developed by Cetnar and Gudowski,[24] the k_{src} can be expressed and evaluated by equation 10:

$$k_{src} = \frac{\iiint_V d\vec{r} \int dE \nu \Sigma_f(\vec{r},E)\Phi(\vec{r},E)}{\iiint_V d\vec{r} \int dE \nu \Sigma_f(\vec{r},E)\Phi(\vec{r},E) + \iiint_V d\vec{r} \int dE S(\vec{r},E)} \qquad (10)$$

where ν is the number of secondary neutron per fission event, Σ_f the macroscopic fission cross section, V the assembly volume, Φ the neutron flux and S the external (time-independent) neutron source. In MCNPX, all results are normalized per source particle, D-D or D-T neutron. Therefore the latter integral at denominator of equation 10 is equal to 1. The MCNPX calculation of the numerator integral of equation 10 can be performed by two independent methods. The first method uses the results of the weight summary table of MCNPX. The second method uses the F4 tally for all the fissionable materials to get the total number of fission neutrons in the fuel with the F4 tally volume set to unity. Both methods give the same results. For the D-D and D-T neutron sources, k_{src} is 700 and 1200 pcm larger than k_{eff}, respectively.

The theoretical definition of the kinetic parameters of ADS has been rigorously deduced by Cacuci.[27] The solution of the adjoint equation by Cacuci avoids the steady state assumption for the ADS,[28] required for the traditional perturbation theory as applied to critical nuclear reactors. Recent studies of the dynamic parameters for thermal driven systems and critical fission cores show that when the adjoint neutron flux is used as a weighting function, the calculated parameters match the experimental measurements.[29] The method illustrated in equations 11-15 for calculating the neutron prompt lifetime does not require the explicit evaluation of the adjoint flux.[30] The method is based on the insertion of a 1/v neutron absorber, such as ^{10}B, and on traditional perturbation theory, which can be rigorously applied only to critical reactors; however, the YALINA-Booster assembly operates close to the critical state. The method illustrated in equations 11-15 cannot be applied to a fast gas reactor because the boron (n,α) potential scattering cross section (2.7 b at 0.1 MeV) competes with the scattering cross section of helium and that softens the neutron spectrum.

$$\frac{k_{eff} - k_{eff}^B}{k_{eff}^B} = k_{eff} \frac{\iiint_V d\vec{r} \int dE \Phi^+(\vec{r},E)\partial\Sigma_a^B(E)\Phi(\vec{r},E)}{\iiint_V d\vec{r} \int dE \Phi^+(\vec{r},E)\chi(E)\int dE' \nu\Sigma_f(E')\Phi(\vec{r},E')} \qquad (11)$$

$$= k_{eff} \frac{N^B \bar{\sigma}_a^B \bar{\mathrm{v}} \iiint_V d\vec{r} \int dE \Phi^+(\vec{r},E)\frac{1}{\mathrm{v}(E)}\Phi(\vec{r},E)}{\iiint_V d\vec{r} \int dE \Phi^+(\vec{r},E)\chi(E)\int dE' \nu(E')\Sigma_f(E')\Phi(\vec{r},E')} \qquad (12)$$

$$= \Lambda k_{eff} N^B \bar{\sigma}_a^B \bar{\mathrm{v}} = l_p N^B \bar{\sigma}_a^B \bar{\mathrm{v}} \qquad (13)$$

$$l_p = \lim_{N^B \to 0} \frac{k_{eff} - k_{eff}^B}{k_{eff}^B} \frac{1}{N^B \overline{\sigma}_a^B \overline{\nu}} \qquad (14)$$

$$\Lambda = \frac{l_p}{k_{eff}} \qquad (15)$$

In equations 11-15, V is the core volume, Φ^+ is the adjoint neutron flux, Φ is the neutron flux, N^B the boron concentration (small concentration and homogeneously distributed over the whole assembly), $\overline{\sigma}_a^B$ is the boron microscopic (n,α) cross section (3837 b) evaluated at the neutron speed $\overline{\nu}$ of 2200 m/s, ν the neutron speed, χ the fission spectrum, ν the number of secondary neutrons per fission event, Σ_f the fuel fission macroscopic cross section, $\partial\Sigma_a^B$ the (small) macroscopic absorption cross section of ^{10}B, k_{eff}^B the multiplication factor with boron, k_{eff} the multiplication factor without boron, Λ the prompt neutron generation time, and l_p the prompt neutron lifetime. A simple C program has been written to filter the output of the MCNPX code and prepare a new MCNPX input with 10^{-7} atoms/b·cm concentration of ^{10}B homogeneously distributed in all the assembly volume. The prompt neutron lifetime and generation time calculated by equations 14 and 15 are about 54 μs. The prompt neutron lifetime directly calculated by MCNPX,[31] which is not weighted on the adjoint neutron flux, is 72 μs.

The MONK k_{eff} value of 0.9773 is lower than the MCNPX value by 240 pcm. The use of DICE-JEF-2.2 instead DICE-ENDF/B-VI.0 for MONK increases k_{eff} by 500 pcm. In addition, the different material approximations and the different nuclear data libraries, BINGO, DICE, and WIMS based on JEF-2.2 change the k_{eff} value within a range of 200 pcm. However, BINGO-JEF-2.2 and DICE-JEF-2.2 produce similar results for k_{src}, within 120 pcm. For the DICE-ENDF/B-VI.0 nuclear data library, the MONK k_{src} is 880 and 1330 pcm larger than k_{eff} for the D-D and D-T external neutron sources, respectively. The k_{scr} values obtained with DICE- and BINGO-JEF-2.2 are higher than the corresponding values obtained with ENDF/B-VI.0 by less than 370 pcm. The WIMS-JEF-2.2 results for k_{eff} and k_{src} are higher than all the other results obtained with DICE-ENDF/B-VI.0 and different libraries based on JEF-2.2 as shown in Table I.

In order to calculate the prompt neutron lifetime and generation time, the mixture capability of the MONK code has been used to insert a 10^{-7} atoms/b·cm concentration of ^{10}B homogeneously distributed in all the assembly volume. For the 1141 configuration of the YALINA-Booster facility, the results of the MONK code using equations 14 and 15 show a neutron prompt lifetime and generation time of 48 and 49 μs, respectively.

The MCB code was utilized to perform the analyses using the continuous energy nuclear data library based on JEF-2.2. The MCB input is the same as the MCNPX one except of few extra lines required for the burnup, whenever enabled. The MCB code was used for its capability to directly calculate k_{src} for source driven systems. The obtained k_{src} is very close to the value obtained with MONK and the maximum difference is less than 120 pcm. In addition, the delayed neutron fraction was calculated with the two runs method, using MCB with JEF-2.2, and the calculated β_{eff} value is 700 pcm. The mixture capability of

MCB has been used to calculate the prompt neutron lifetime and generation time, which are equal to 60 μs.

The second YALINA-Booster configuration under consideration has 902 EK-10 fuel rods. The 902 configuration was analyzed as the 1141 and the results are summarized in Table II. The decrease of 239 EK-10 fuel rods in the thermal zone reduces the MCNPX k_{eff} down to 0.92881, 5090 pcm lower than the k_{eff} of the configuration with 1141 EK-10 fuel rods. The calculated k_{eff} values for this configuration with different MCNP versions and MCNPX with ENDF/B-VI.6 are similar within the standard deviation of the calculations. The use of ENDF/B-VI.0 instead of ENDF/B-VI.6 increases k_{eff} by 100 pcm. The delayed neutron fraction, prompt neutron lifetime and generation time are about the same as the corresponding values of the 1141 YALINA-Booster configuration, as shown in Tables I and II. For the 902 YALINA-Booster configuration, the differences between k_{eff} and k_{src}, for D-D and D-T sources, are much larger than the corresponding differences for the 1141 YALINA-Booster configuration. As the multiplication factor decreases, the neutron source impact on the subcriticality of the assembly increases. For the D-D and D-T neutron sources k_{src} values are 2750 and 4240 pcm, larger than k_{eff}, respectively. The source multiplication factor values calculated from the weight summary table of MCNPX are the same as those obtained with F4 neutron tally and both results used equation 10.

The MONK k_{eff} value of 0.92710 obtained by DICE/ENDF/B-VI.0 differs 300 and 170 pcm from the MCNP4c3/ENDF/B-VI.0 and MCNPX/ENDF/B-VI.6 values, respectively. The utilization of JEF-2.2 nuclear data library instead of ENDF/B-VI.0 increases the MONK multiplication factor by 540 pcm. For JEF-2.2, the different material approximations and the different sets of nuclear data (BINGO, DICE, and WIMS libraries) change the k_{eff} value within a range of 200 pcm.

The MONK k_{src} values with DICE nuclear data library based on ENDF/B-VI.0 are 2890 and 4350 pcm larger than k_{eff} for the D-D and D-T external neutron sources, respectively. When DICE and BINGO nuclear data libraries based on JEF-2.2 are used instead of DICE-ENDF/B-VI.0, k_{src} increases by 380 and 290 pcm for the DD and DT external neutron sources, respectively. MONK k_{src} values for D-D and D-T neutron sources with WIMS-JEF-2.2 are 300 to 930 and 170 to 1060 pcm larger than the values obtained with DICE-ENDF/B-VI.0 when the unified source specification and the source geometry unit are used, respectively. The prompt neutron lifetime and generation time calculated by MONK for the 902 YALINA-Booster configuration are similar to those obtained for the 1141 YALINA-Booster configuration.

The k_{eff} from the MCB code with the JEF-2.2 continuous energy nuclear data library is similar to the value from the MONK code with the BINGO-JEF-2.2 continuous energy nuclear data library (80 pcm difference). In addition, the k_{src} differences between the MCB and MONK values are less than 120 pcm. The kinetics parameters obtained by MCB for the 902 configuration are very similar to the obtained values for the 1141 YALINA-Booster configuration.

6. Neutron Flux Distributions and Spectra of the Experimental Channels

6. A Fission Neutron Source

The neutron flux distributions in the experimental channels of the YALINA-Booster configuration with 1141 EK-10 fuel rods were calculated with MCNPX and MONK computer codes. Both Monte Carlo codes produced similar neutron flux distributions, confirming the reliability of the two models for analyzing this configuration. MCNPX and MONK results are displayed side by side in Figures 31 and 32. The axial distributions have a cosine shape. The neutron flux values are higher in the experimental channels of the thermal zone since the neutron multiplication is higher in the thermal region. The neutron flux of the experimental channel EC7T is lower than in the other thermal experimental channels since it is located at the border of the fuel zone. Similarly, the neutron flux distributions in the experimental channels of the reflector have lower values because they are located away from the fuel rods. In addition, the reflector thickness is relatively small and therefore it has small effect on reducing the neutron leakage. The radial distribution of the EC10R experimental channel of the reflector decreases as the radial distance increases due to the neutron leakage.

Figure 33 repeats the plots of Figures 31 and 32 for the 902 YALINA-Booster configuration. The fluxes in all the experimental channels of the fast zone for the 902 YALINA-Booster configuration are higher than the corresponding fluxes for the 1141 YALINA-Booster configuration because of the benefits from the increase of the polyethylene reflector volume and the normalization of the results per fission neutron source over a smaller fuel volume. A similar effect occurs for the EC5T and EC6T experimental channels of the thermal zone. The flux in EC5T becomes higher than the one in EC6T because the latter experimental channel is much closer to the fuel zone boundary for the 902 YALINA-Booster configuration. The flux in the EC7T experimental channel is about the same for the two configurations. The flux of the experimental channels of the reflector is lower for the 902 configuration due to the smaller neutron multiplication relative to the 1141 YALINA-Booster configuration.

The neutron spectra in the experimental channels of the fast zone calculated by MONK and MCNPX computer codes are shown in Figure 34 side by side. The two codes produced very similar results. In the fast channels, the peak value of the neutron spectrum is at 0.8 MeV and it is about 5000 times higher than the value at 0.1 eV. This ratio diminishes down to 500 for the EC3B experimental channel because this channel is located next to the thermal zone and a small fraction of thermal neutrons succeed to stream into the fast zone. The neutron spectrum in the thermal and the reflector experimental channels calculated by MONK and MCNP are similar, as shown in Figure 35. In the thermal channels, the fast and the thermal peaks of the spectrum are about equal. As expected, the neutron spectrum in the experimental channels of the reflector is much softer than the neutron spectrum in the experimental channels of the thermal zone.

The standard deviation values associated with the neutron spectra of Figures 34 and 35 are shown in Figures 36 and 37, respectively. For the experimental channels of the fast zone, the statistical error in the thermal energy region is large due to the small fraction of thermal neutrons. The EC3B experimental channel has a smaller standard deviation

because it has a higher fraction of thermal neutrons, as noted before. At 0.27-0.28 and 1.12-1.14 eV, ^{235}U capture and fission cross-sections have some resonances as shown in Figure 38, which decrease the neutron population in the corresponding energy ranges and increase the associated standard deviation. As expected, the standard deviation in the experimental channels of the thermal zone is lower because thermal neutrons are more adequately sampled. The standard deviation in the experimental channels of the reflector region is higher than the one in the experimental channels of the thermal region due to the lower neutron flux intensity; especially for EC9R experimental channel since this channel is located in the middle of the graphite reflector. For MONK computer code, the statistical error is larger compared to MCNPX since the total number of neutron histories is lower than MCNP. MONK runs only on a single processor, which does not permit the use of the same number of neutron histories as MCNP.

The neutron spectra in the experimental channels and their standard deviations of the 902 YALINA-Booster configuration are shown in Figures 39 through 42. There are no significant differences with the similar results obtained for the 1141 YALINA-Booster configuration with exception of more thermal neutrons in the EC7T experimental channel.

6. B Deuterium-Deuterium External Neutron Source

The neutron spectra from the use of D-D neutron source emitting 2.45 MeV neutrons in the 1141 YALINA-Booster configuration are shown in Figure 43 for the experimental channels of the fast zone and in Figure 44 for the experimental channels of the thermal and reflector zones. All spectra resemble those obtained by a fission neutron source in Figures 34 and 35 except for the 2.45 MeV peak. The neutron spectra have been normalized to one; consequently, the neutron spectrum of the EC9R experimental channel superimposes with the spectra of the other experimental channels of the reflector. The spectrum of the EC9R experimental channel has the largest fraction of thermal neutrons because of the graphite reflector. The statistical errors associated with the previous neutron spectra are shown in Figures 45 and 46. These statistical errors are very similar to the ones obtained for the fission neutron source in Figures 36 and 37.

The neutron spectra of the 902 YALINA-Booster configuration are shown in Figures 47 through 50. The decrease in the number of EK-10 fuel rods reduces the neutron multiplication factor and this enhances the 2.45-MeV spectrum peak in the fast region. For the 902 YALINA-Booster configuration, the thermal part of the neutron spectra in the experimental channels of the fast zone exhibits a smoother profile relative to the 1141 YALINA-Booster configuration (Figure 47 versus Figure 43). This improvement results from sampling a total of 22 million neutrons instead of one million as in all other calculations. For the 902 YALINA-Booster configuration, the neutron spectra in the experimental cannels of the thermal zone are similar to the corresponding neutron spectra of the 1141 YALINA-Booster configuration with exception of the EC7T experimental channel, as previously discussed for the fission neutron source.

6. C Deuterium-Tritium External Neutron Source

The previous analyses with D-D neutron source were repeated with D-T neutron source and the results are shown in Figures 51 through 58. The previous comments for the results obtained with D-D neutron source hold also for the D-T neutron source with exception of the following key remarks:

- The spectrum peak due the external neutron source moves from 2.45 to 14.1 MeV.
- The peak due to the neutron source is visible not only in the experimental channels of the fast region but also in the experimental channels of the thermal region.
- The neutron leakage for the configurations with D-T neutron source is about 52% higher than for the configurations with D-D neutron source.

7. Reaction Rates

The reaction rates of ^{235}U, ^{3}He, ^{115}In, ^{197}Au and ^{55}Mn were calculated in the different experimental channels. The microscopic cross sections of these isotopes are plotted in Figure 59. The (n,p) cross section of ^{3}He is the largest cross section and it shows no resonances. The reaction rates of ^{115}In, ^{197}Au and ^{55}Mn are calculated by modeling the irradiation capsules and the sample holder as specified in the IAEA benchmark specifications.[5] The reaction rates of ^{3}He and ^{235}U are obtained by multiplying the flux by the microscopic cross section, therefore ignoring the self shielding effect. ^{197}Au and ^{55}Mn represent 100% of gold and magnesium elements, respectively; whereas natural indium is composed of ^{113}In (4.3% abundance) and ^{115}In (95.7% abundance). In ENDF/B-VI.6, indium data are available only for the natural element. Therefore, the reaction rate for ^{115}In isotope was approximated with the reaction rate for natural indium. This approximation generates a small error because of the low concentration of ^{113}In in the natural indium for the experimental channels of the thermal zone. For the experimental channels of the fast zone the approximation is negligible because of the similar (n,γ) cross sections of ^{113}In and ^{115}In in the fast energy range, as shown in Figure 60. The reaction rates normalized per atom and source neutron are plotted in Figures 61 through 69 for ^{3}He in EC6T; ^{235}U in EC6T, and EC2B; In in EC5T, EC6T, EC7T, and EC10R; ^{197}Au in EC6T; and ^{55}Mn in EC6T.

The reaction rates of the 1141 YALINA-Booster configuration are higher than the corresponding values for the 902 configuration because of the higher neutron multiplication factor. In addition, the reaction rates from the D-T neutron source are larger than the corresponding rates from the D-D neutron source due to a higher number of secondary neutrons per fission and (n,xn) reactions. The reaction rates in the thermal experimental channels have a cosine shape and the values follow the magnitude of the microscopic cross sections illustrated in Figure 59. In a descending order, the reaction rate ranking is ^{3}He, ^{115}In, ^{197}Au and ^{55}Mn. In addition, the spatial distributions are not symmetrical at the boundaries because the reflector zones do not have equal thicknesses. The ^{235}U fission reaction rate in the EC2B fast experimental channel shown in Figure 63 does not follow a cosine shape because of the polyethylene reflector at the boundaries.

The ^{115}In, ^{197}Au and ^{55}Mn reaction rates at the center of the EC2B experimental channel are given in Table III and they are proportional to the microscopic cross section values of Figure 59. The standard deviation associated with the reaction rates of Table III is given in Table IV. The statistical error is about 10% because this channel has a fast neutron spectrum and the majority of the reactions occur in the thermal energy range, where neutrons are not adequately sampled.

8. Conclusions

Two different geometrical models simulating the YALINA-Booster facility were developed successfully without any geometry approximation and homogenization. The two models used the MONK and MCNP/MCNPX/MCB Monte Carlo computer codes, both used for licensing nuclear power plants. MONK and MCNP are different codes with different geometrical representations, calculation methodologies, and nuclear data libraries. When both MONK and MCNP/MCNPX/MCB use the same nuclear data base, the obtained results for the independent Monte Carlo simulations show an excellent agreement. The neutron multiplication factor, the source multiplication factor, the prompt neutron lifetime, and the neutron generation time were successfully determined and compared for different YALINA-Booster configurations. Moreover, the neutron multiplication factor calculated with ENDF/B-VI and JEF-3.1 nuclear data libraries match the recent experimental measurements within a discrepancy of 200 pcm, this result reduces by a factor 10 the difference reported in previous published studies.[6]

References

[1] C. D. BOWMAN et al. Nuclear Energy Generation and Waste Transmutation Using an Accelerator-Driven Intense Thermal Neutron Source, Nuclear Instruments and Methods in Physics Research A **320**, p. 336, 1992.

[2] C. RUBBIA et al. Experimental Verification of the Concept of Energy Amplification by High Energy Induced Cascade, CERN/ISC, CERN 93-31, 1993.

[3] S. SOULE et al. Neutronic Studies in Support of Accelerator-Driven Systems: the MUSE Experiments in the MASURCA Facility, Nuclear Science and Engineering **148**, pp. 124-152, 2004.

[4] C. RUBBIA et al. Neutronic Analyses of the TRADE Demonstration Facility, Nuclear Science and Engineering **148**, pp. 103-123, 2004.

[5] V. BOURNOS et al. YALINA-Booster Benchmark Specifications for the IAEA Coordinated Research Projects on Analytical and Experimental Benchmark Analysis on Accelerator Driven Systems, and Low Enriched Uranium Fuel Utilization in Accelerator Driven Sub-Critical Assembly Systems, IAEA, 2007.

[6] C. M. PERSSON et al. Analysis of Reactivity Determination Methods in the Subcritical Experiment YALINA, Nuclear Instruments and Methods in Physics Research A **554**, pp. 374-383, 2005.

[7] Answers Software, MONK, User Guide for Version 9, 2006.

[8] N. R. SMITH, the MONK Superhistory Power Algorithm, AEA Technology plc, 1996.

[9] J. F. BRIESMEISTER. A General Monte Carlo N-Particle Transport Code, Version 4c, LANL, LA-13709-M, 2002.

[10] MCNP Team. MCNP5.1.40, LA-UR-05-8617, 2005.

[11] J. S. HENDRICKS et al. MCNPX, VERSION 2.6.B, LA-UR-06-3248, 2006.

[12] J. CETNAR et al. MCB: a Continuous Energy Monte Carlo Burnup Simulation Code, EUR 18898 EN, OECD/NEA 523, 1999.

[13] J. CETNAR et al. Simulation of Nuclide Transmutation with Monte-Carlo Continuous Energy Burnup Code (MCB1C), Proc. ADTTA Conference, Reno, USA, 2001.

[14] J. CETNAR, General Solution of Bateman Equations for Nuclear Transmutations. Annals of Nuclear Energy **33/7**, pp. 640-645 2006.

[15] A. TALAMO, W. GUDOWSKI and J. CETNAR, MCB1c2 Bug on Thermal Reactors. Annals of Nuclear Energy **33/7**, pp. 653-654 2006.

[16] A. TALAMO et al. Comparison of MONTEBURNS and MCB Monte Carlo Burnup Codes on a One-Pass Deep Burn. Annals of Nuclear Energy **33/14-15**, pp. 1176-1188, 2006.

[17] W. KLEY, Remarks Concerning the Efficiency of a Booster Neutron Source, Nuclear Instruments and Methods in Physics Research A **200**, pp. 175-178, 1981.

[18] J.J. DUDERSTADT and L.J. HAMILTON. Nuclear Reactor Analysis, John Wiley & Sons, pp. 216-218, 1976.

[19] E.E. LEWIS and W.F. MILLER, Computational Methods of Neutron Transport. American Nuclear Society, pp. 92-95, 1993.

[20] R.J. BRISSENDEN and A.R. GARLICK. Biases in the Estimation of k_{eff} and its Error by Monte Carlo Methods, Annals of Nuclear Energy **13**, pp 63-83, 1986.

[21] F. BROWN, Monte Carlo Advances and Challenges, F. Joliot/O. Hahn summer school lectures, Karlsruhe, Germany, 2005.

[22] E.M. GELBARD, Implementations of the Superhistory Method. Argonne National Laboratory, ANL/RA/CP-102252, 2000.

[23] R.K. MEULEKAMP and S.C. van der MARCK, Calculating the Effective Delayed Neutron Fraction with Monte Carlo, Nuclear Science and Engineering **152/2**, pp. 142-148, 2006.
[24] J. CETNAR and W. GUDOWSKI, Neutron Multiplication in Stationary ADS by Using Monte Carlo Techniques, AGH contribution to EURATOM project: PDS-XADS, pp. 83-88, 2005.
[25] J. ZAKOVA and A. TALAMO, Effect of Neutron Source on the Incineration of Light Water Reactors Waste by Prismatic High Temperature Reactors, ACCAPP07, Pocatello, USA, 2007.
[26] F. F. HAYWOOD, Z.G. BURSON AND H.E. BANTA, A Self-replenishing Tritium Target for Neutrons Generators, ORNL-TM-3397, 1972.
[27] D. CACUCI, On the Neutron Kinetics and Control of Accelerator Driven Systems, Nuclear Science and Engineering **148**, pp. 55-66, 2004.
[28] A. GANDINI and M. SALVATORES, The Physics of Subcritical Multiplying Systems, Journal of Nuclear Science and Technology **39**, pp. 673, 2002.
[29] B. VERBOMEN et al., Monte Carlo Calculation of the Effective Neutron Generation Time, Annals of Nuclear Energy **33**, pp. 911-916, 2006.
[30] M. M. BRETSCHER, Perturbation-Independent Methods for Calculating Research Reactor Kinetic Parameters, ANL/RERTR/TM-30, 1997.
[31] R. D. BUSCH, G.D. SPRIGGS and J.S. HENDRICKS, Definition of Neutron Lifespan and Neutron Lifetime in MCNP4b, LA-UR-97-222, 1997.

Table I. k_{eff} and β values for YALINA-Booster configuration with 1141 EK-10 fuel rods

Code	Library	Fission neutron source	D-D & fission neutron sources	D-T & fission neutron sources	β [pcm]	l_p [μs]	Λ [μs]
MCNPX2.6β	ENDF/B-VI.6	0.97972±4	-	-	760±8	-	-
MCNPX2.6β	ENDF/B-VI.6	0.97956±9	0.98683[f] 0.98690[g]	0.99148[f] 099145[g]	749±16	54±2[b] 72[c]	56±2[b] 73[c]
MCNPX2.6β	JEFF-3.1	0.98008±9	-	-	728±12	-	-
MCNP5	ENDF/B-VI.6	0.98016±9	-	-	766±18	-	-
MCNP4c3	ENDF/B-VI.6	0.98004±7	-	-	747±15 752±2[a]	-	-
MCNP4c3	ENDF/B-VI.0	0.98097±8	-	-	765±16 755±2[a]	-	-
MCB2β	JEF-2.2	0.98318±9	0.98856	0.99291	699±17	60±2	61±2
MONK9a	BINGO JEF-2.2	0.9836±20	0.9898±20[e]	0.9932±20[e]	-	-	-
MONK9a	DICE JEF-2.2	0.9824±20	0.9891±20[e]	0.9931±20[e]	-	-	-
MONK9a	DICE ENDF/B-VI.0	0.9773±10	0.9861±20[e]	0.9906±20[e]	-	48±5	49±5
MONK9a	WIMS JEF-2.2	0.9844±20	0.9912±10[e] 0.9926±20[d]	0.9910±10[e] 0.9930±20[d]	-	-	-

Table I legend

a	One run method.
b	Boron concentration equal to 1e-7 atoms/b·cm^2.
c	MCNPX 1/v tally.
d	Source geometry unit.
e	Unified source specification.
f	Using the weights summary table
g	Using the secondary neutrons F4 tally

Table II. k_{eff} and β values for YALINA-Booster configuration with 902 EK-10 fuel rods

Code	Library	Fission neutron source	D-D & fission neutron sources	D-T & fission neutron sources	β [pcm]	l_p [μs]	Λ [μs]
MCNPX2.6β	ENDF/B-6.6	0.92881±4	-	-	765±8	-	-
MCNPX2.6β	ENDF/B-6.6	0.92880±8	0.95635[f] 0.95625[g]	0.97118[f] 0.97117[g]	754±18	54±2[b] 74[c]	58±2[b] 80[c]
MCNPX2.6β	JEFF-3.1	0.92862±9	-	-	739±12	-	-
MCNP5	ENDF/B-6.6	0.92913±8	-	-	761±17	-	-
MCNP4c3	ENDF-6.6	0.92918±9	-	-	764±12 762±2[a]	-	-
MCNP4c3	ENDF/B-6.0	0.93014±9	-	-	775±12 763±2[a]	-	-
MCB2β	JEF-2.2	0.93271±8	0.96061	0.97477	705±16	59±2[d]	63±2[d]
MONK9a	BINGO JEF-2.2	0.93350±20	0.96000±30[e]	0.97350±20[e]	-	-	-
MONK9a	DICE JEF-2.2	0.93250±20	0.95980±30[e]	0.97350±20[e]	-	-	-
MONK9a	DICE ENDF/B-6.0	0.92710±20	0.95600±30[e]	0.97060±20[e]	-	49±5[d]	53±5[d]
MONK9a	WIMS JEF-2.2	0.93460±20	0.96280±20[e] 0.96910±20[d]	0.96290±20[e] 0.97180±20[d]	-	-	-

Table II legend

A	One run method.
B	Boron concentration equal to 1e-7 atoms/b·cm^2.
C	MCNPX 1/v tally.
D	Source geometry unit.
E	Unified source specification.
F	Using the weights summary table
G	Using the secondary neutrons F4 tally

Table III. (n,γ) reaction rates in the EC2B experimental channel for different YALINA-Booster configurations

	1141		902	
	DD	DT	DD	DT
^{197}Au	0.00838	0.011099	0.002509	0.004987
In	0.00877	0.01454	0.004626	0.006641
^{55}Mn	0.000416	0.000771	0.000153	0.000282

Table IV. (n,γ) reaction rate standard deviations [%] in the EC2B experimental channel for different YALINA-Booster configurations

	1141		902	
	DD	DT	DD	DT
^{197}Au	9.73	11.66	8.09	6.62
In	8.18	9.07	9.78	8.61
^{55}Mn	8.06	10.65	7.40	7.39

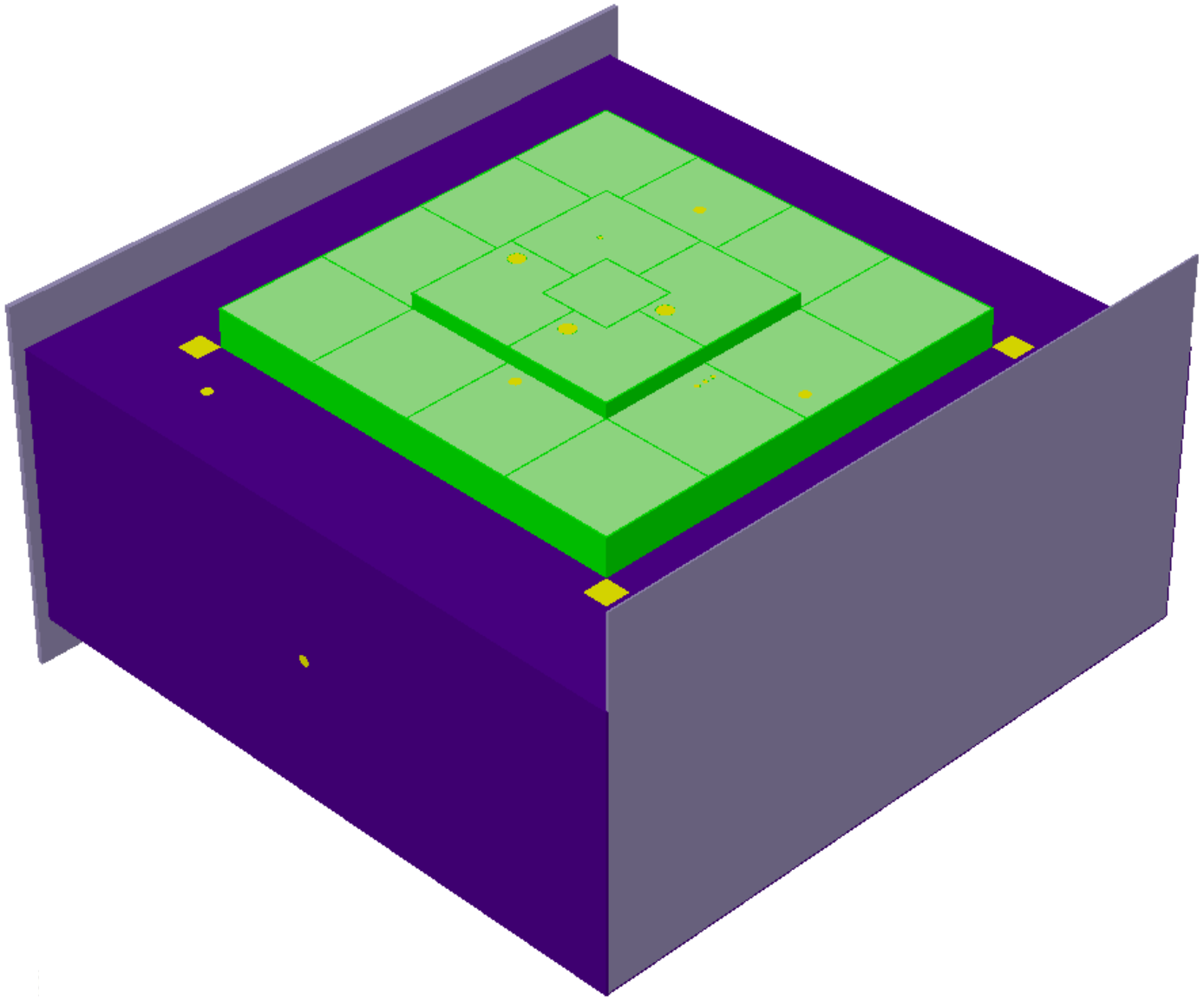

Figure 1. Three dimensional external view of the YALINA-Booster subcritical assembly plotted by VISTA-RAY

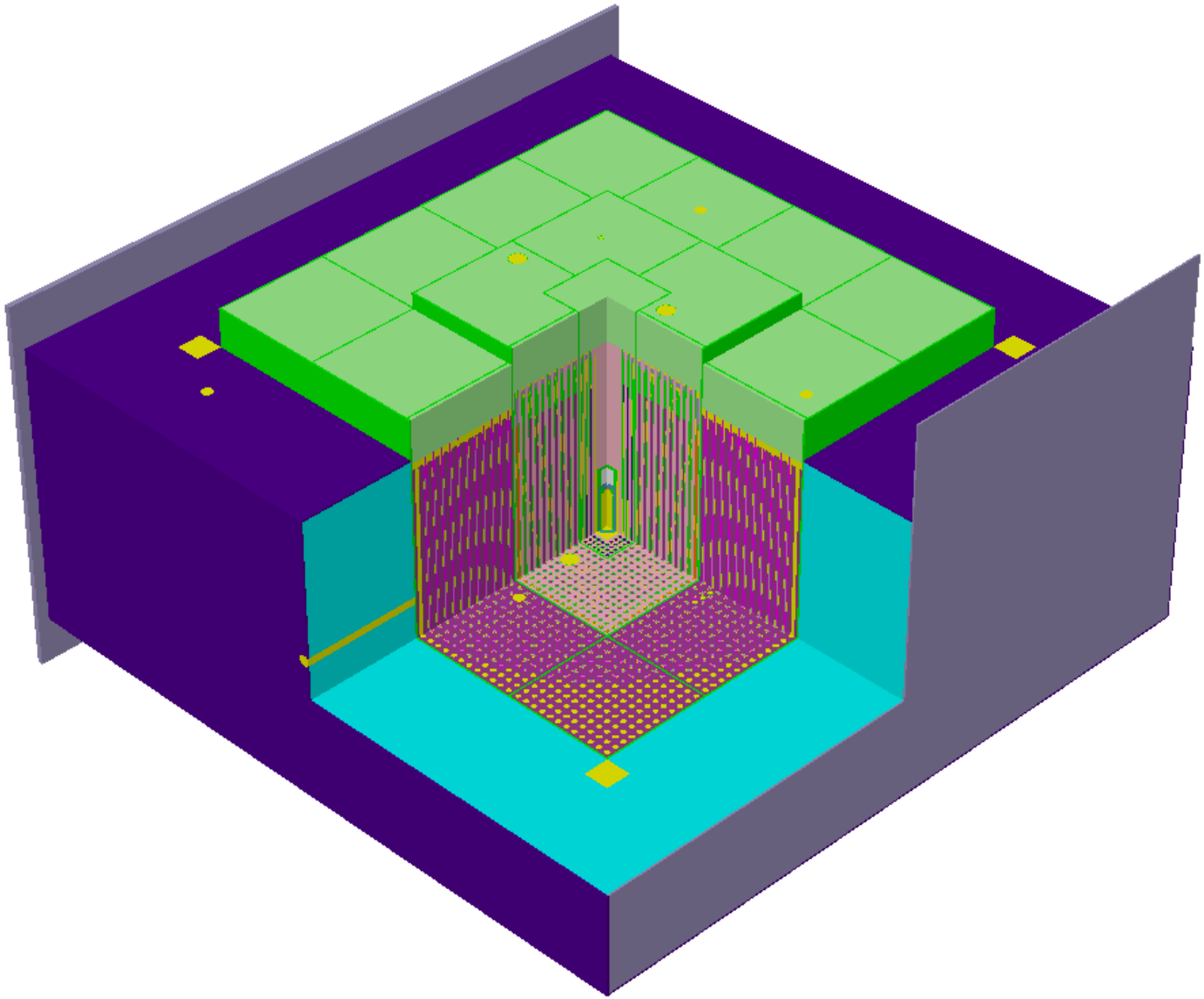

Figure 2. Three dimensional external view of the YALINA-Booster subcritical assembly with corner cut to show the internal parts plotted by VISTA-RAY

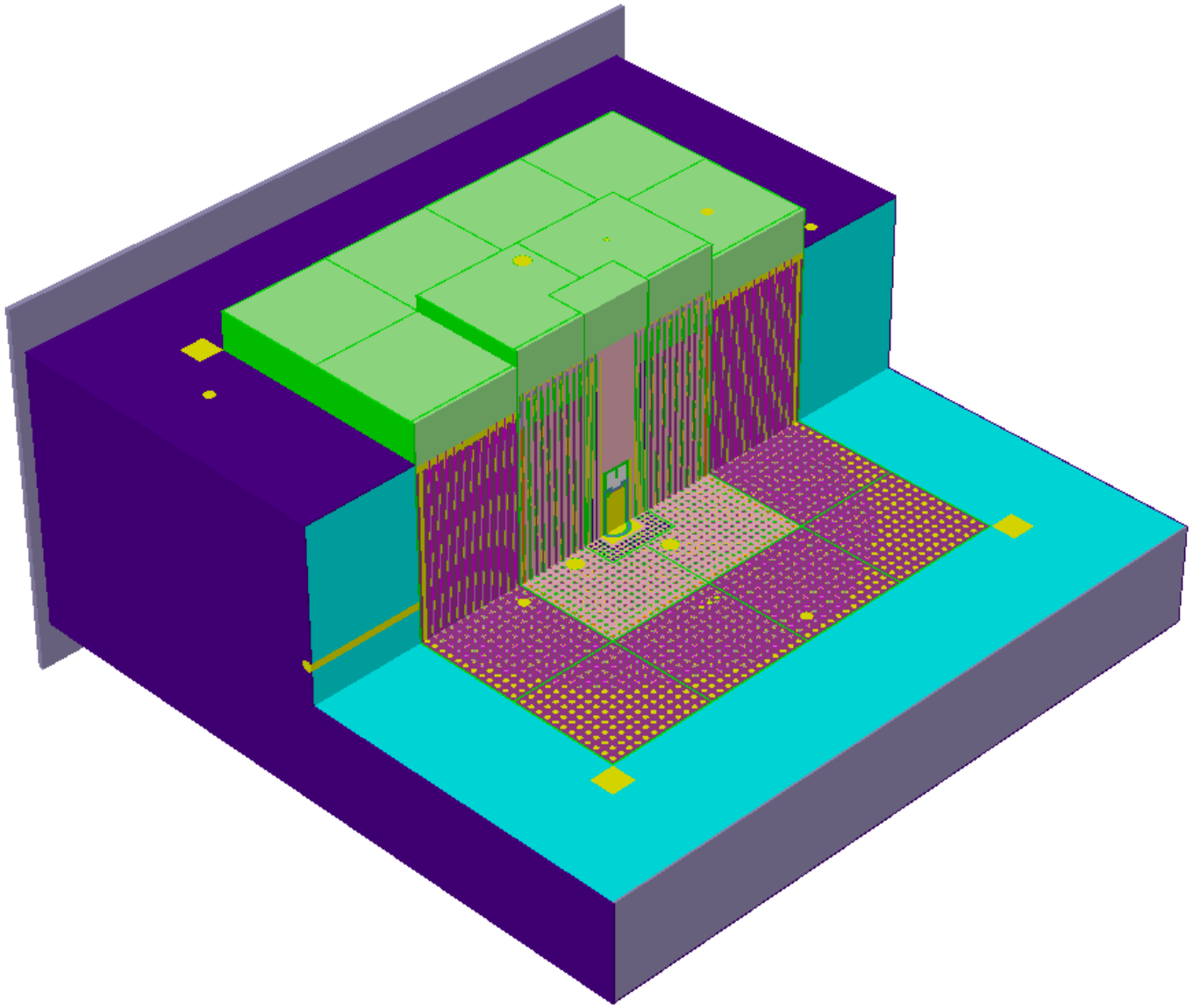

Figure 3. Three dimensional external view of the YALINA-Booster subcritical assembly with right half side cut to show the internal parts plotted by VISTA-RAY

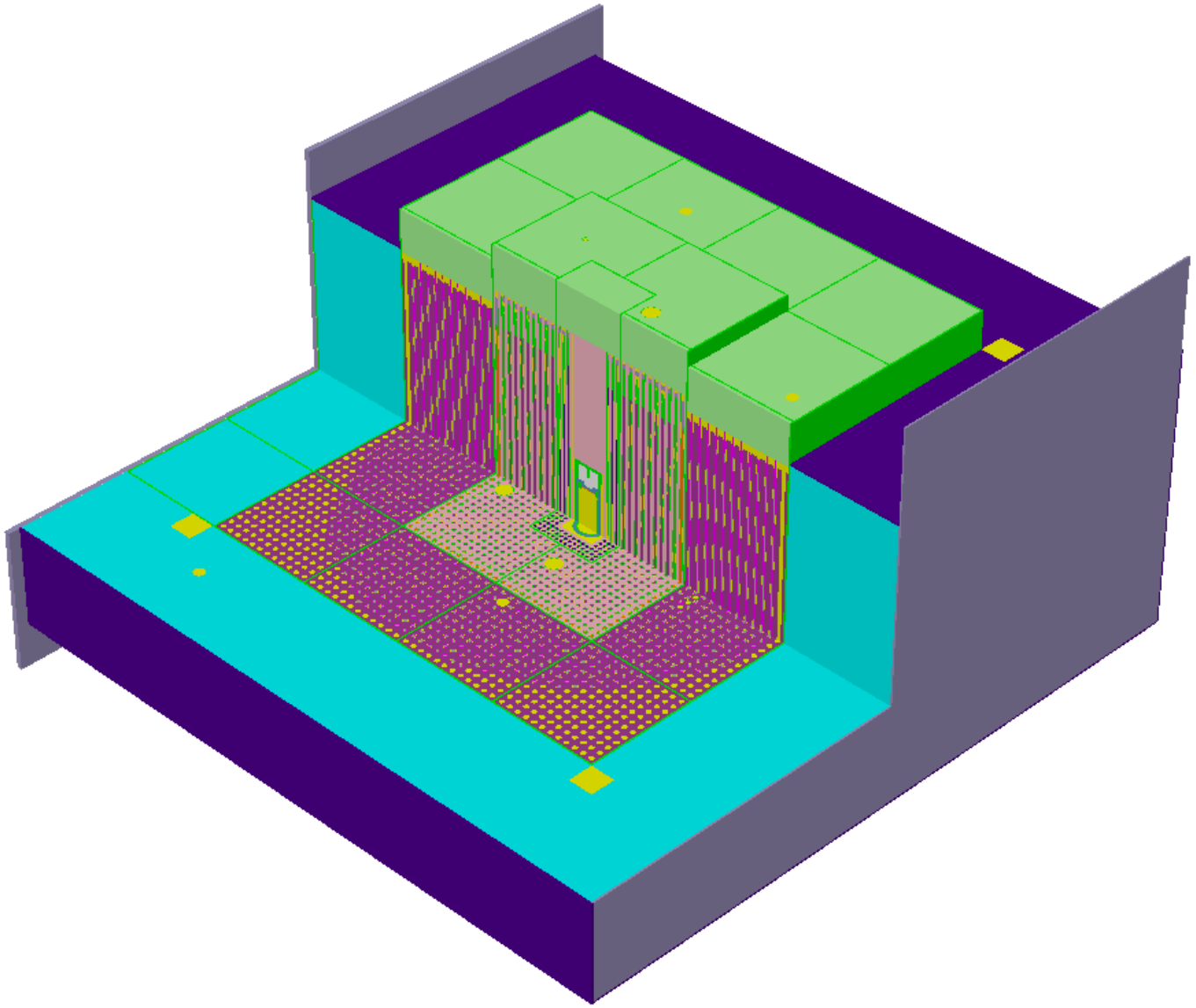

Figure 4. Three dimensional external view of the YALINA-Booster subcritical assembly with left half side cut to show the internal parts plotted by VISTA-RAY

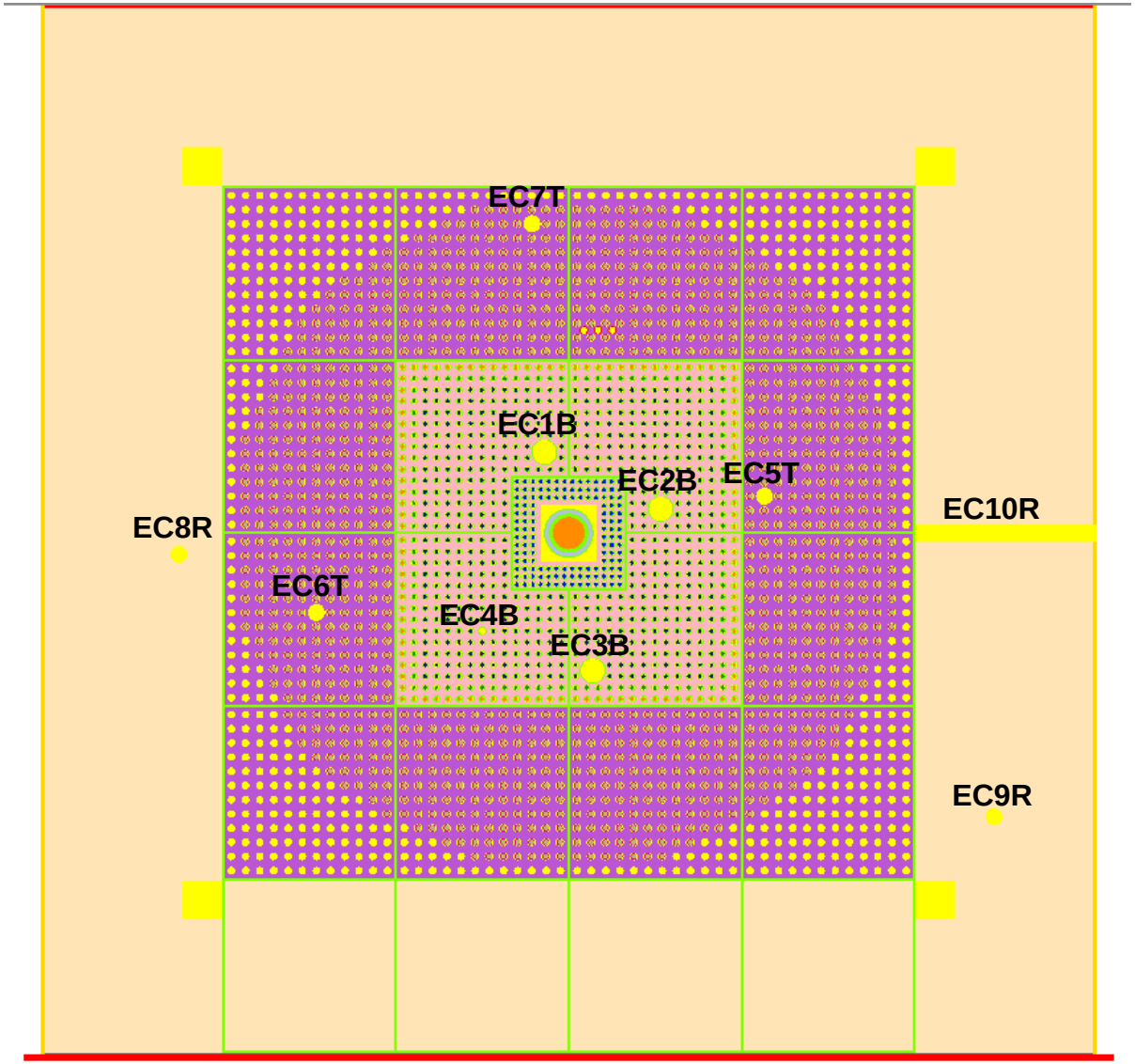

Figure 5. Horizontal section of the YALINA-Booster subcritical configuration with 1141 EK-10 fuel rods plotted by VISAGE

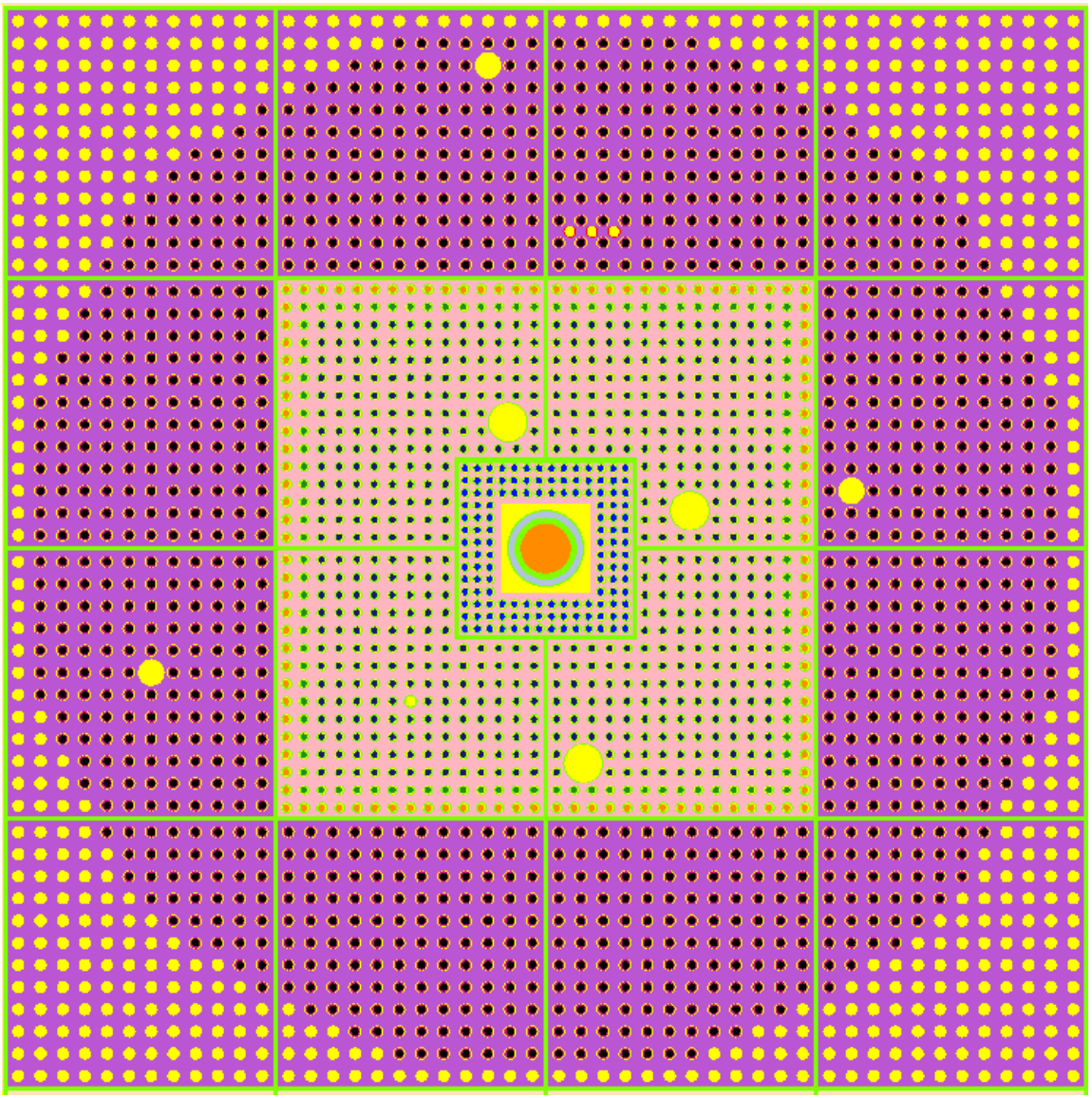

Figure 6. Horizontal section of the YALINA-Booster subcritical configuration with 1141 EK-10 fuel rods for the target, fast, and thermal zones plotted by VISAGE

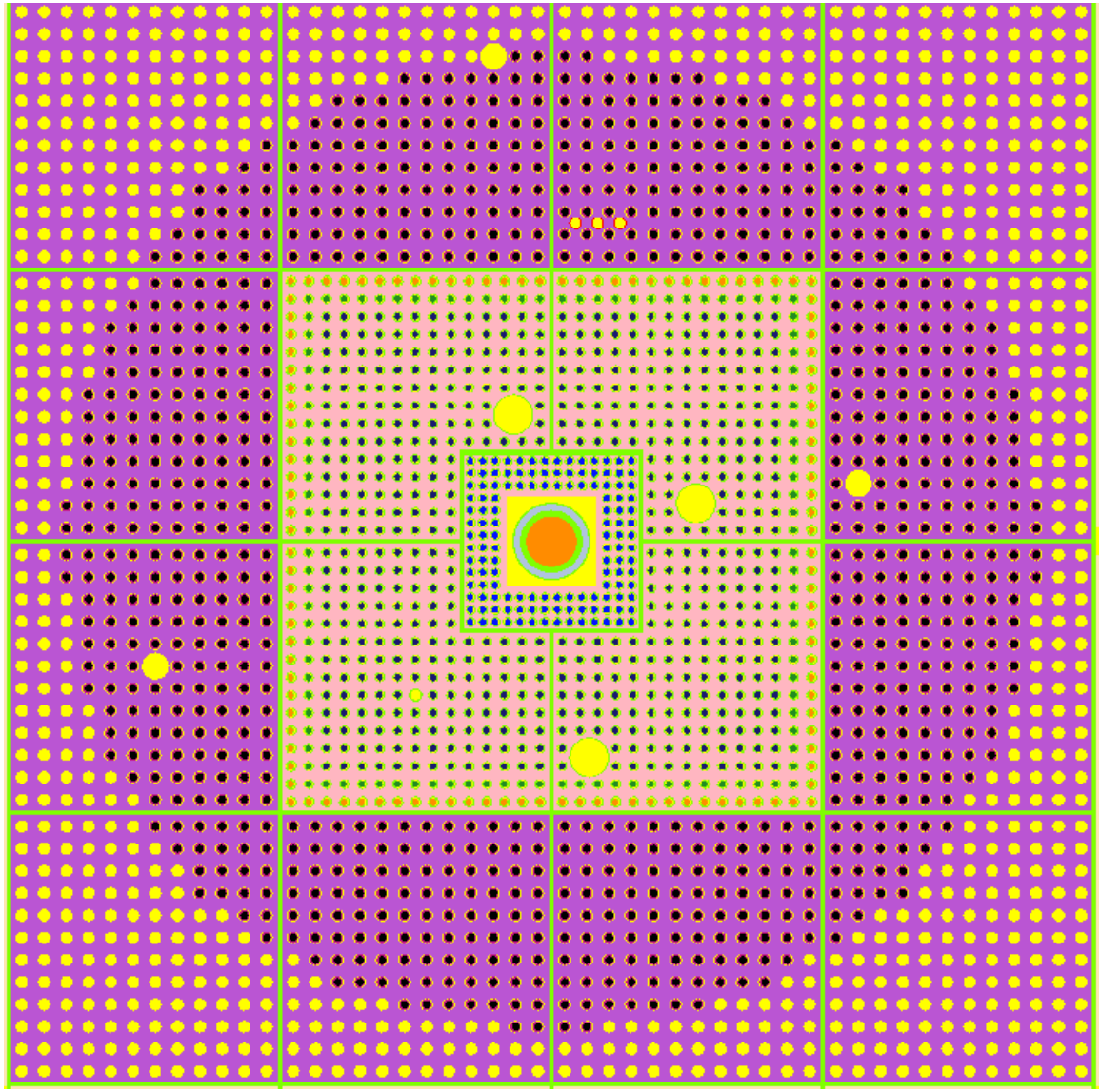

Figure 7. Horizontal section of the YALINA-Booster subcritical configuration with 902 EK-10 fuel rods for the target, fast, and thermal plotted by VISAGE

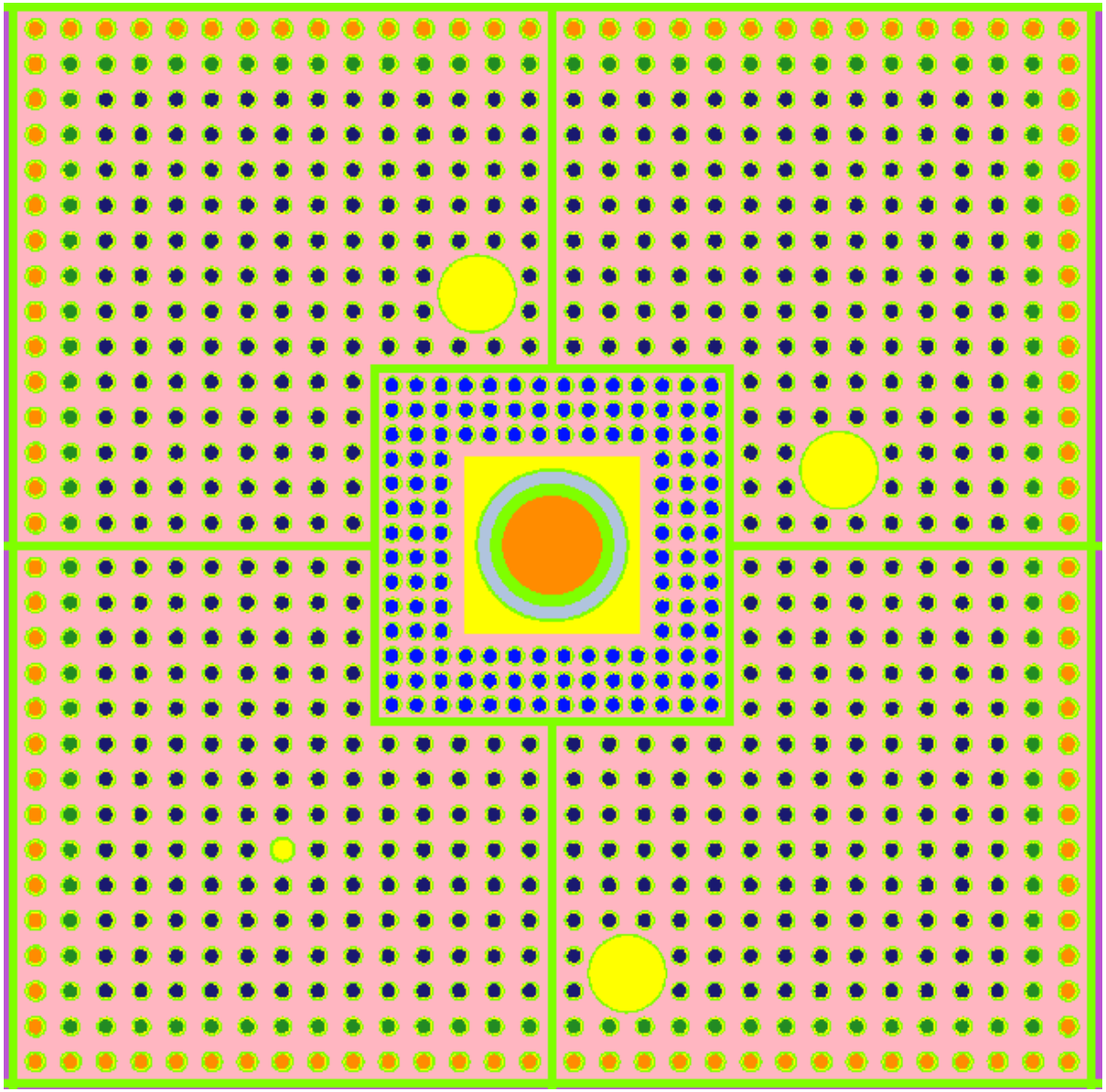

Figure 8. Horizontal section of the YALINA-Booster for the target and fast zones plotted by VISAGE

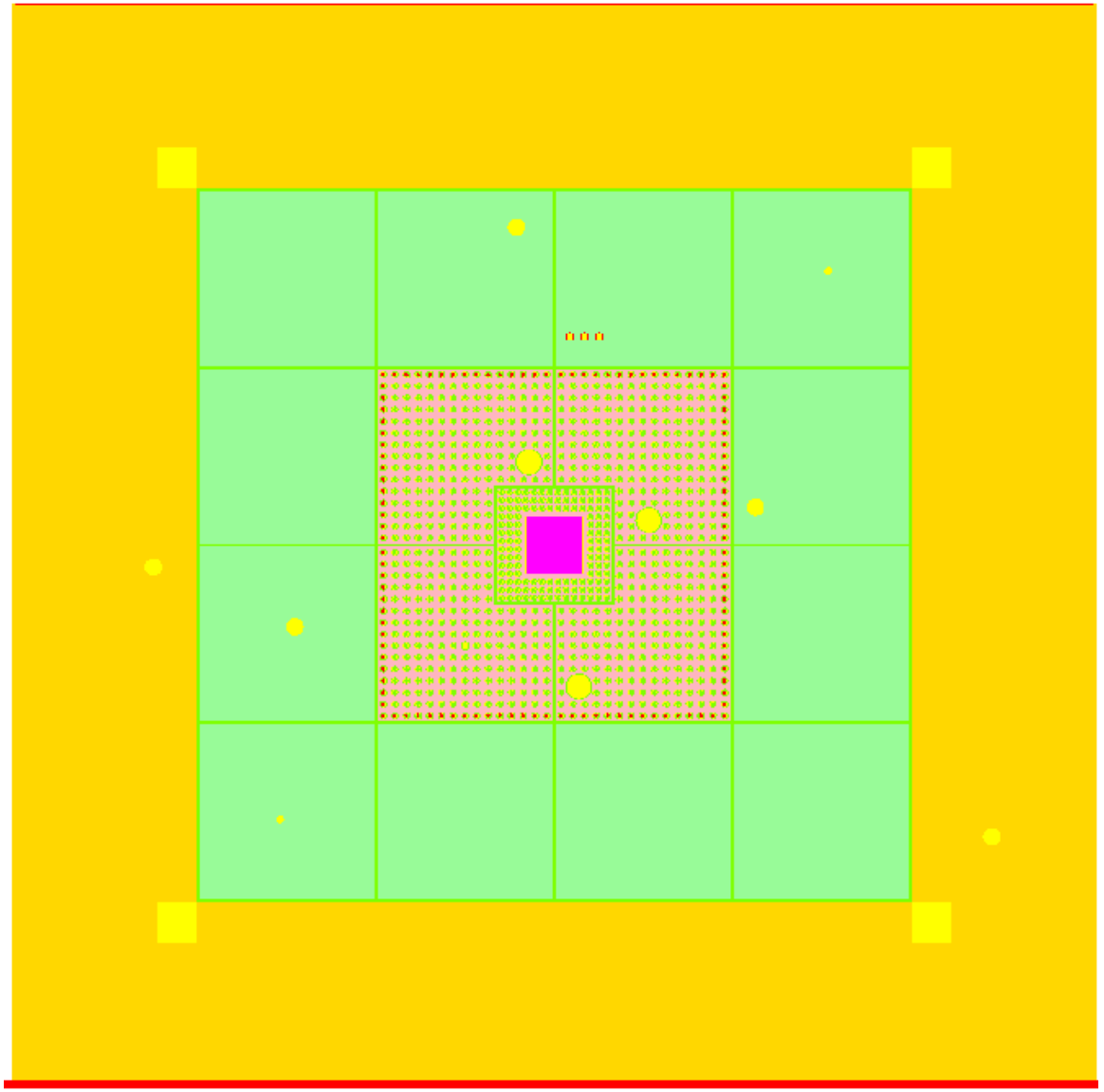

Figure 9. Horizontal section of the YALINA-Booster at the axial height of the top organic glass layer plotted by VISAGE

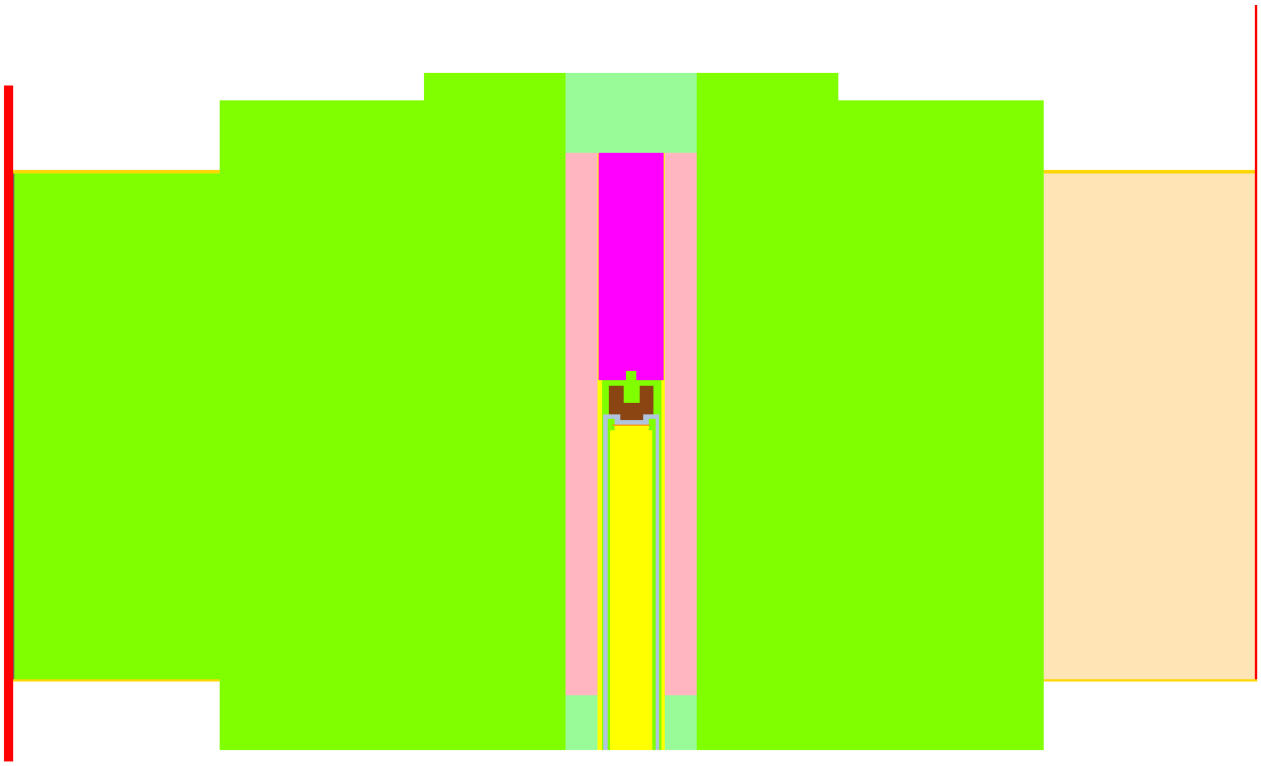

Figure 10. Vertical section of the YALINA-Booster at x=0 plotted by VISAGE

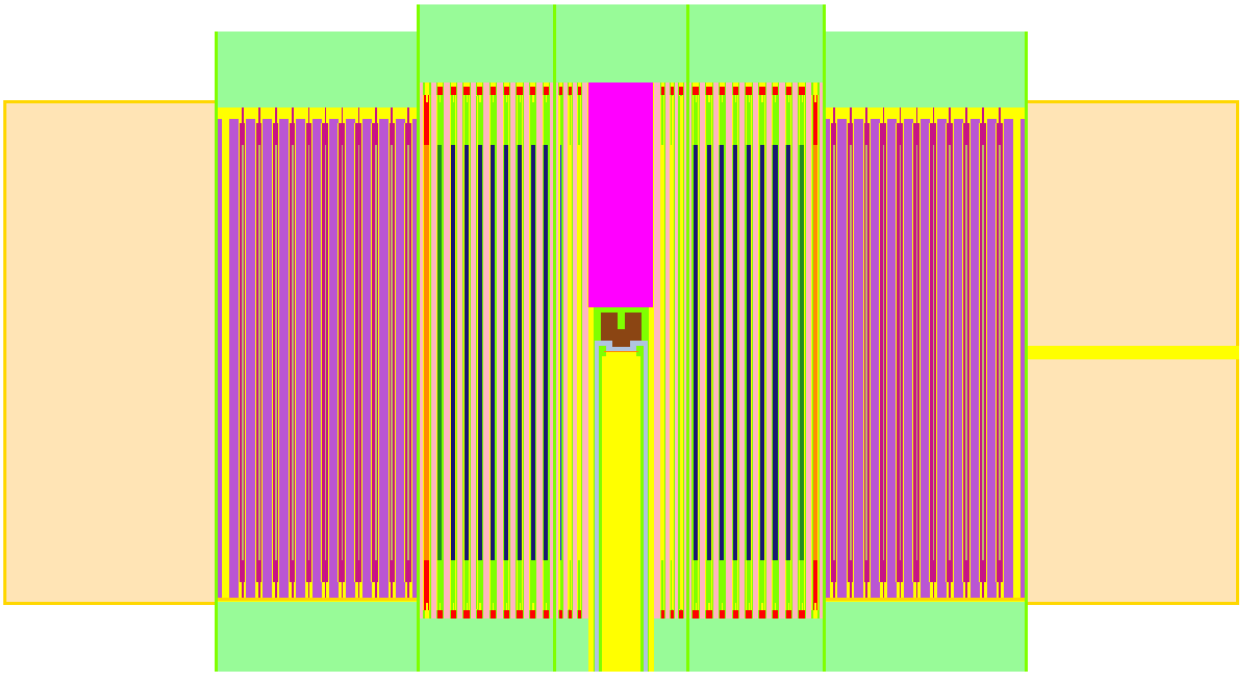

Figure 11. Vertical section of the YALINA-Booster at y=0.87 plotted by VISAGE

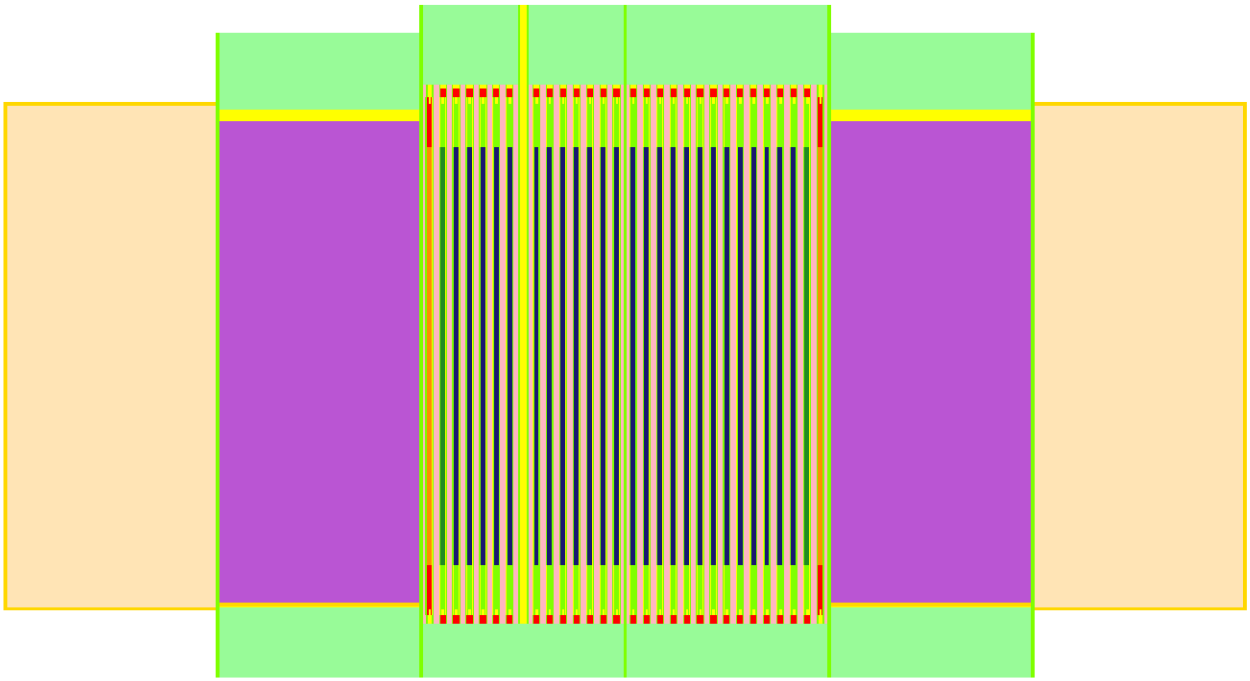

Figure 12. Vertical section of the YALINA-Booster at the location of EC4B (y=-13.8) plotted by VISAGE

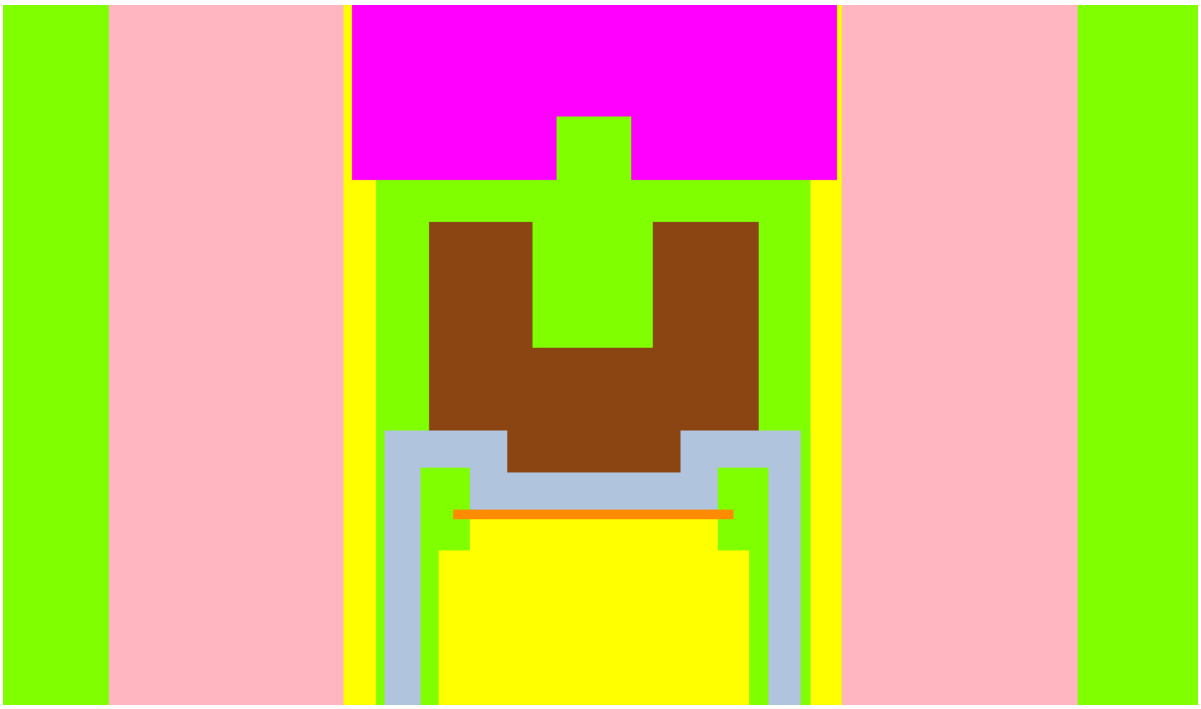

Figure 13. Vertical section of the target zone of the YALINA-Booster plotted by VISAGE

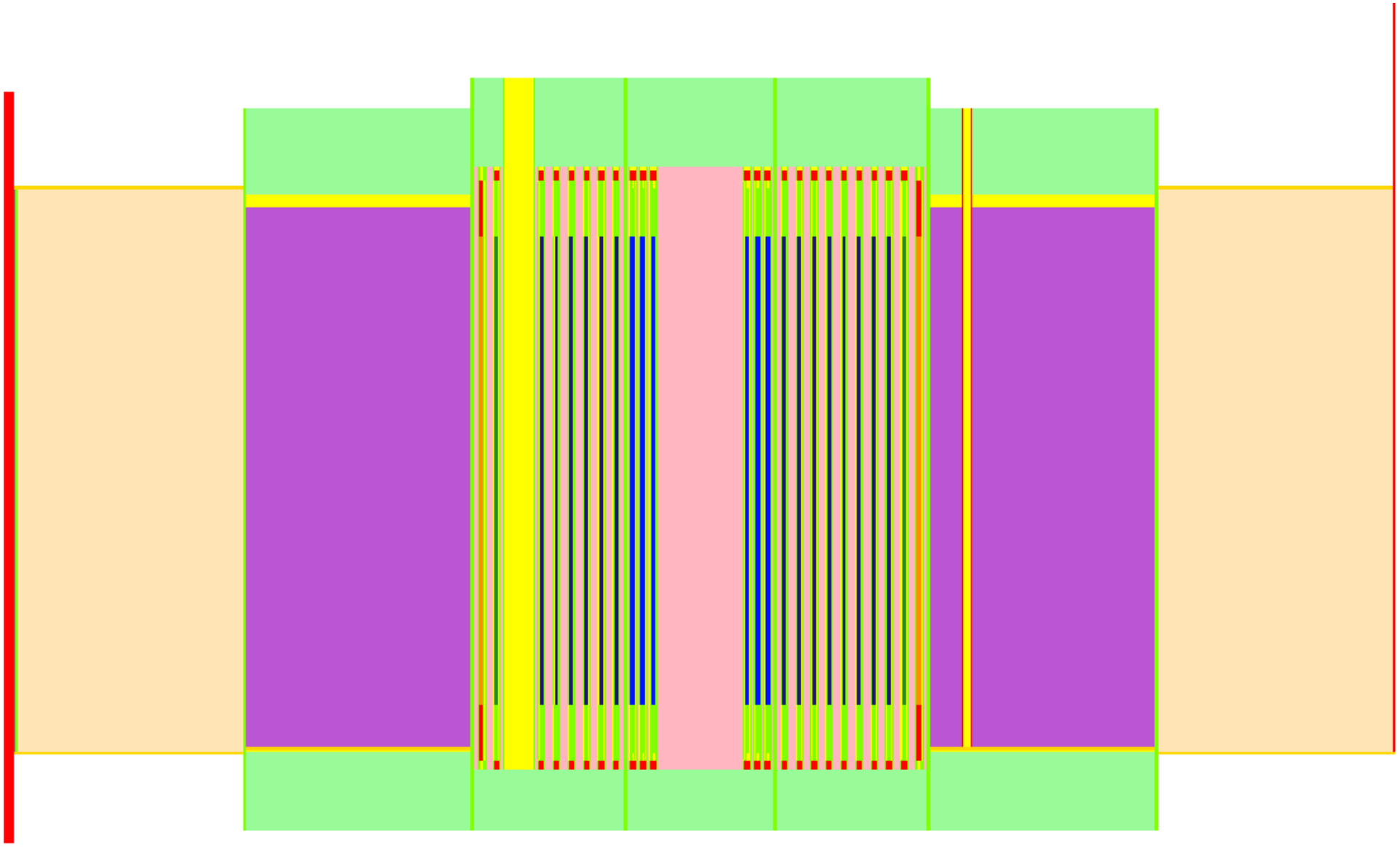

Figure 14. Vertical section of the YALINA-Booster at x=4.01 plotted by VISAGE

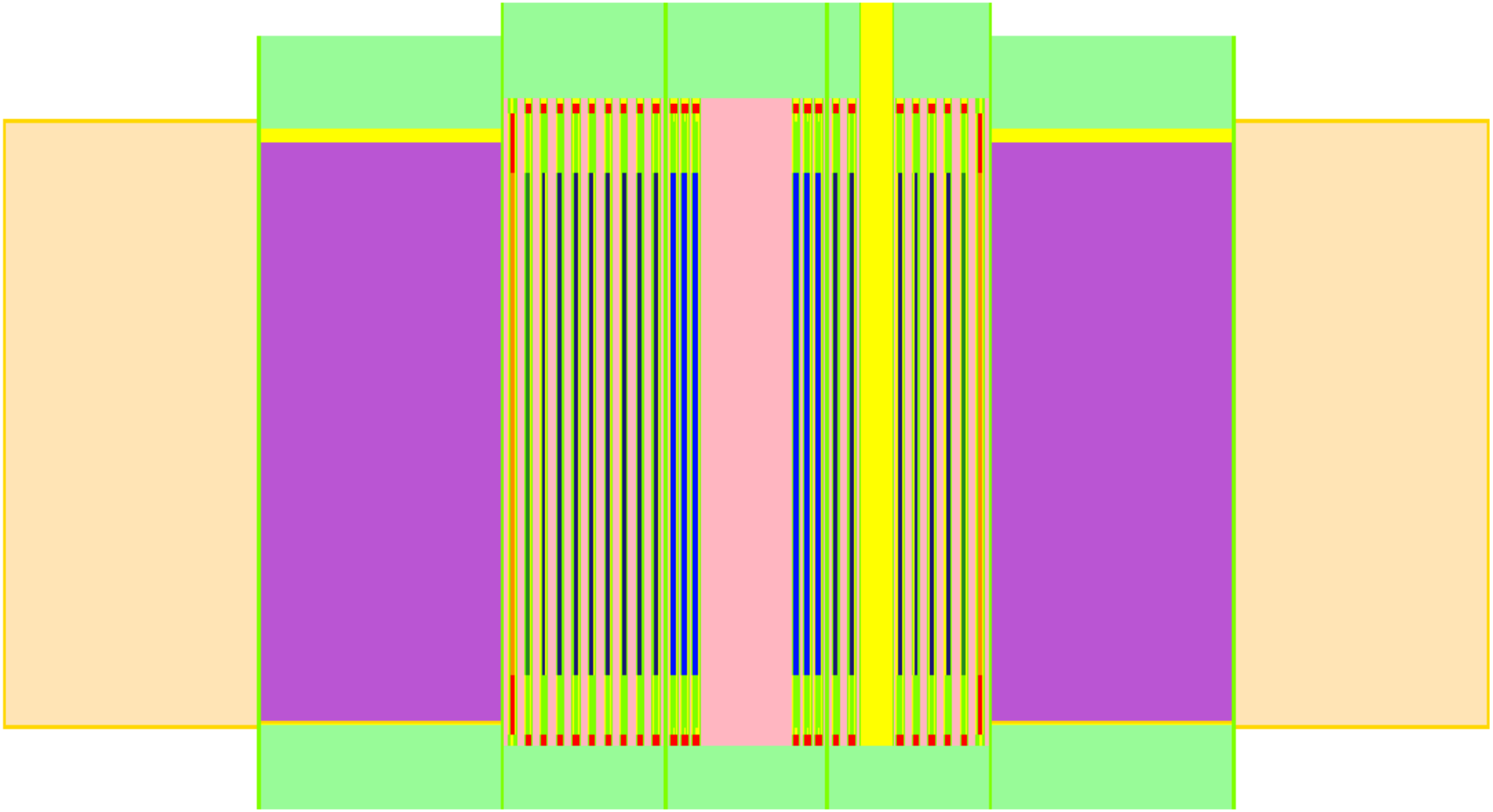

Figure 15. Vertical section of the YALINA-Booster at y=4.01 plotted by VISAGE

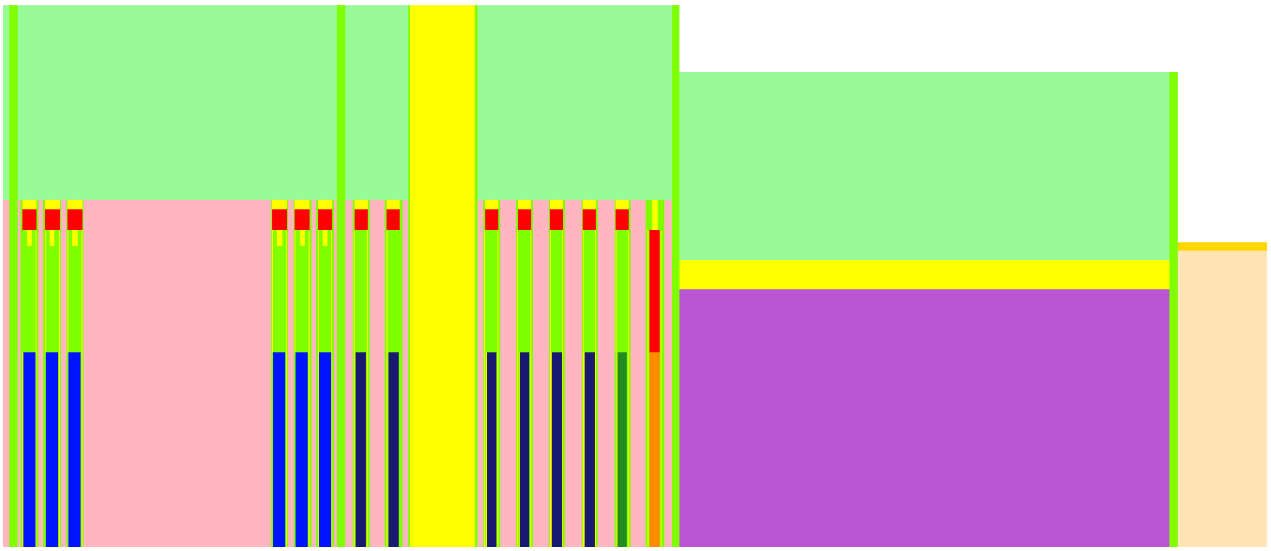

Figure 16. Top zoom of the vertical section of the YALINA-Booster at y=4.01 plotted by VISAGE

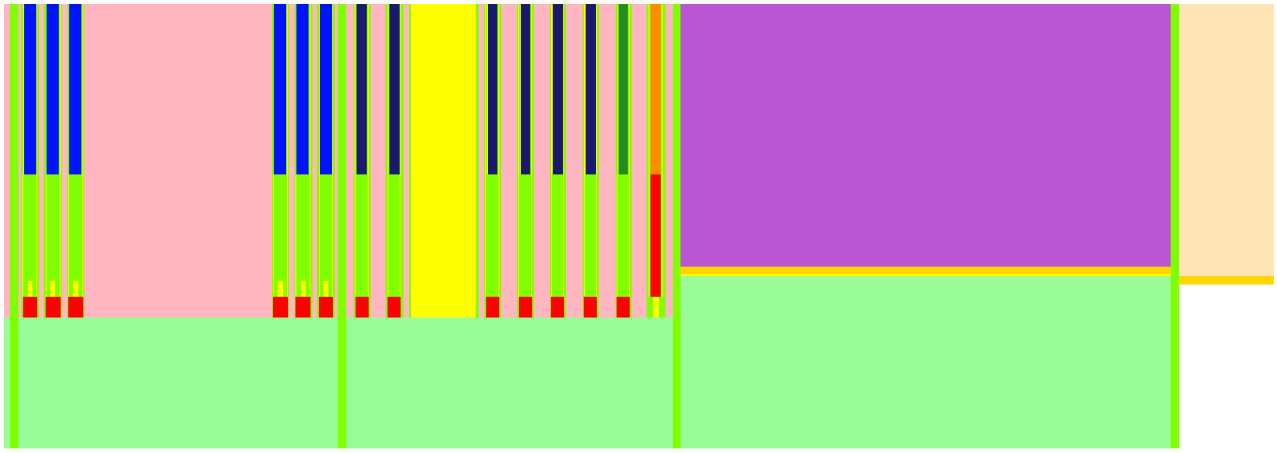

Figure 17. Bottom zoom of the vertical section of the YALINA-Booster at y=4.01 plotted by VISAGE

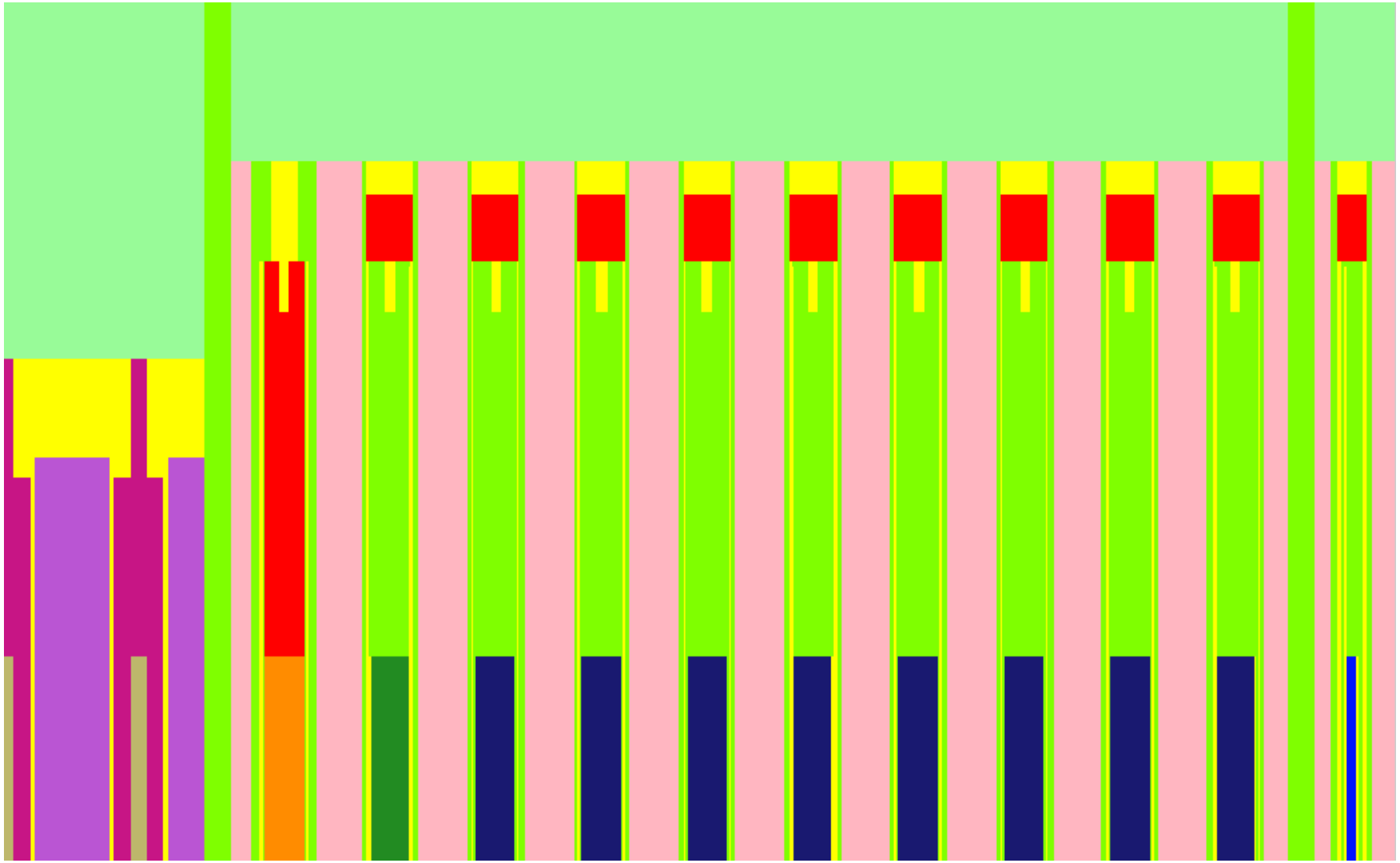

Figure 18. Top zoom of the vertical section of the YALINA-Booster plotted by VISAGE

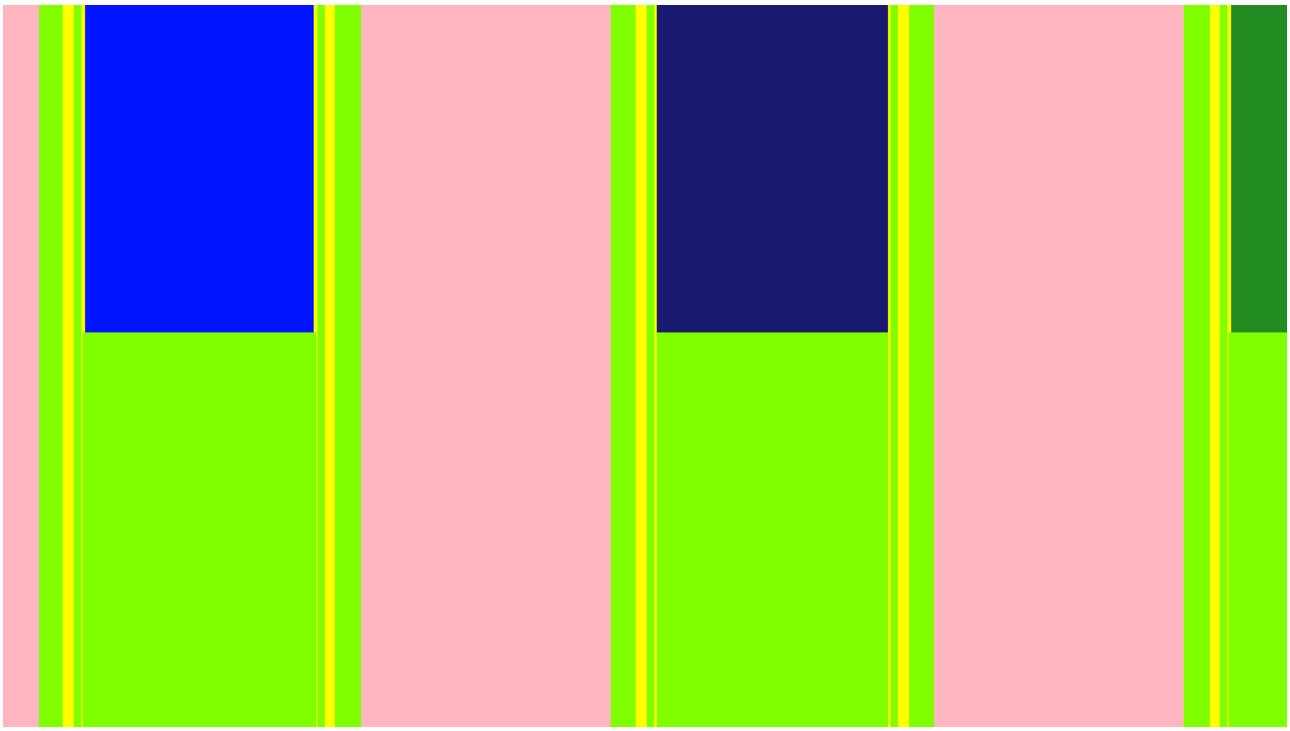

Figure 19. Detail of the fuel rods in the fast zone of the YALINA-Booster plotted by VISAGE

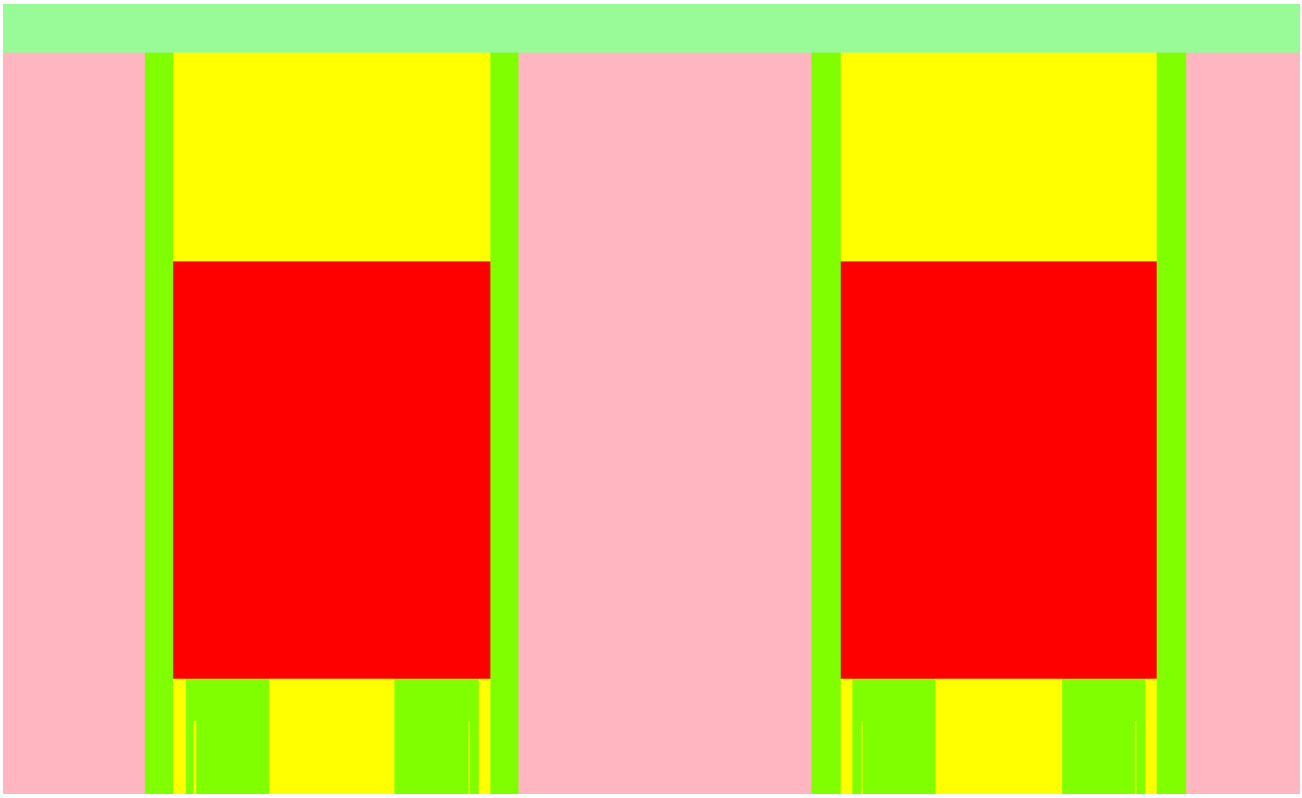

Figure 20. Detail of the fuel rods in the fast zone of the YALINA-Booster plotted by VISAGE

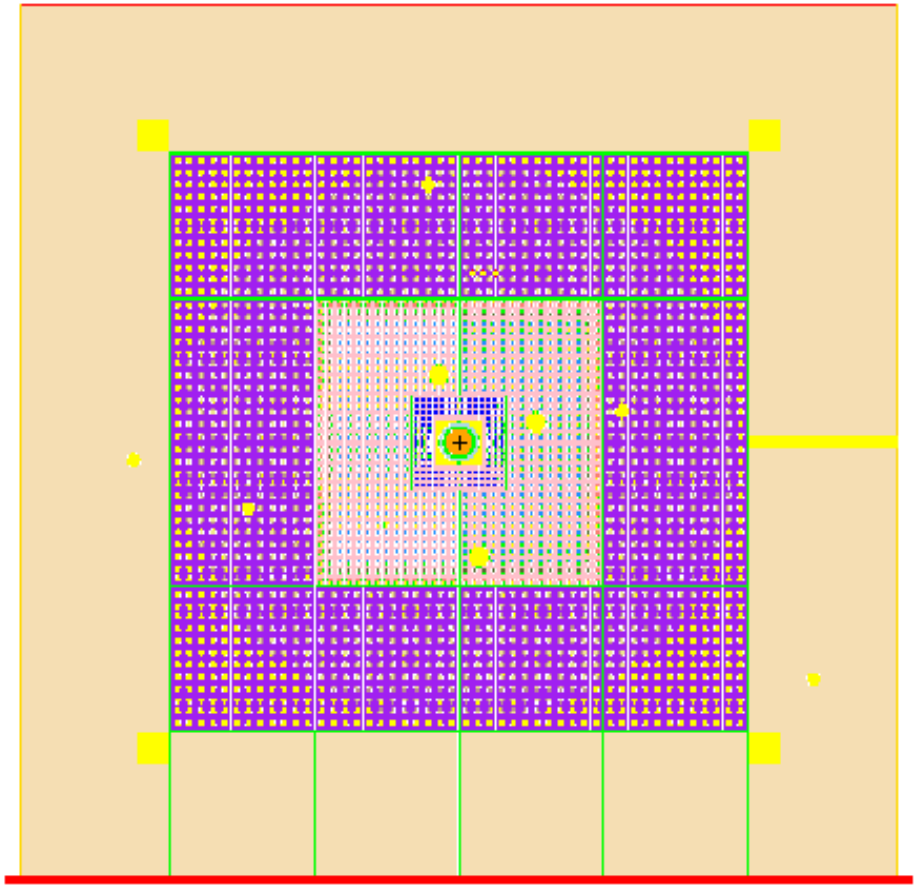

Figure 21. Horizontal section of the YALINA-Booster plotted by MCNP5

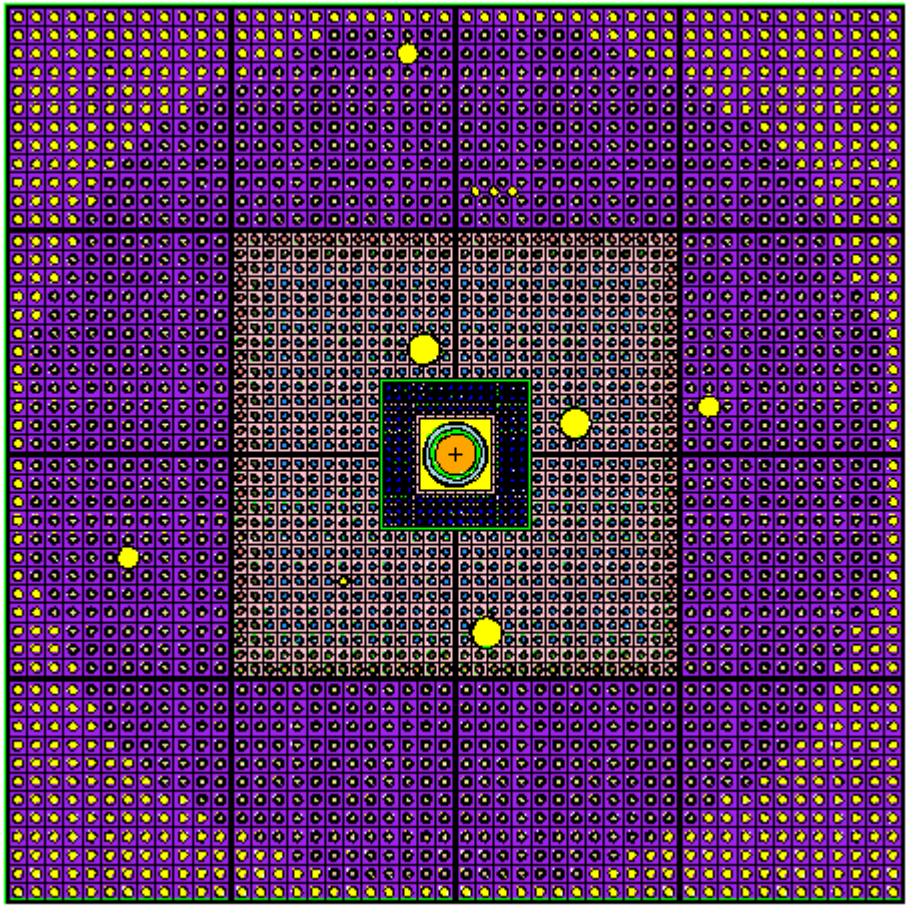

Figure 22. Horizontal section of the fast and thermal zones of the YALINA-Booster plotted by MCNP5

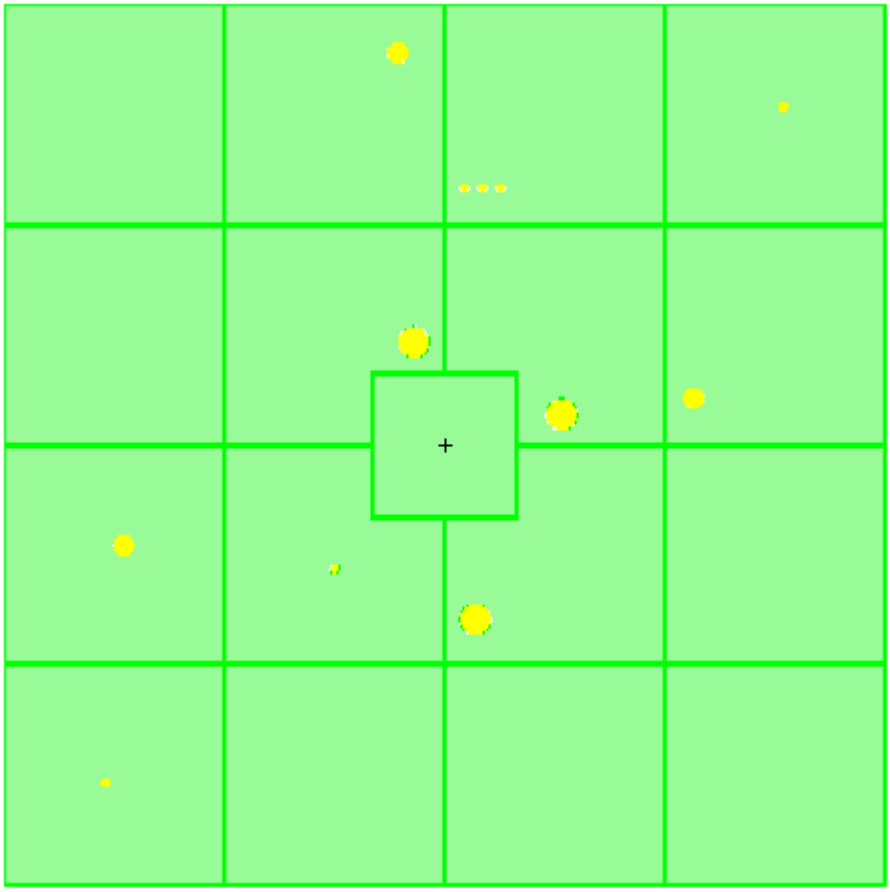

Figure 23. Horizontal section of the top borated polyethylene reflector of the YALINA-Booster plotted by MCNP5

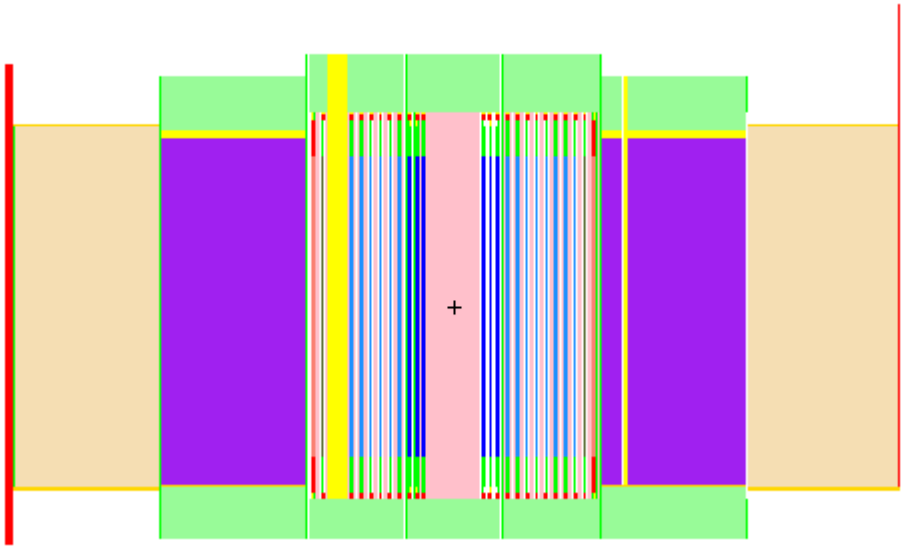

Figure 24. Vertical section of the YALINA-Booster at x=4.01 plotted by MCNP5

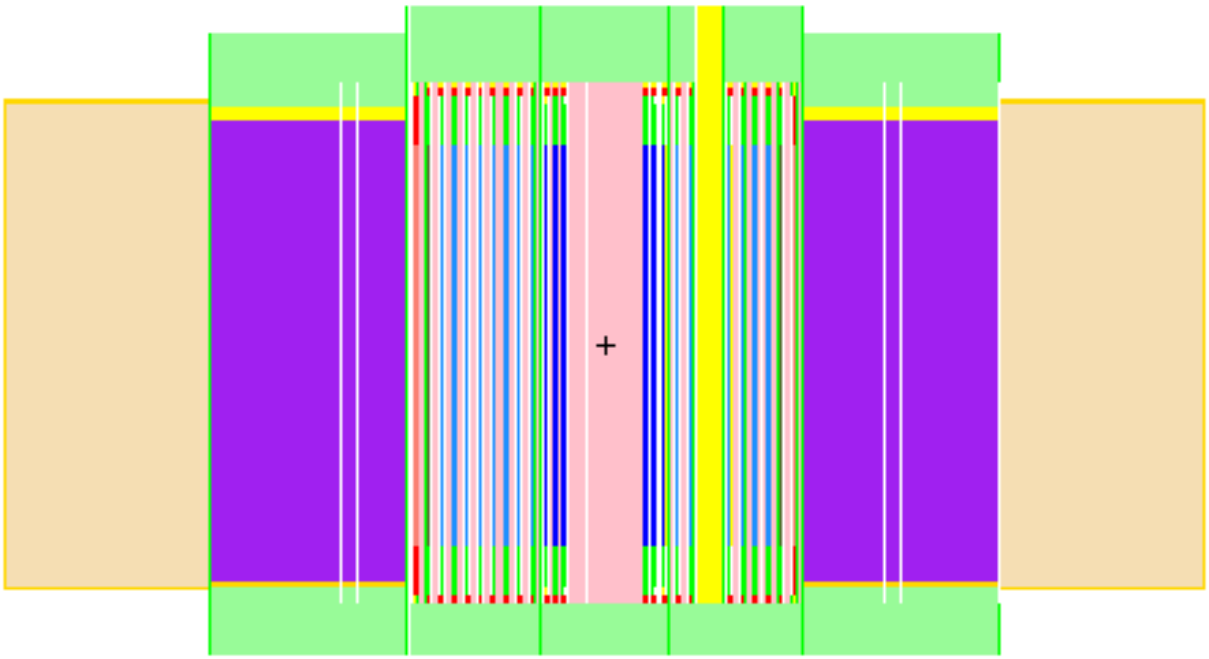

Figure 25. Vertical section of the YALINA-Booster at y=4.01 plotted by MCNP5

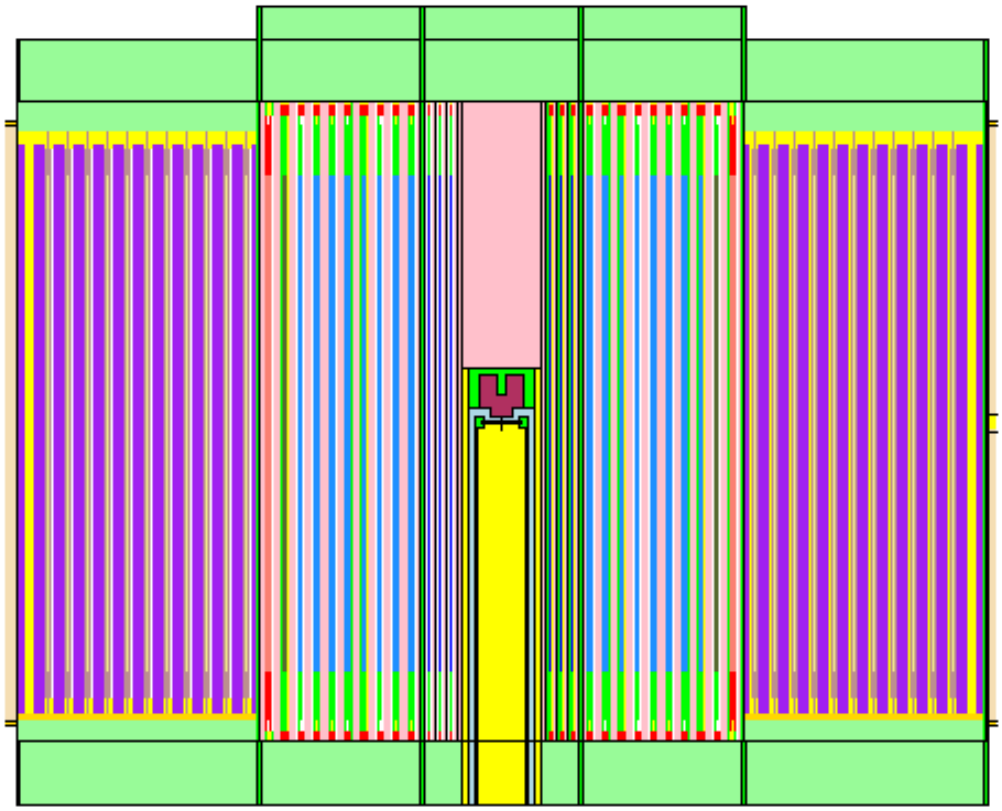

Figure 26. Zoom of the vertical section of the YALINA-Booster plotted by MCNP5

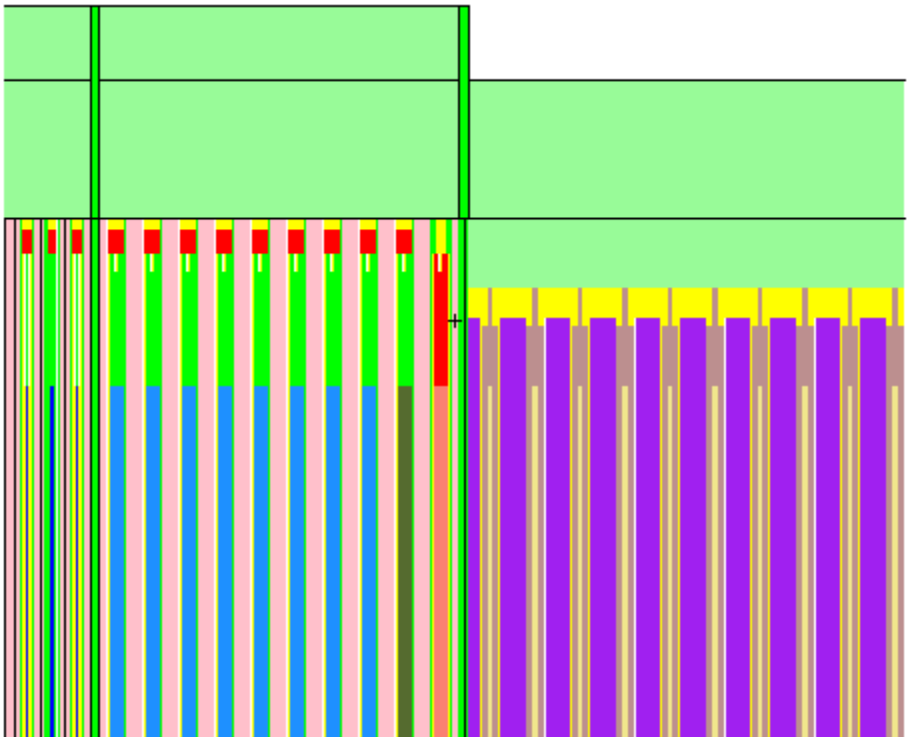

Figure 27. Top zoom of the vertical section of the YALINA-Booster plotted by MCNP5

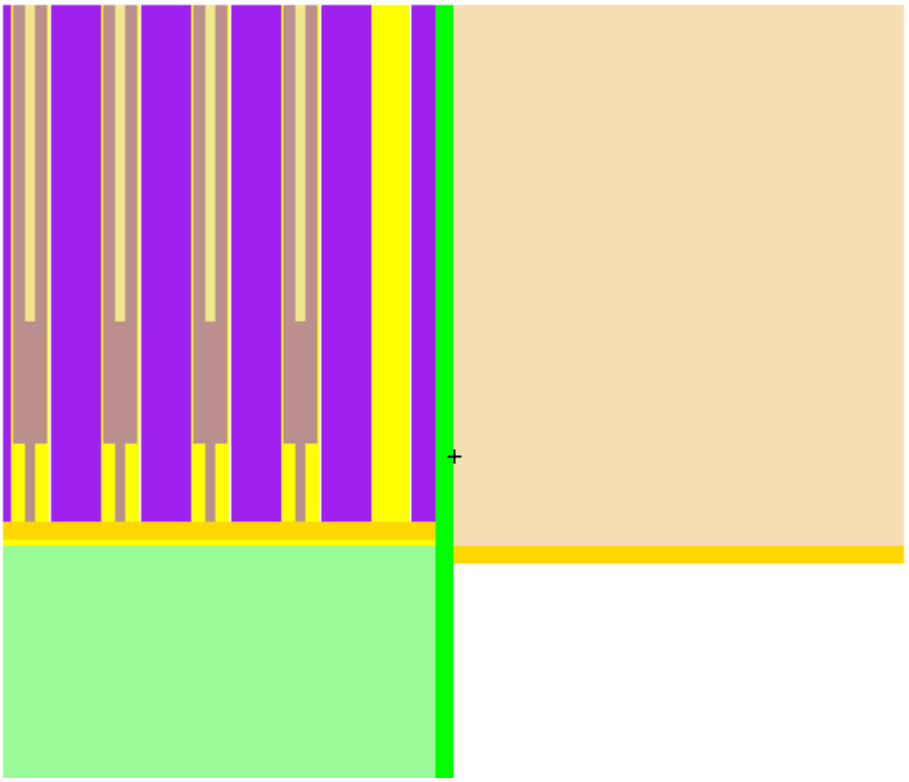

Figure 28. Bottom zoom of the vertical section of the YALINA-Booster plotted by MCNP5

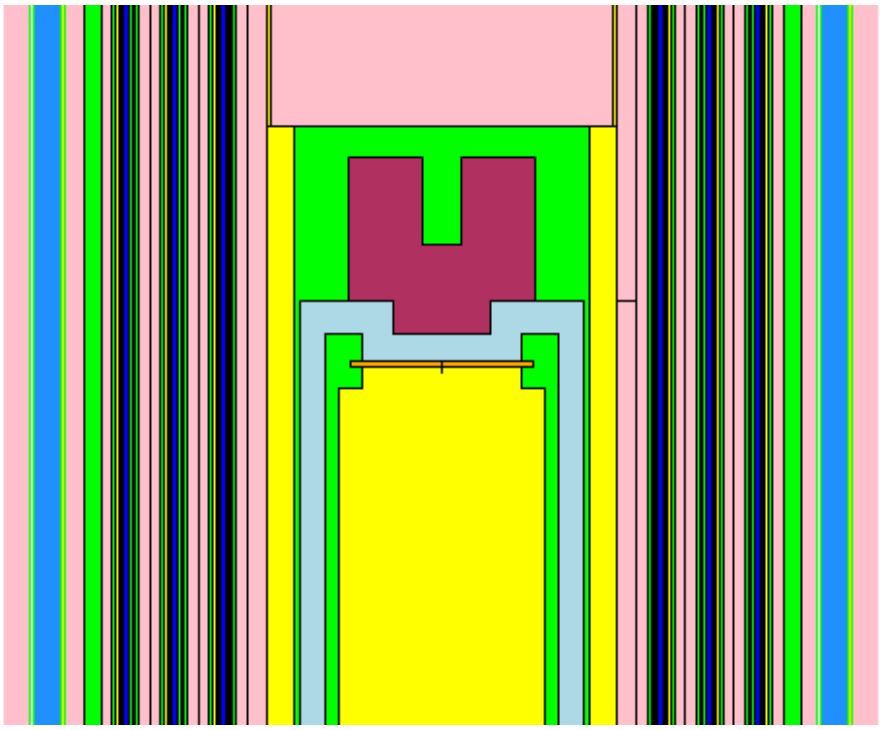

Figure 29. Vertical section of the target zone of the YALINA-Booster plotted by MCNP5

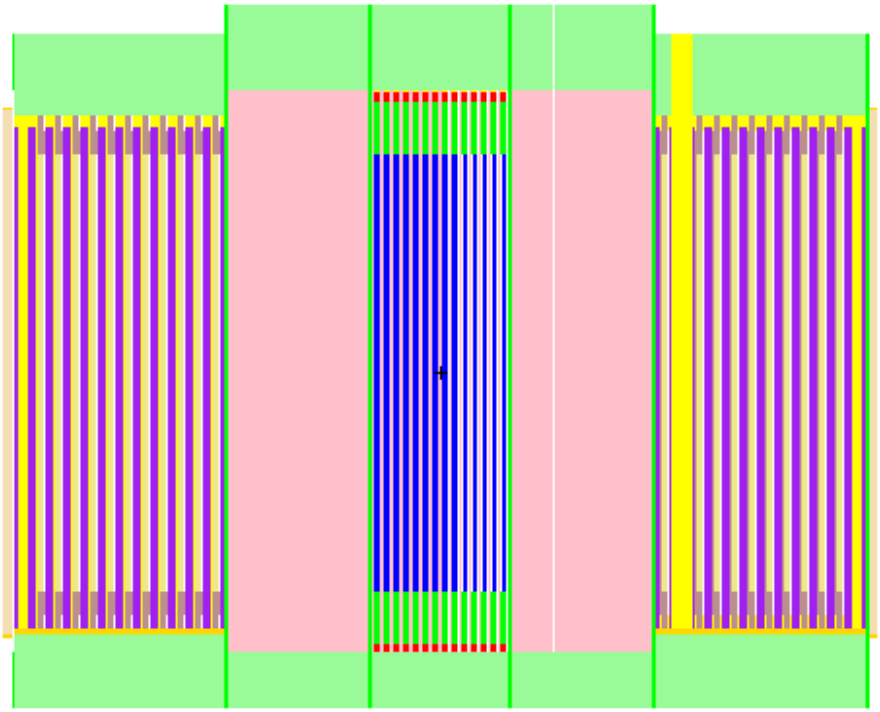

Figure 30. Vertical section of the YALINA-Booster at the location of EC5T plotted by MCNP5

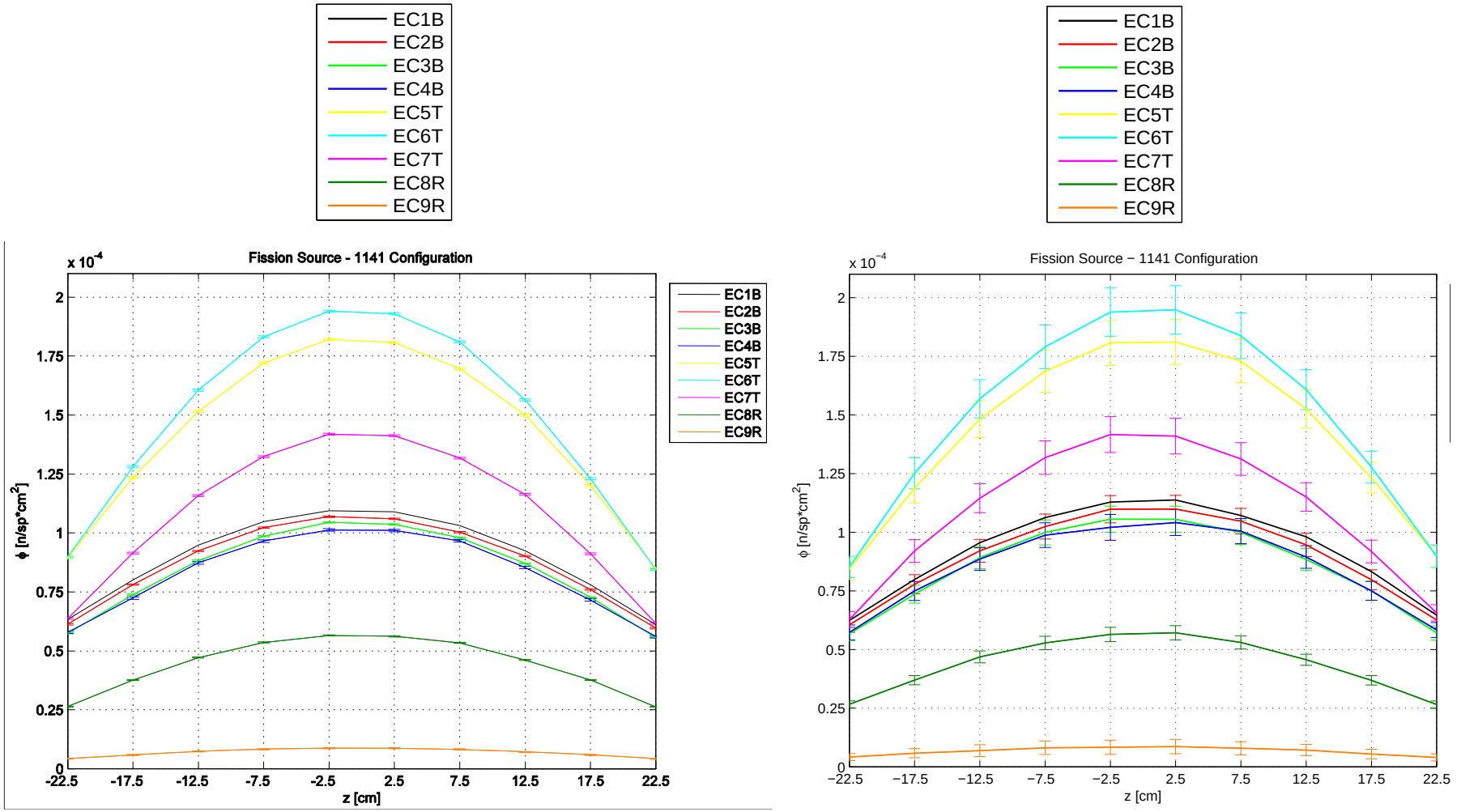

Figure 31. Axial neutron flux distribution in the experimental channels for the fission neutron source calculated by MCNPX (left) and MONK (right), The values are averaged over an experimental channel length of 5 cm length, 1141 configuration

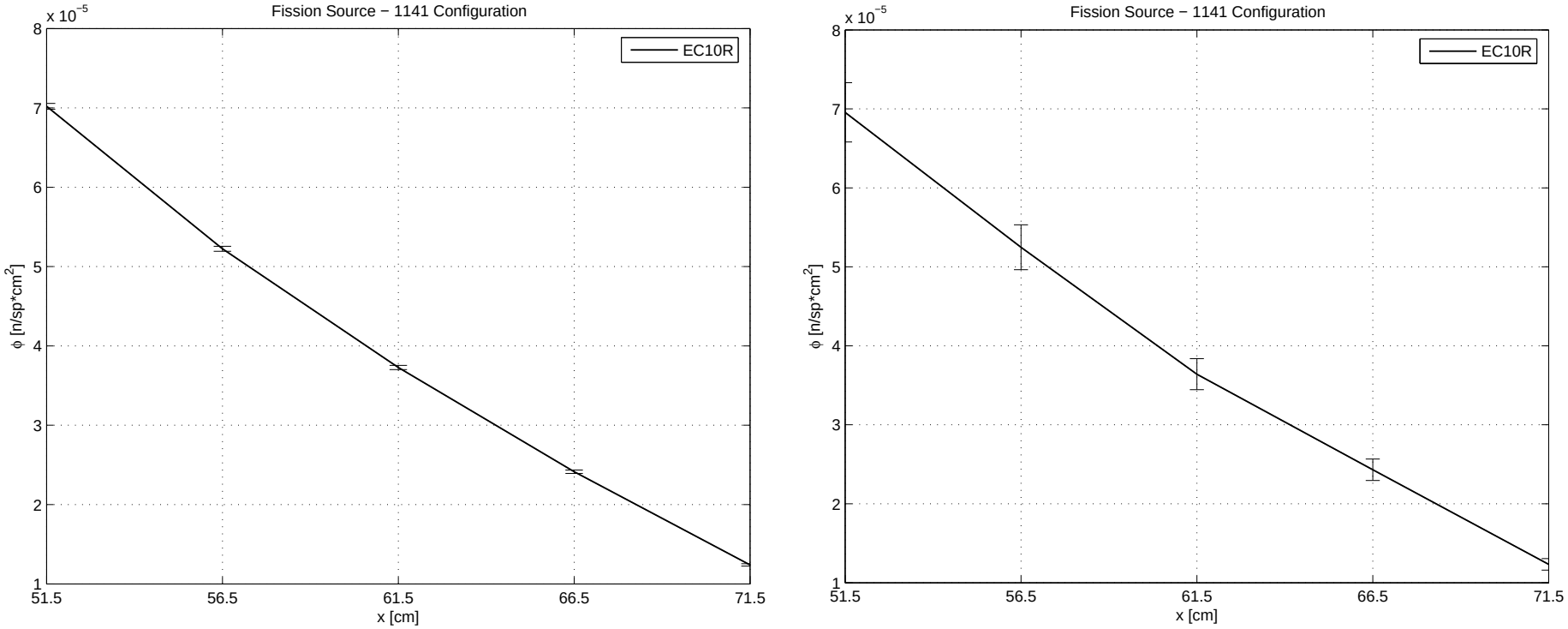

Figure 32. Radial neutron flux profile in the experimental channel EC10R for the fission neutron source calculated by MCNPX (left) and MONK (right), The values are averaged over an experimental channel length of 5 cm length, 1141 configuration

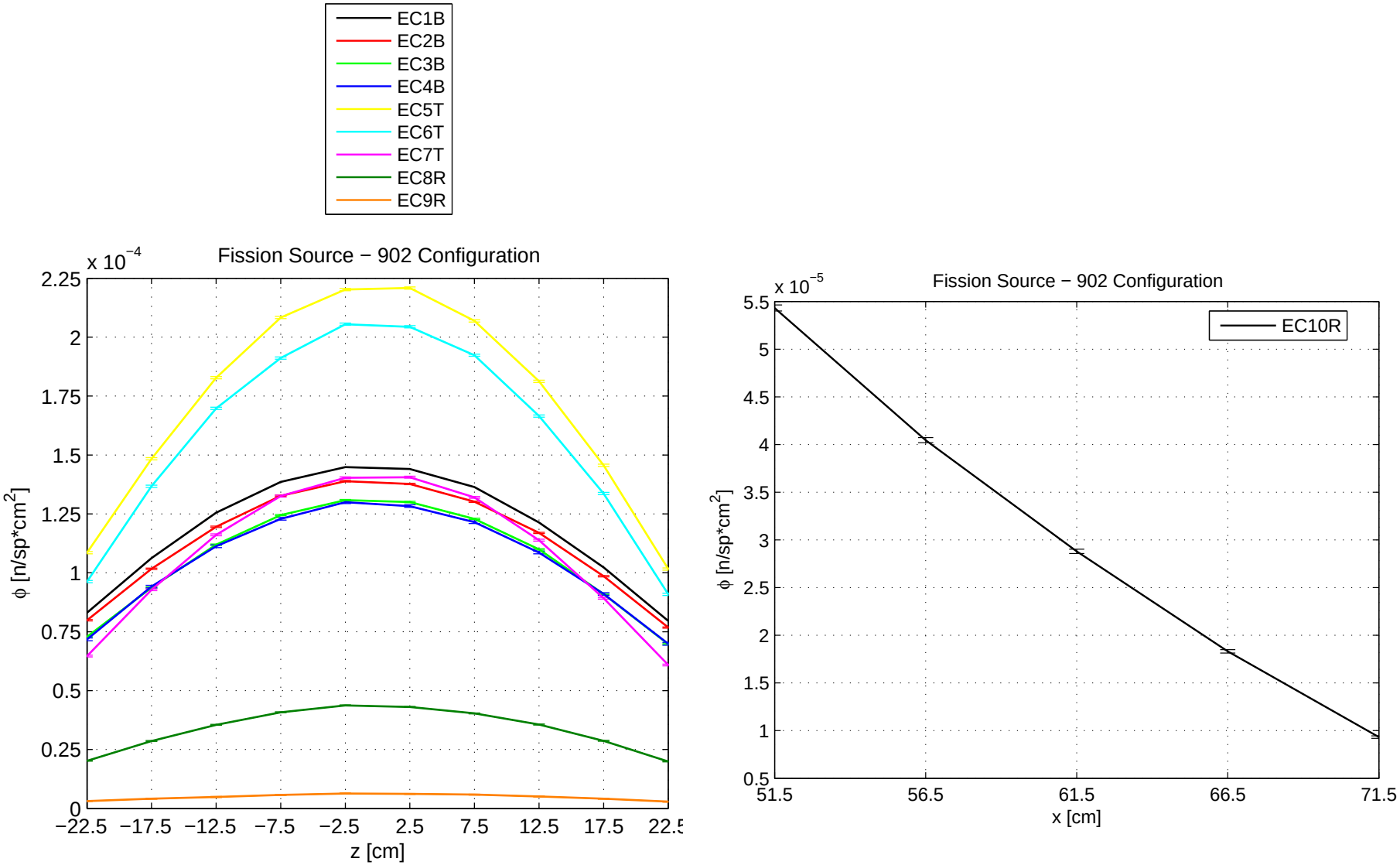

Figure 33. Axial and radial neutron flux profiles in the experimental channels for the fission neutron source calculated by MCNPX, The values are averaged over an experimental channel length of 5 cm length, 902 configuration

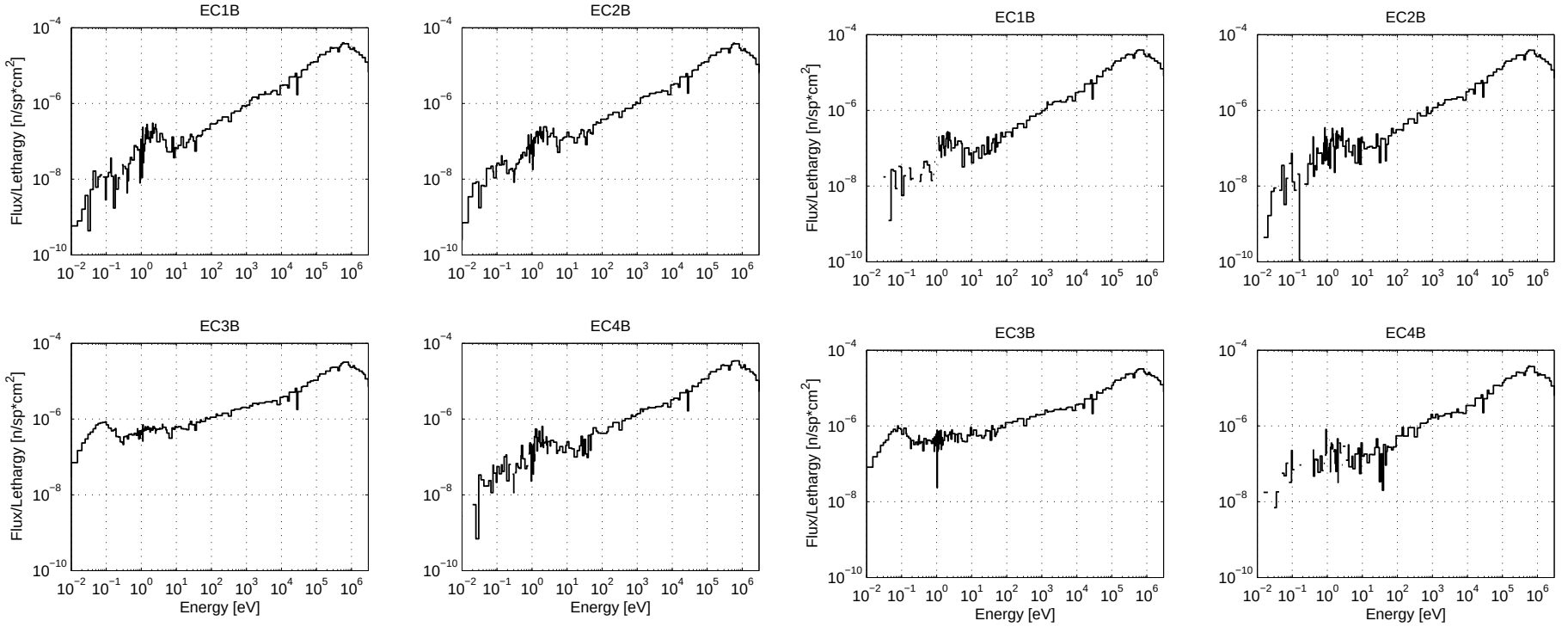

Figure 34. Neutron spectrum of the YALINA-Booster configuration with 1141 EK-10 fuel rods in the experimental channels of the fast zone for the fission neutron source calculated by MCNPX (left) and MONK (right) using 172 neutron energy group structure, The spectra were calculated at the center of the active fuel length and over 10 cm experimental channel length

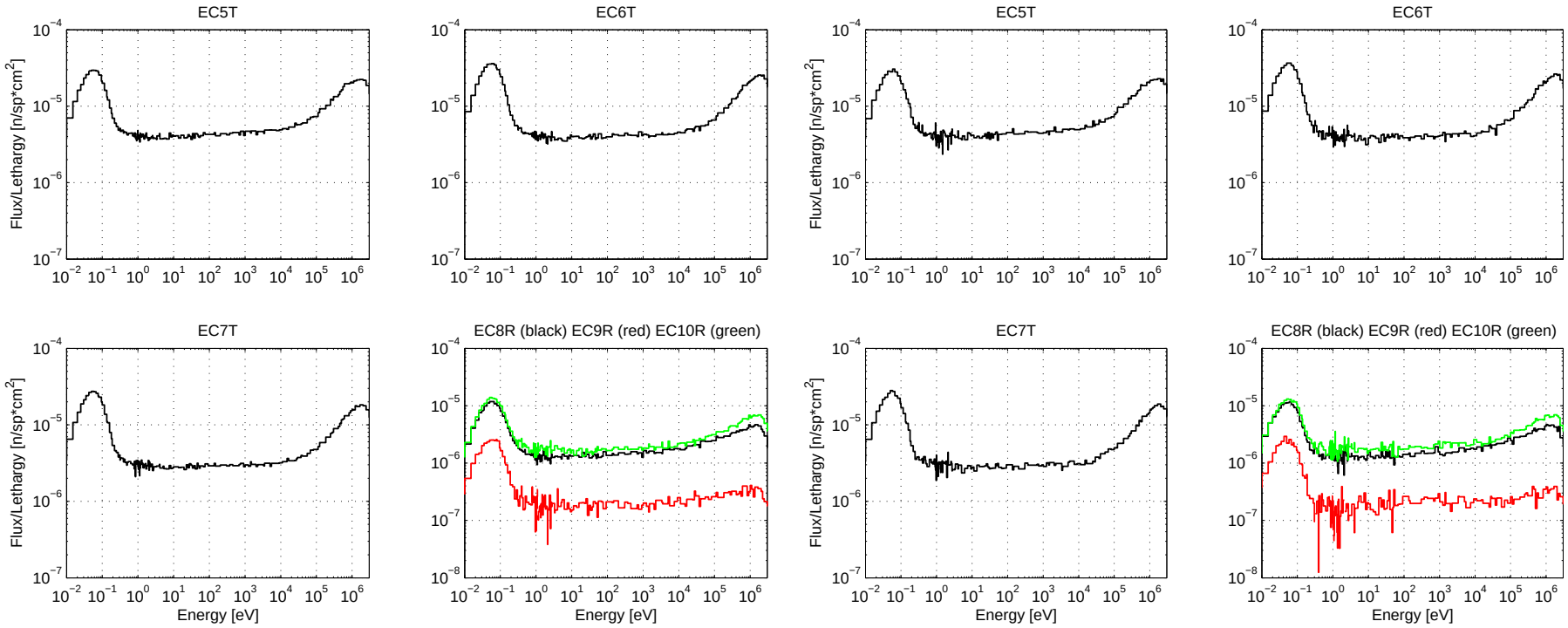

Figure 35. Neutron spectrum of the YALINA-Booster configuration with 1141 EK-10 fuel rods in the experimental channels of the thermal and reflector zones for the fission neutron source calculated by MCNPX (left) and MONK (right) using 172 neutron energy group structure, The spectra were calculated at the center of the active fuel length and over 10 cm experimental channel length for EC5T, EC6T, and EC7T, and 5 cm experimental channel length for EC10R

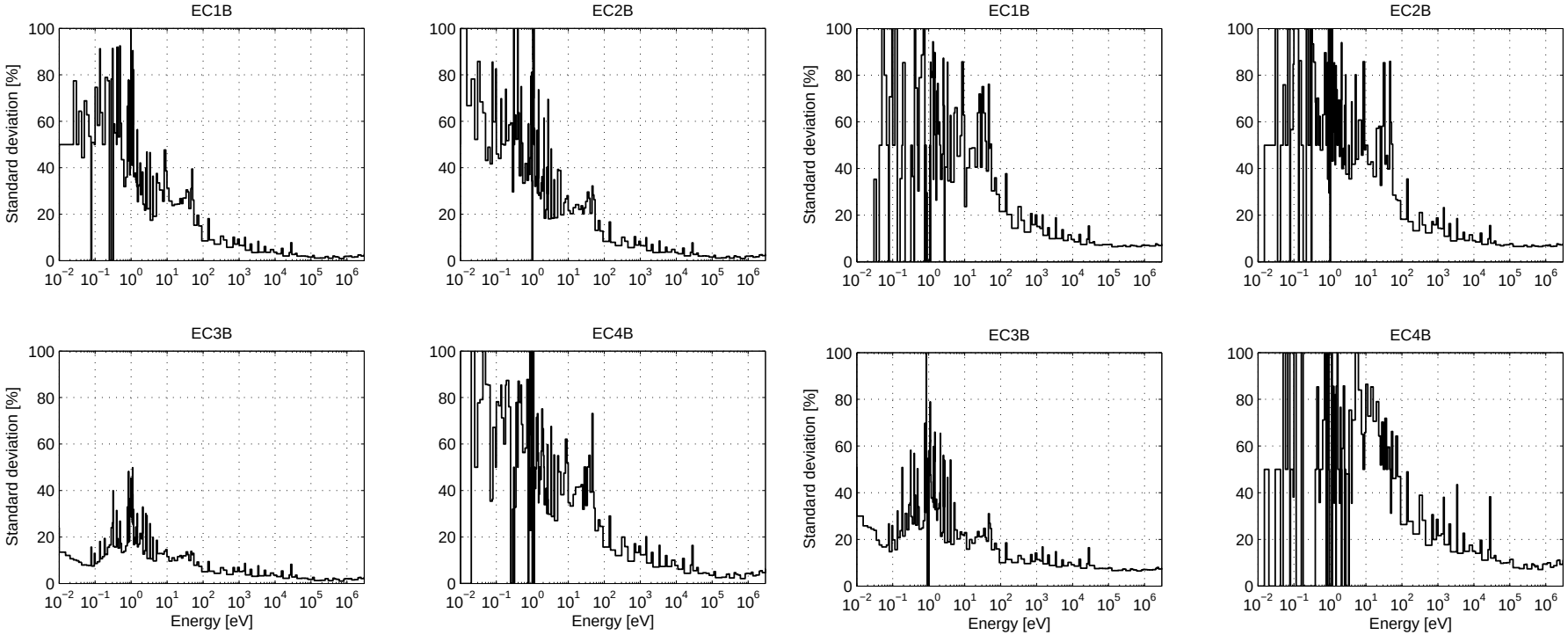

Figure 36. Standard deviation of the 172 groups neutron spectrum shown in Figure 34 in the experimental channels of the fast zone for the fission neutron source calculated by MCNPX (left) and MONK (right)

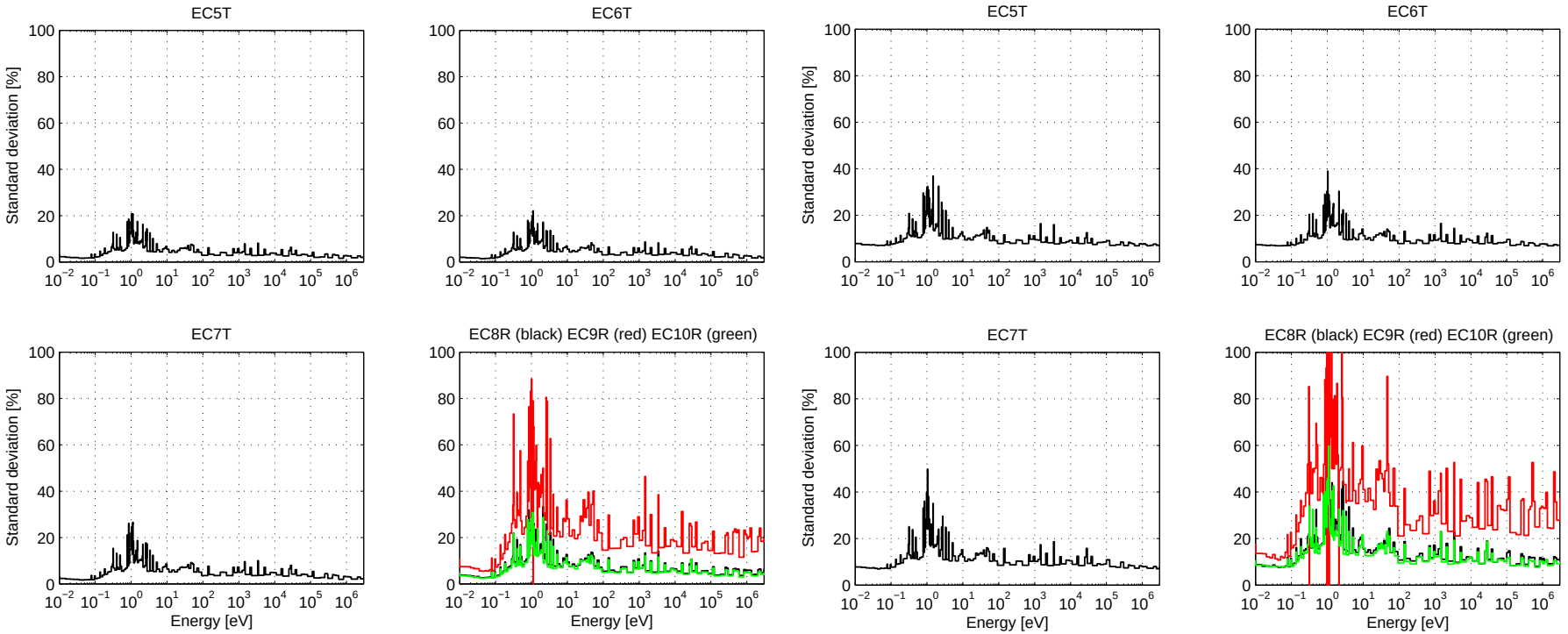

Figure 37. Standard deviation of the 172 groups neutron spectrum shown in Figure 35 in the experimental channels of the thermal and reflector zones for the fission neutron source calculated by MCNPX (left) and MONK (right)

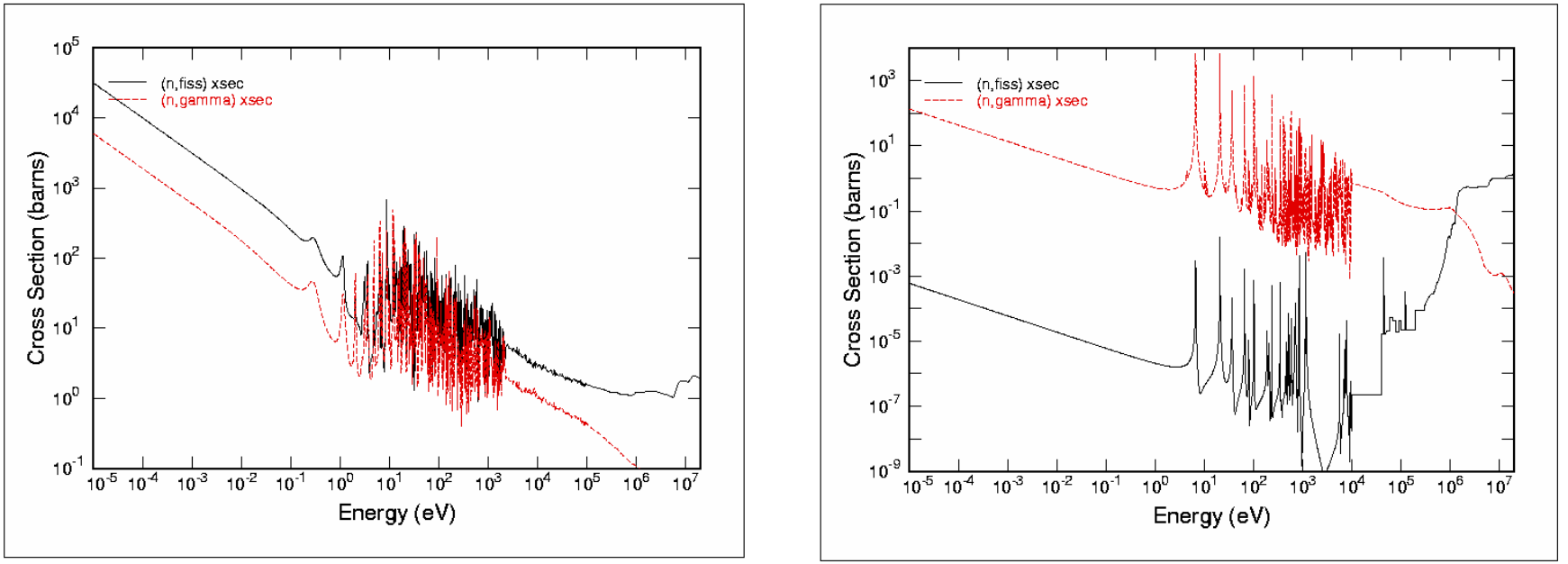

Figure 38. Microscopic cross sections of ^{235}U (left) and ^{238}U (right) from JEFF-3.0

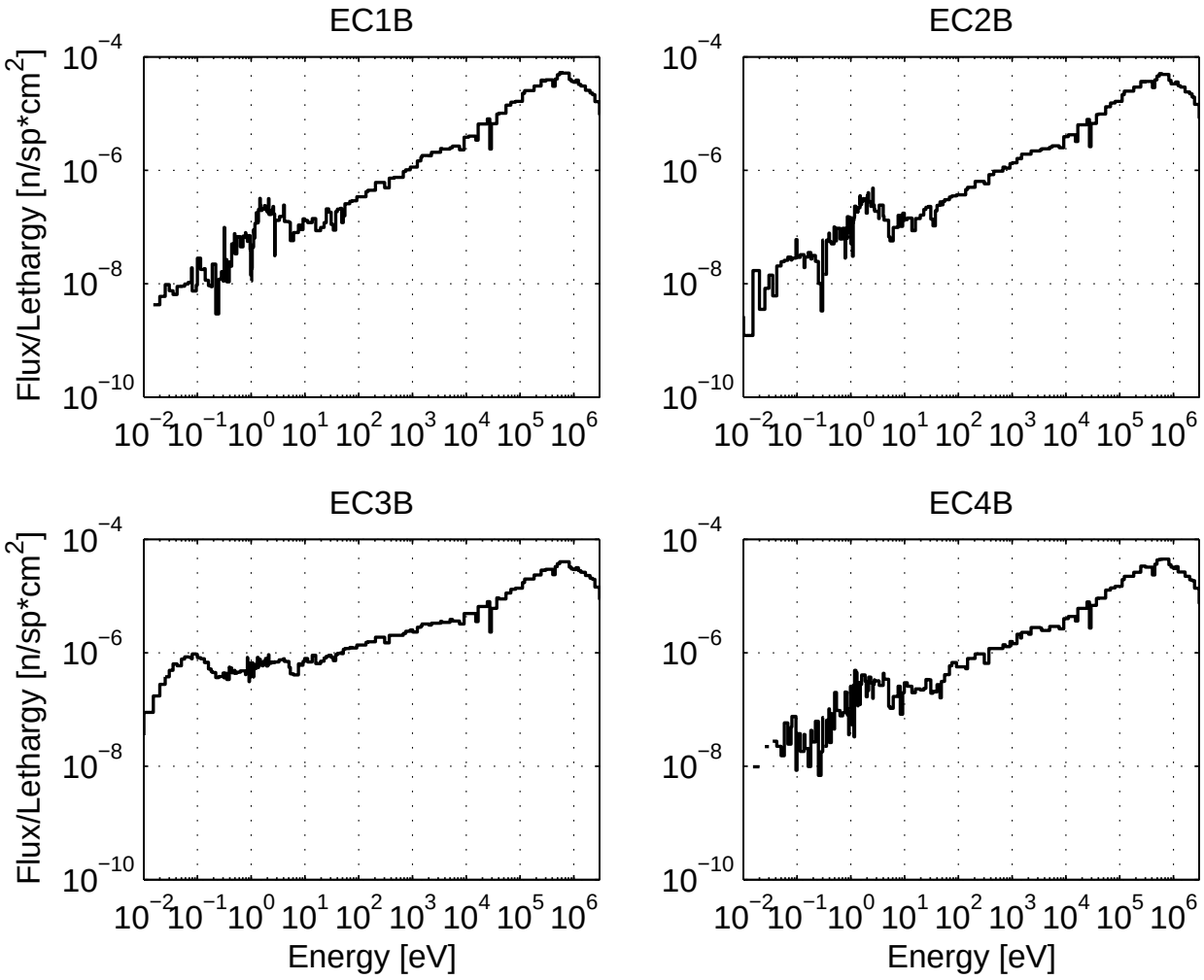

Figure 39. Neutron spectrum of the YALINA-Booster configuration with 902 EK-10 fuel rods in the experimental channels of the fast zone for the fission neutron source calculated by MCNPX using 172 neutron energy group structure, The spectra were calculated at the center of the active fuel length and over 5 cm experimental channel length

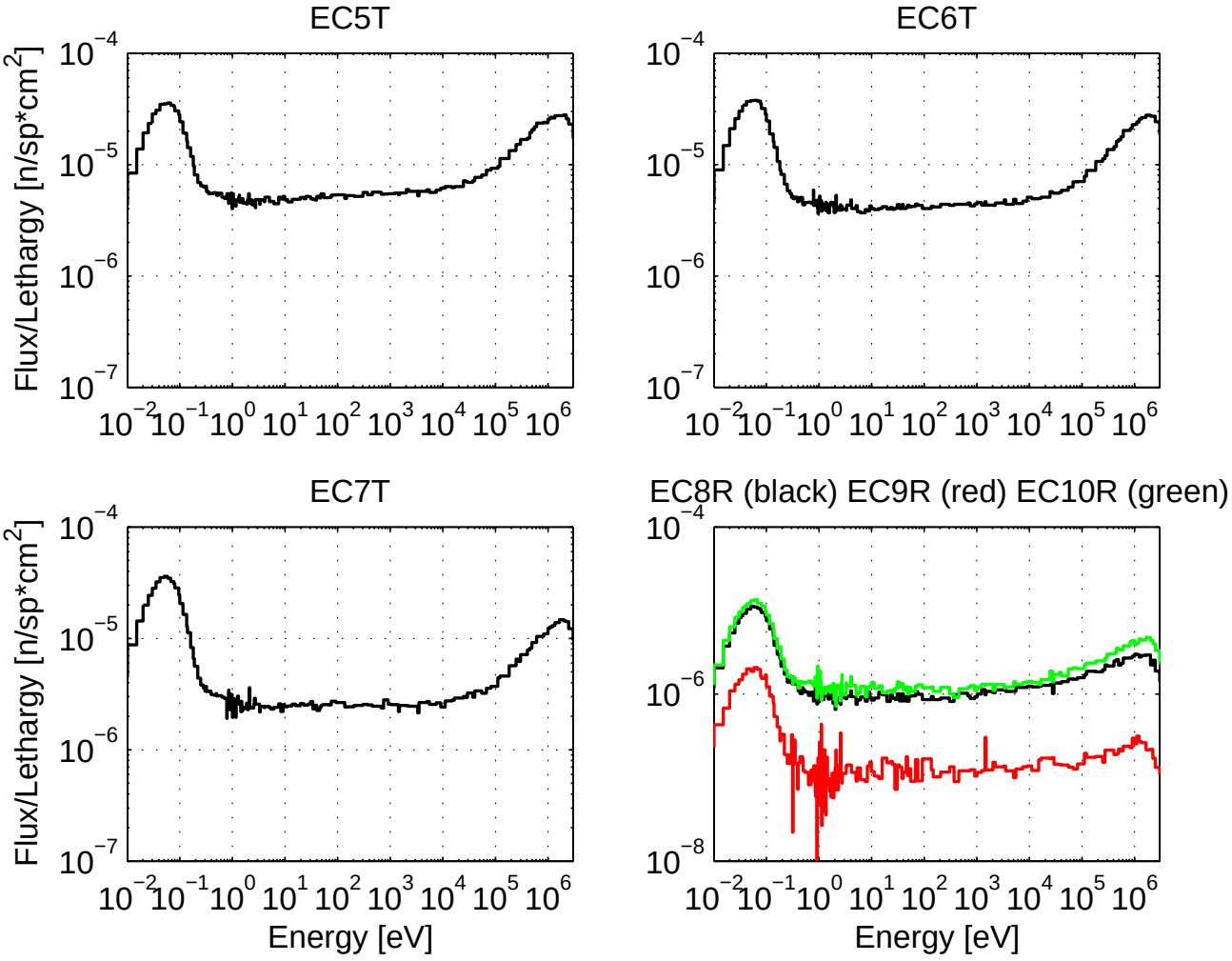

Figure 40. Neutron spectrum of the YALINA-Booster configuration with 902 EK-10 fuel rods in the experimental channels of the thermal zone for the fission neutron source calculated by MCNPX using 172 neutron energy group structure, The spectra were calculated at the center of the active fuel length and over 10 cm experimental channel length for EC5T, EC6T, and EC7T, and 5 cm experimental channel length for EC10R

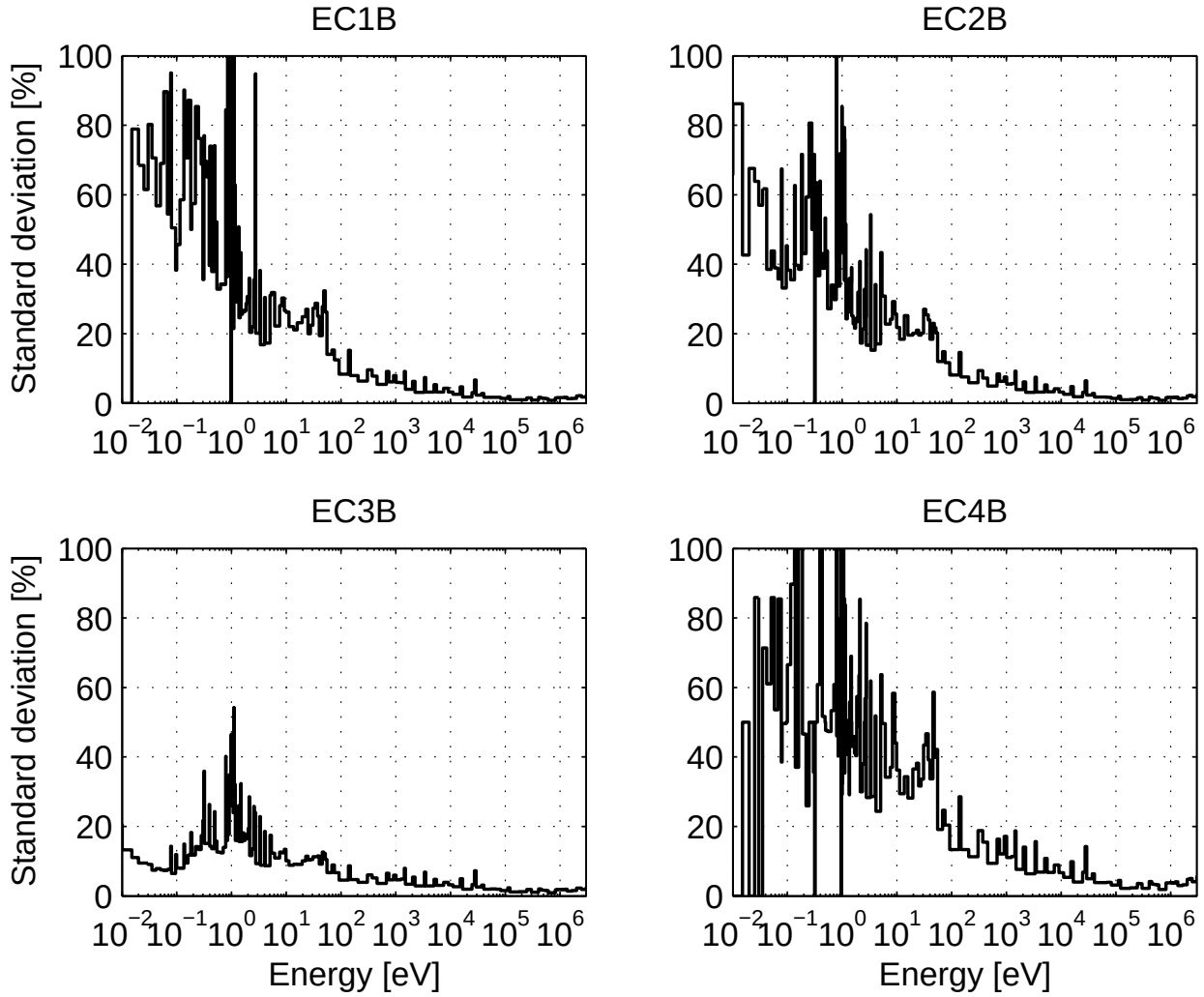

Figure 41. Standard deviation of the 172 groups neutron spectrum shown in Figure 39 in the experimental channels of the fast zone for the fission neutron source calculated by MCNPX

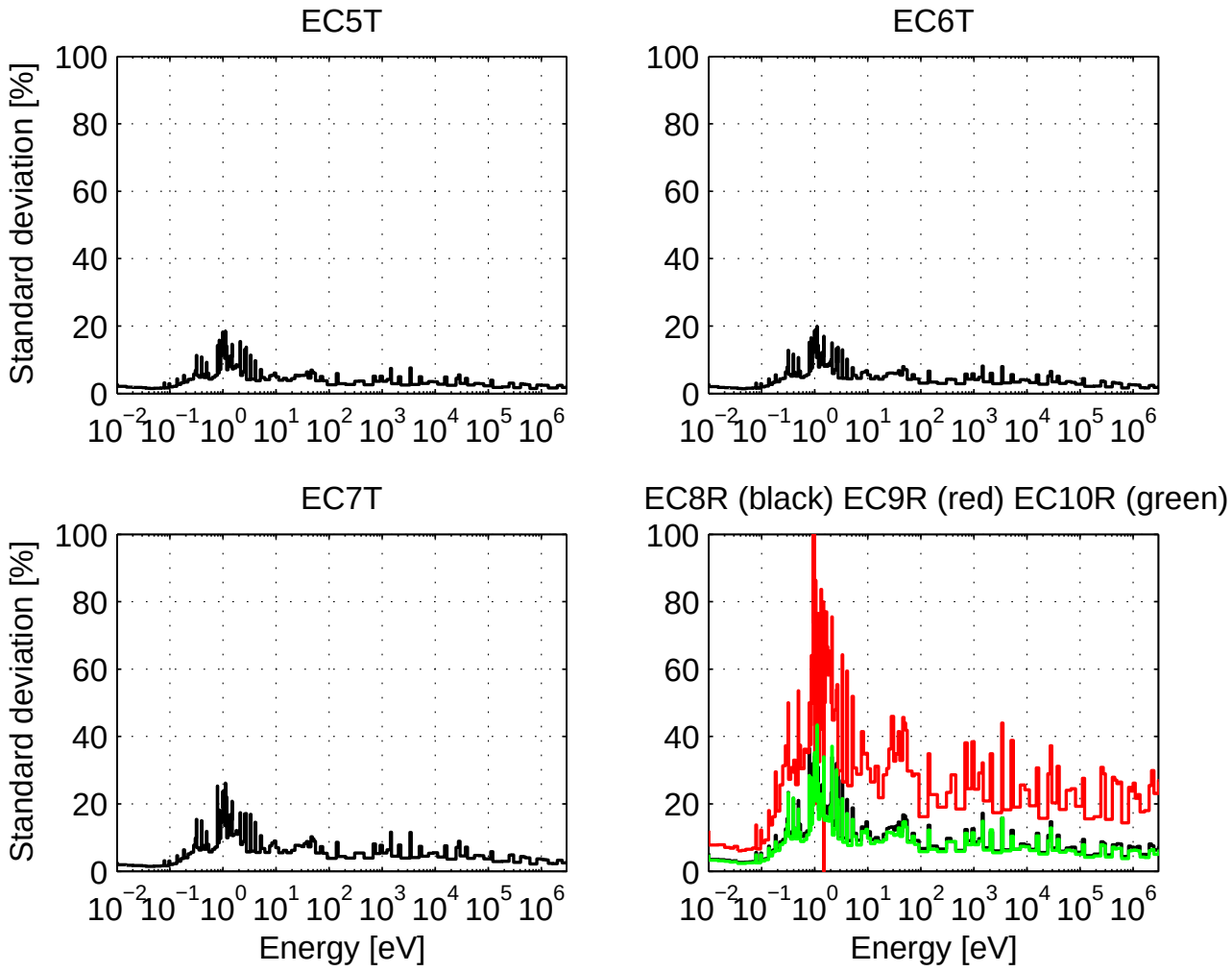

Figure 42. Standard deviation of the 172 groups neutron spectrum shown in Figure 40 in the experimental channels of the thermal and reflector zones for the fission neutron source calculated by MCNPX

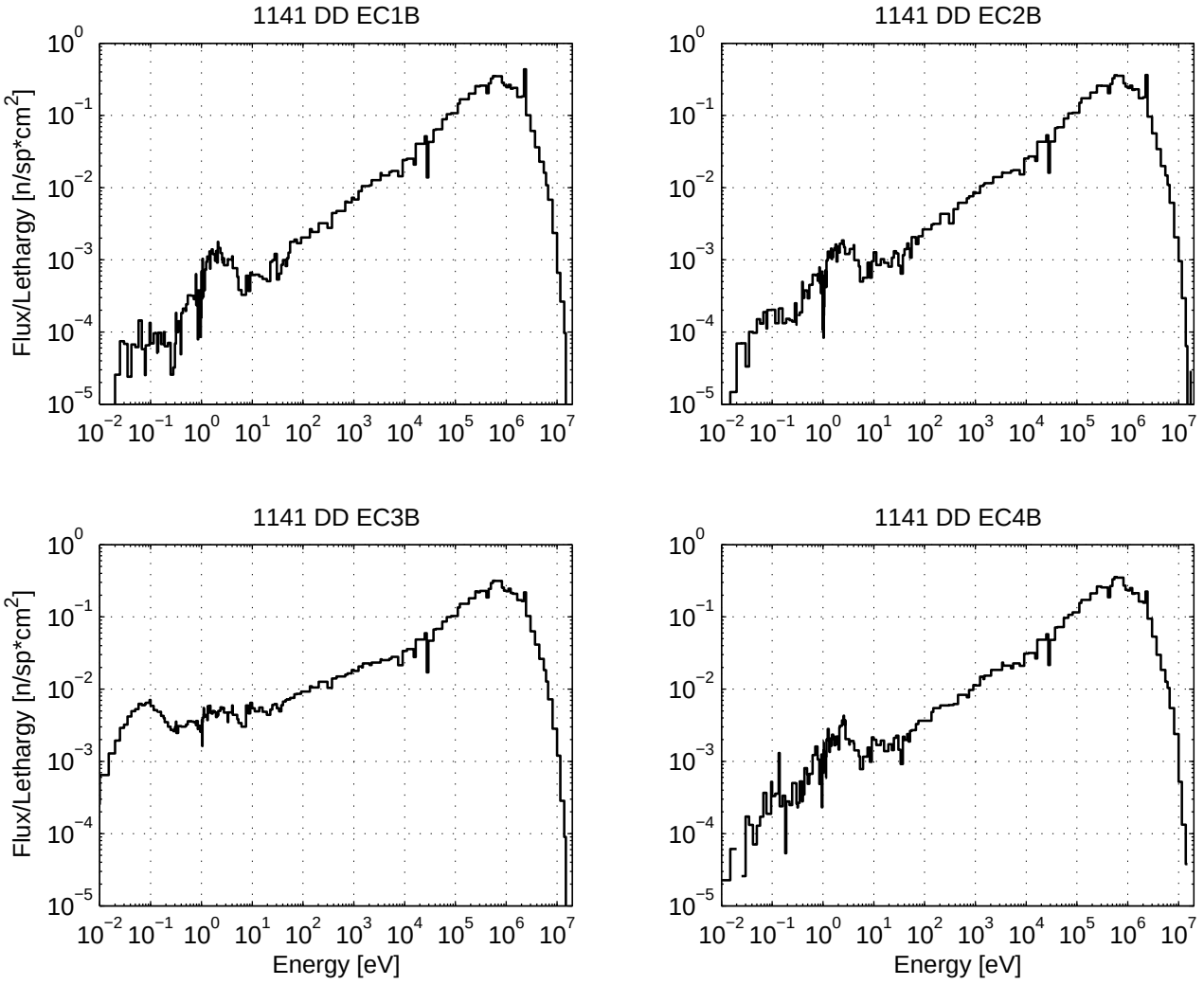

Figure 43. Neutron spectrum of the YALINA-Booster configuration with 1141 EK-10 fuel rods in the experimental channels of the fast zone for the D-D neutron source calculated by MCNPX using 172 neutron energy group structure, The spectra were calculated at the center of the active fuel length and over 10 cm experimental channel length

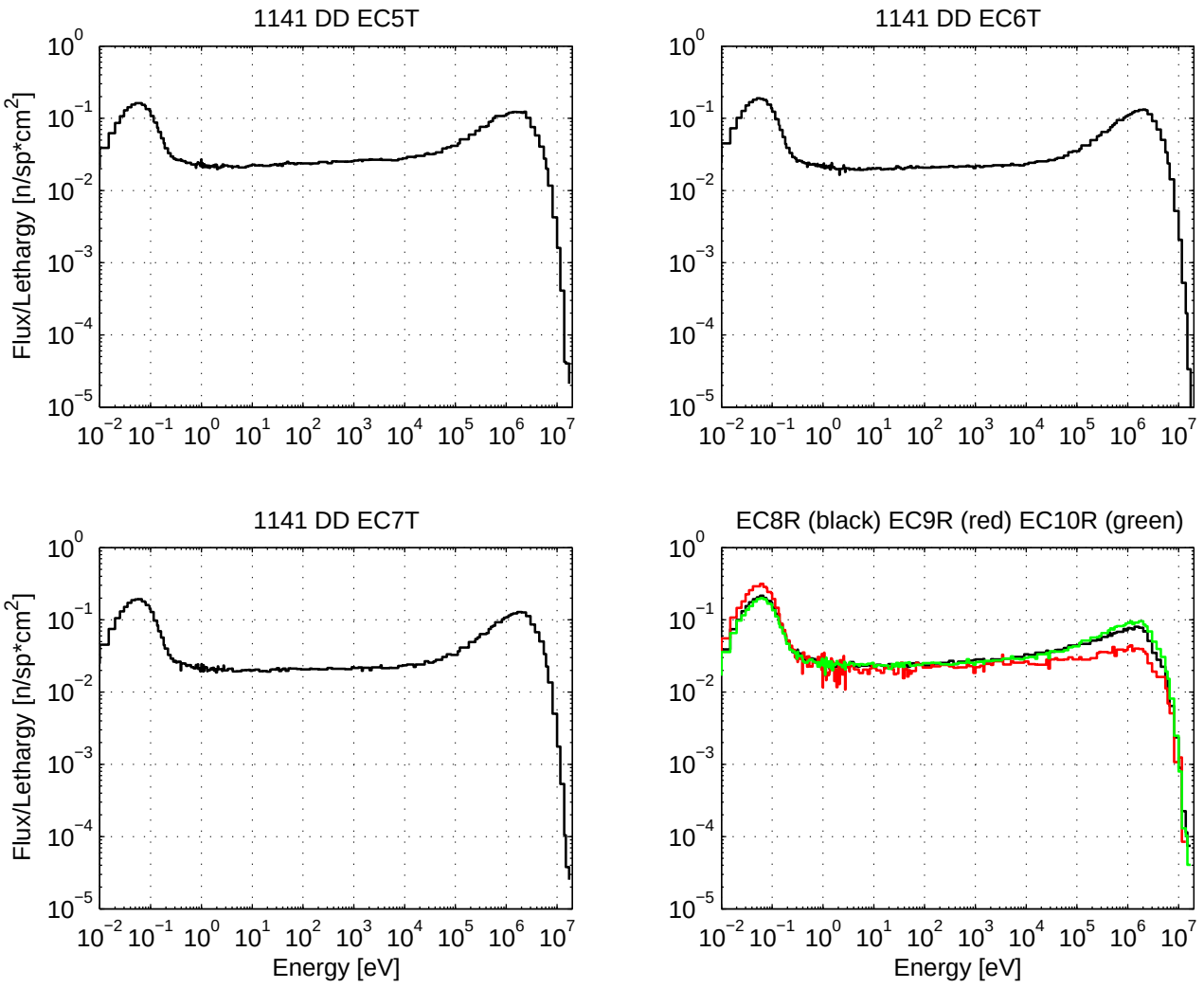

Figure 44. Neutron spectrum of the YALINA-Booster configuration with 1141 EK-10 fuel rods in the experimental channels of the thermal and reflector zones for the D-D neutron source calculated by MCNPX using 172 neutron energy group structure, The spectra were calculated at the center of the active fuel length and over 10 cm experimental channel length for EC5T, EC6T, and EC7T, and 5 cm experimental channel length for EC10R

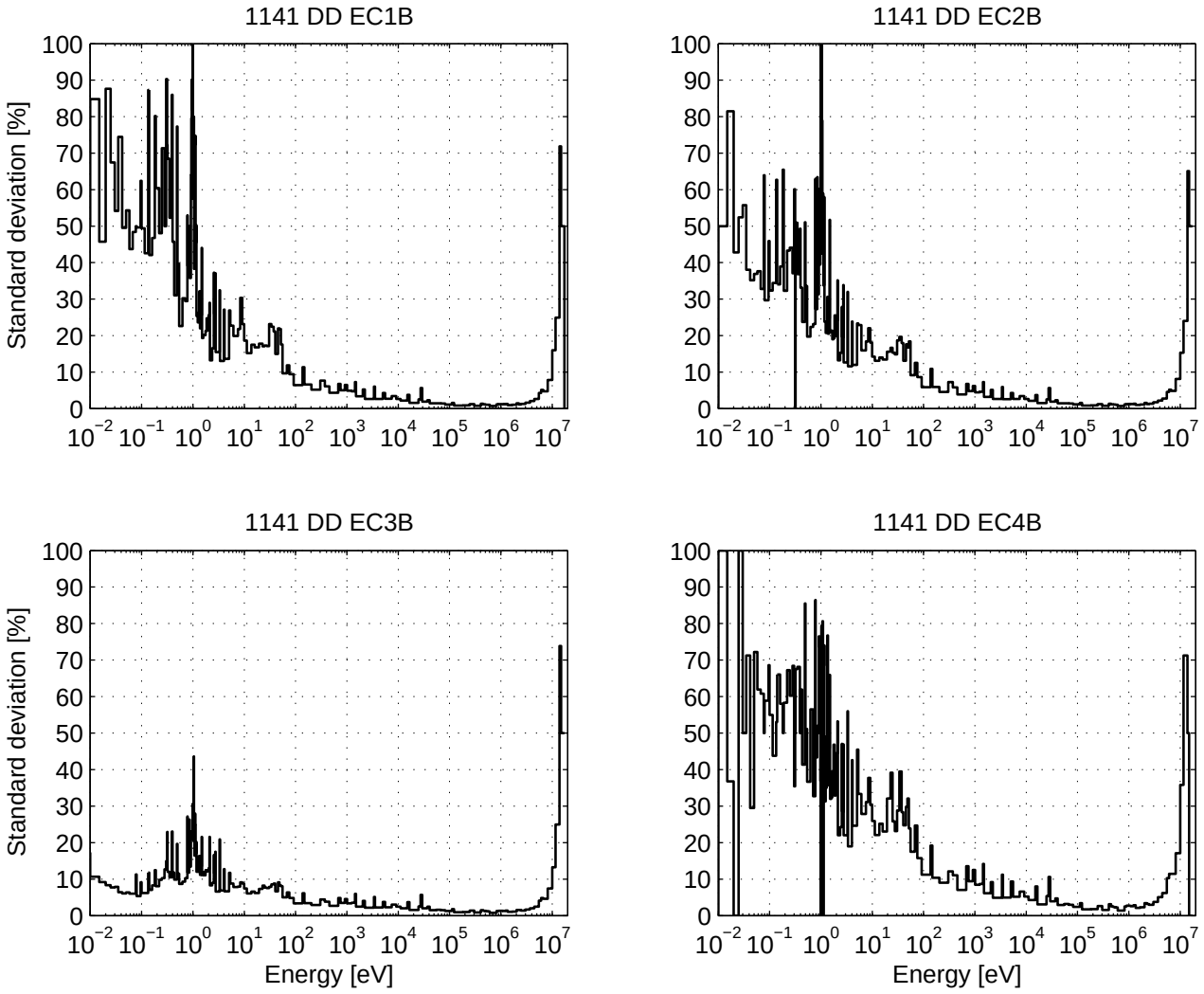

Figure 45. Standard deviation of the 172 groups neutron spectrum shown in Figure 43 in the experimental channels of the fast zone for the D-D neutron source calculated by MCNPX

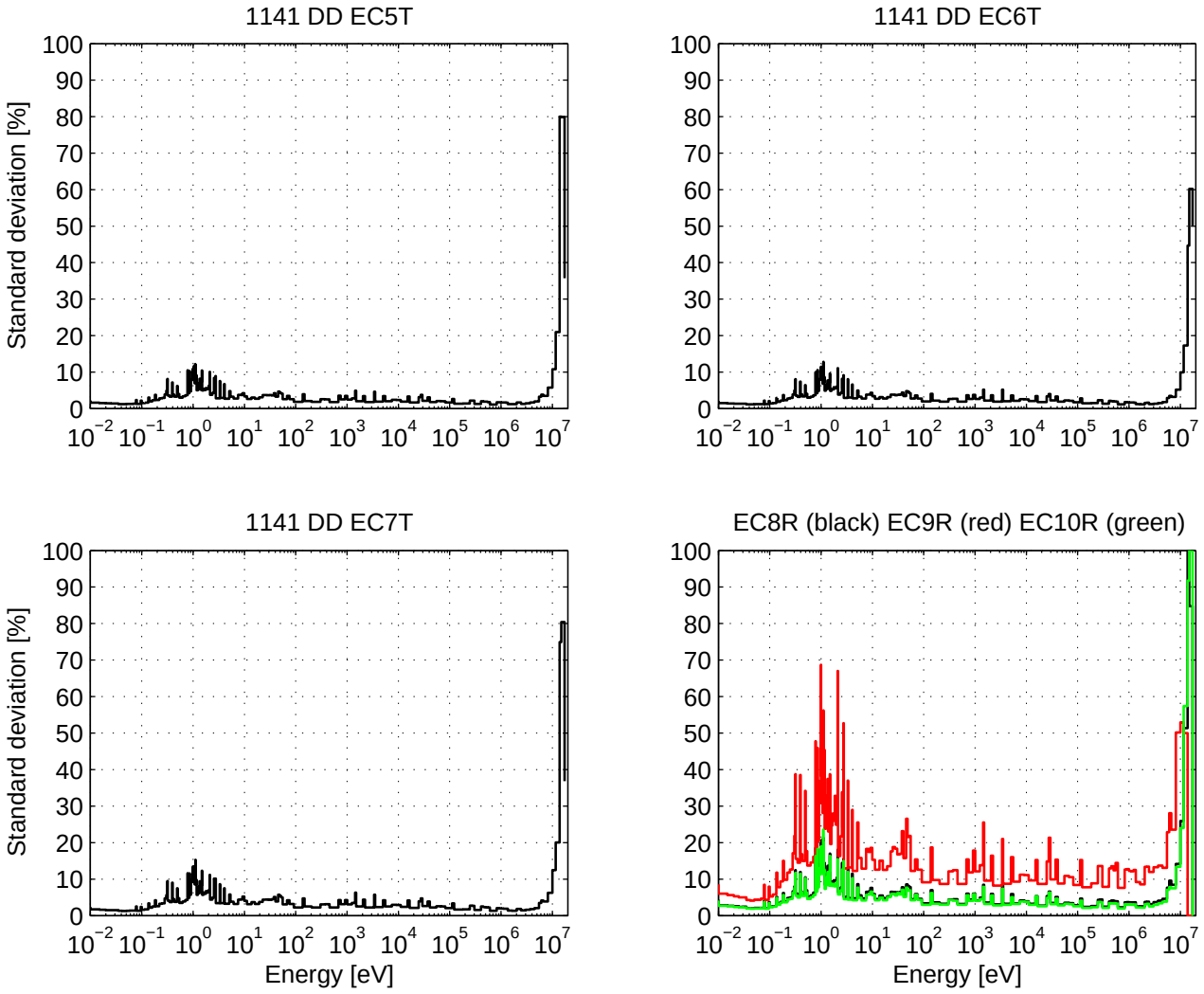

Figure 46. Standard deviation of the 172 groups neutron spectrum shown in Figure 44 in the experimental channels of the thermal and reflector zones for the D-D neutron source calculated by MCNPX

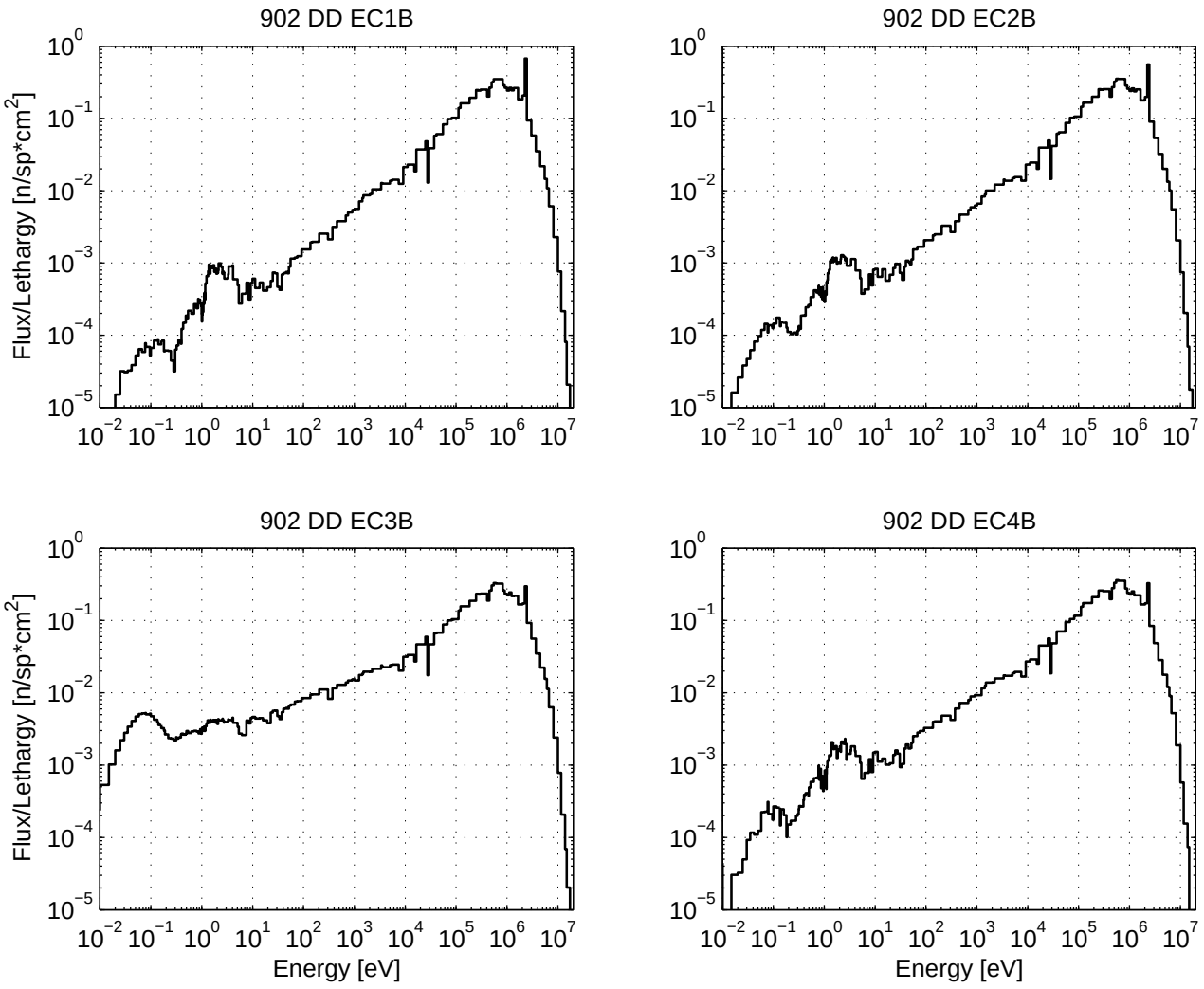

Figure 47. Neutron spectrum of the YALINA-Booster configuration with 902 EK-10 fuel rods in the experimental channels of the fast zone for the D-D neutron source calculated by MCNPX using 172 neutron energy group structure, The spectra were calculated at the center of the active fuel length and over 10 cm experimental channel length

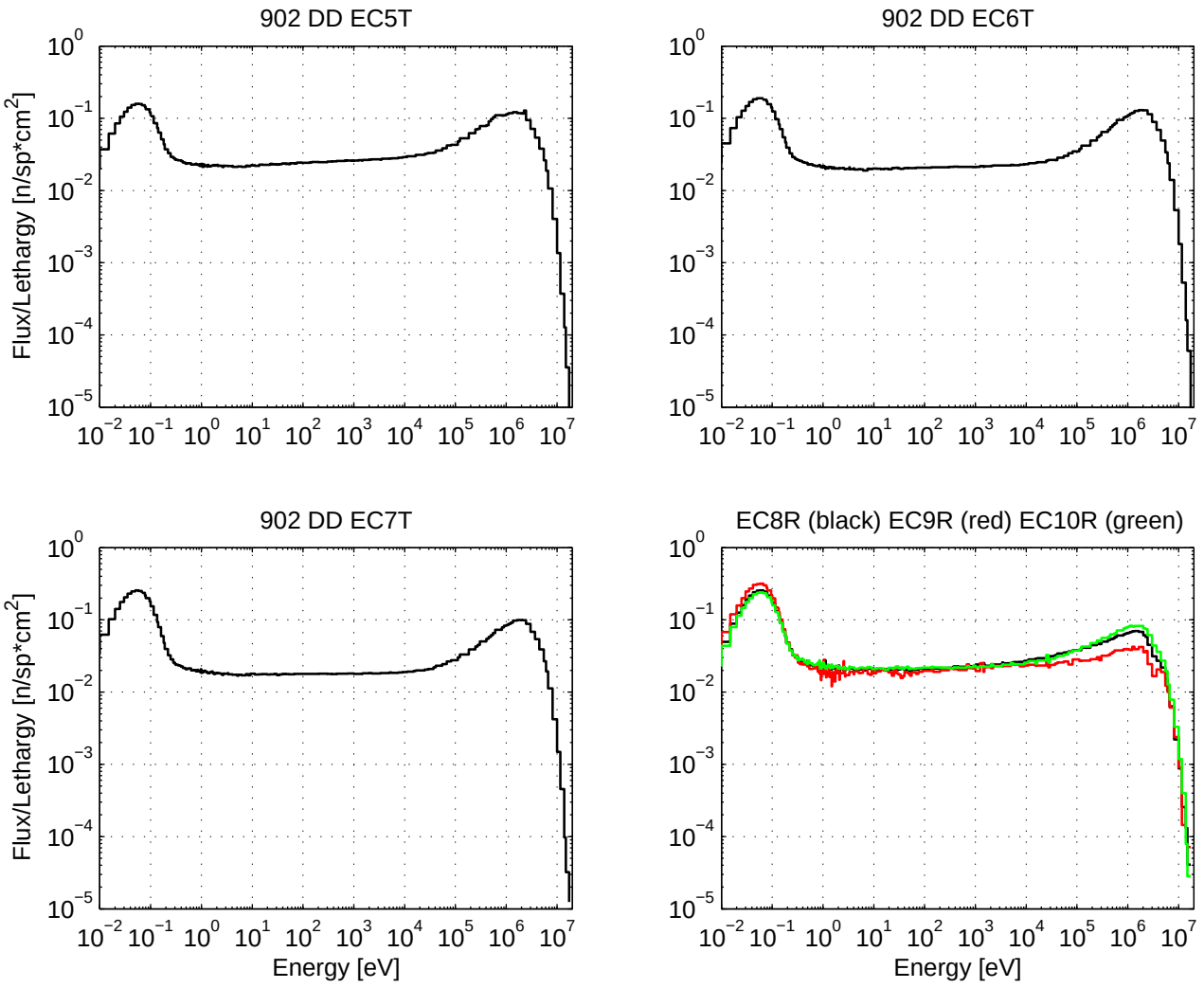

Figure 48. Neutron spectrum of the YALINA-Booster configuration with 902 EK-10 fuel rods in the experimental channels of the thermal and reflector zones for the D-D neutron source calculated by MCNPX using 172 neutron energy group structure, The spectra were calculated at the center of the active fuel length and over 10 cm experimental channel length for EC5T, EC6T, and EC7T, and 5 cm experimental channel length for EC10R

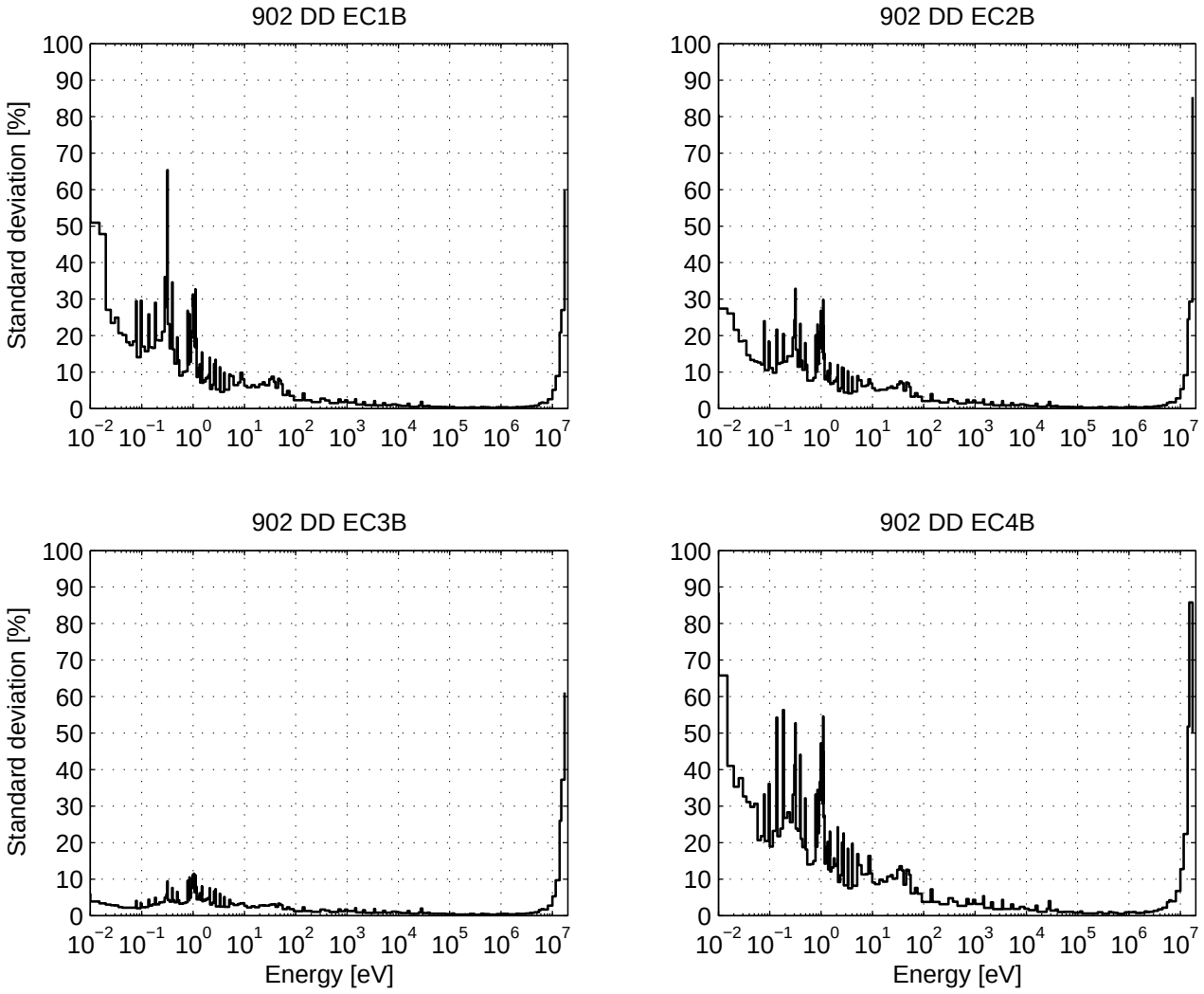

Figure 49. Standard deviation of the 172 groups neutron spectrum shown in Figure 47 in the experimental channels of the fast zone for the D-D neutron source calculated by MCNP

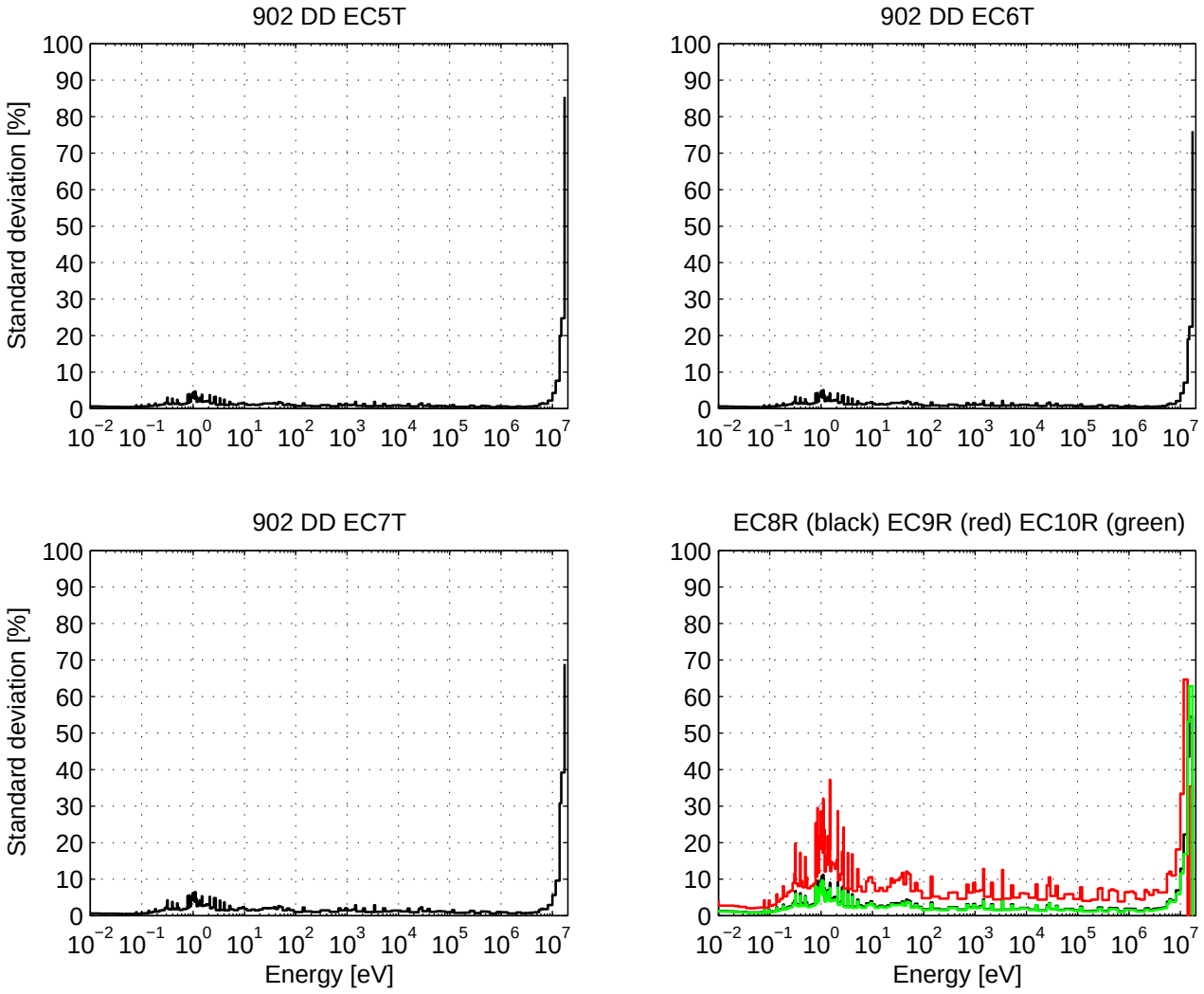

Figure 50. Standard deviation of the 172 groups neutron spectrum shown in Figure 48 in the experimental channels of the thermal and reflector zones for the D-D neutron source calculated by MCNPX

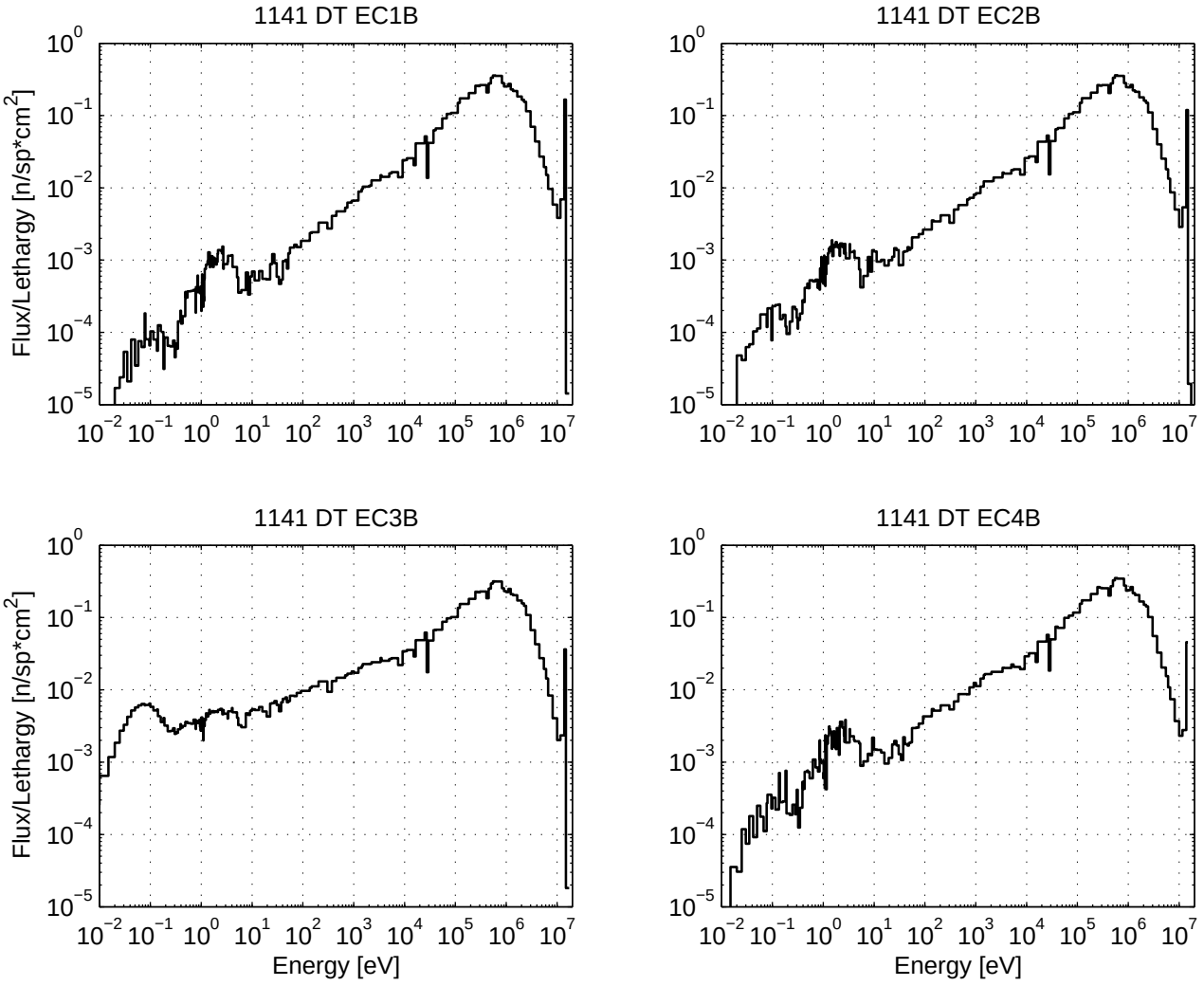

Figure 51. Neutron spectrum of the YALINA-Booster configuration with 1141 EK-10 fuel rods in the experimental channels of the fast zone for the D-T neutron source calculated by MCNPX using 172 neutron energy group structure, The spectra were calculated at the center of the active fuel length and over 10 cm experimental channel length

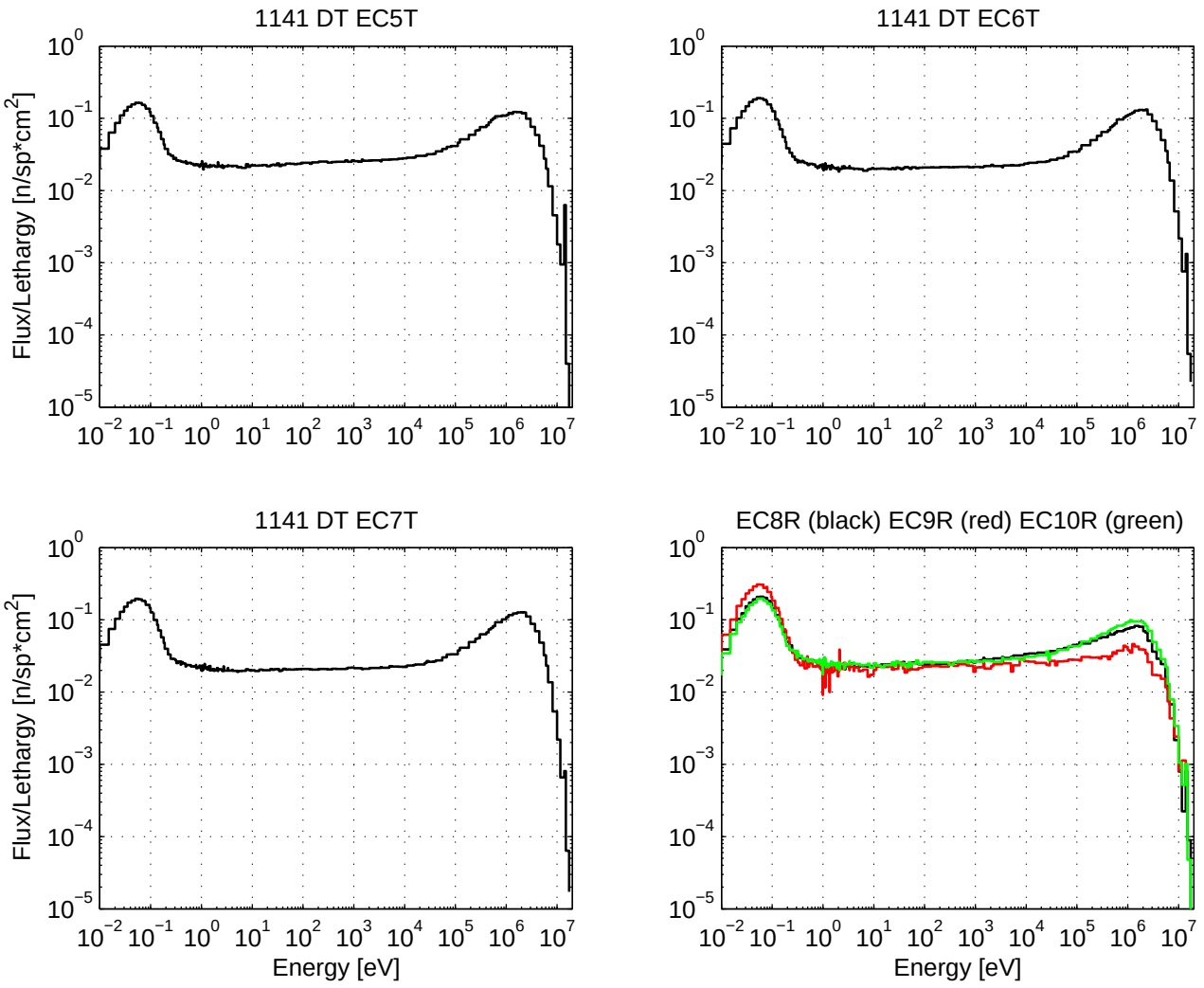

Figure 52. Neutron spectrum of the YALINA-Booster configuration with 1141 EK-10 fuel rods in the experimental channels of the thermal and reflector zones for the D-T neutron source calculated by MCNPX using 172 neutron energy group structure, The spectra were calculated at the center of the active fuel length and over 10 cm experimental channel length for EC5T, EC6T, and EC7T, and 5 cm experimental channel length for EC10R

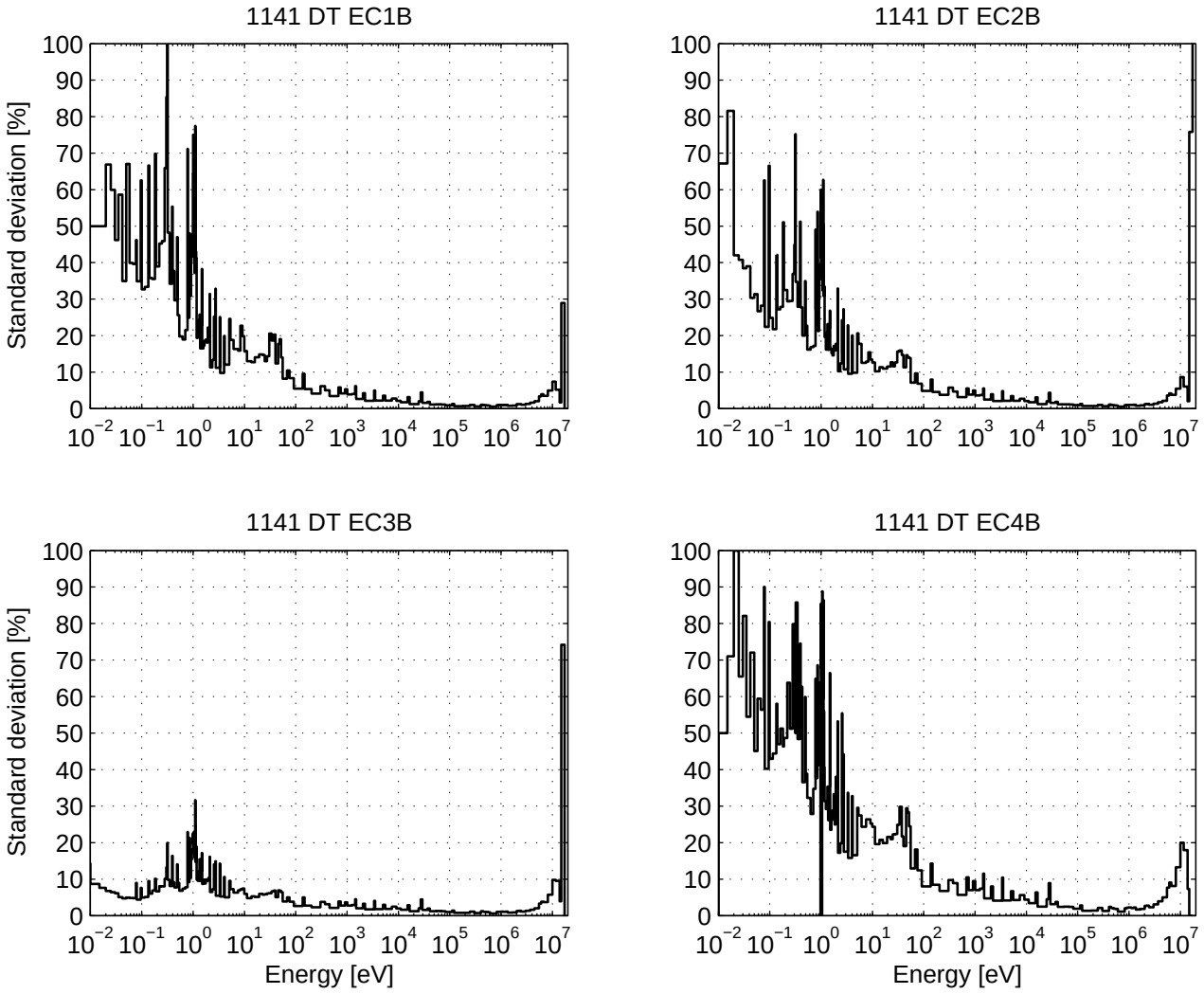

Figure 53. Standard deviation of the 172 groups neutron spectrum shown in Figure 51 in the experimental channels of the fast zone for the D-D neutron source calculated by MCNPX

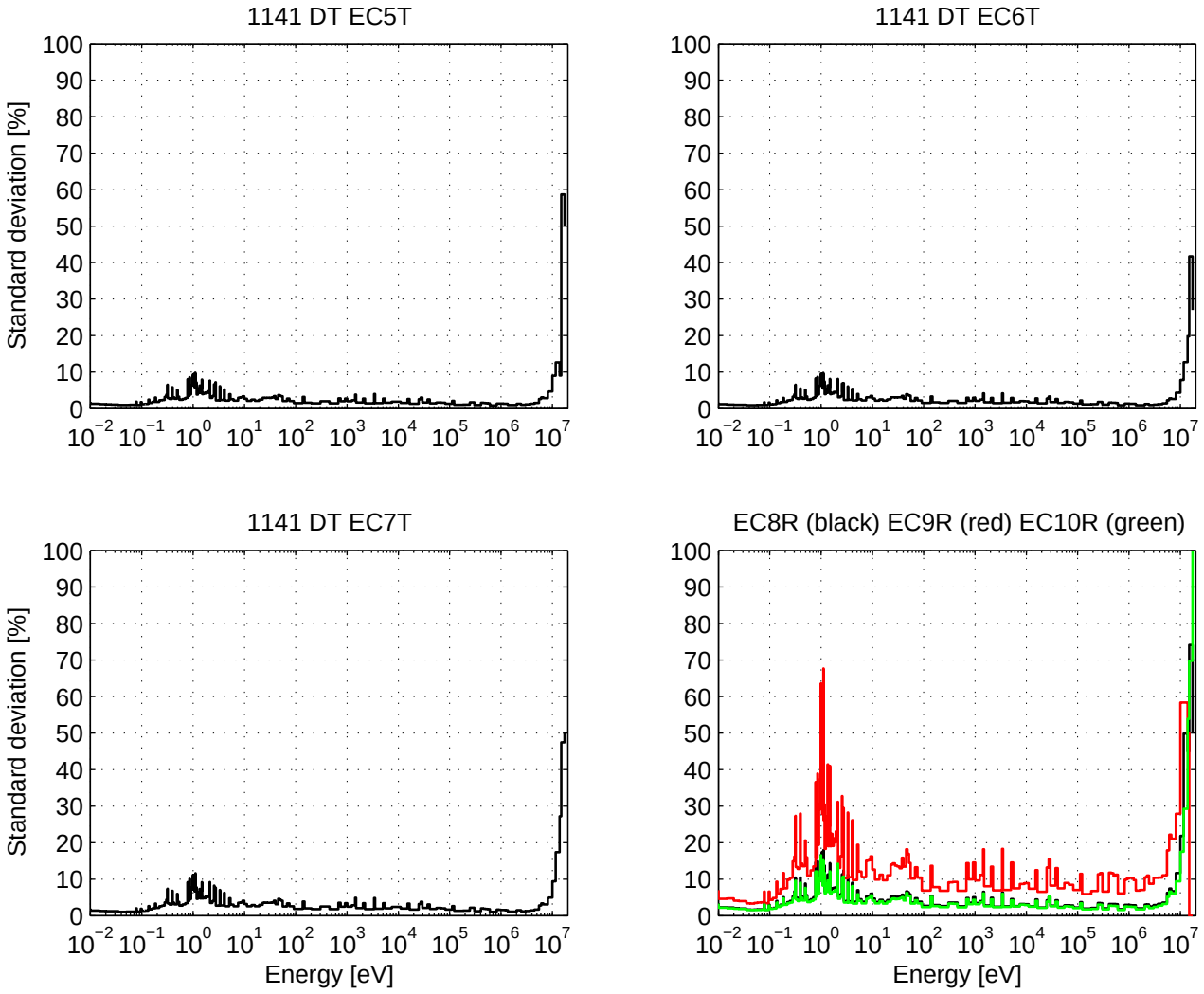

Figure 54. Standard deviation of the 172 groups neutron spectrum shown in Figure 52 in the experimental channels of the thermal and reflector zones for the D-T neutron source calculated by MCNPX

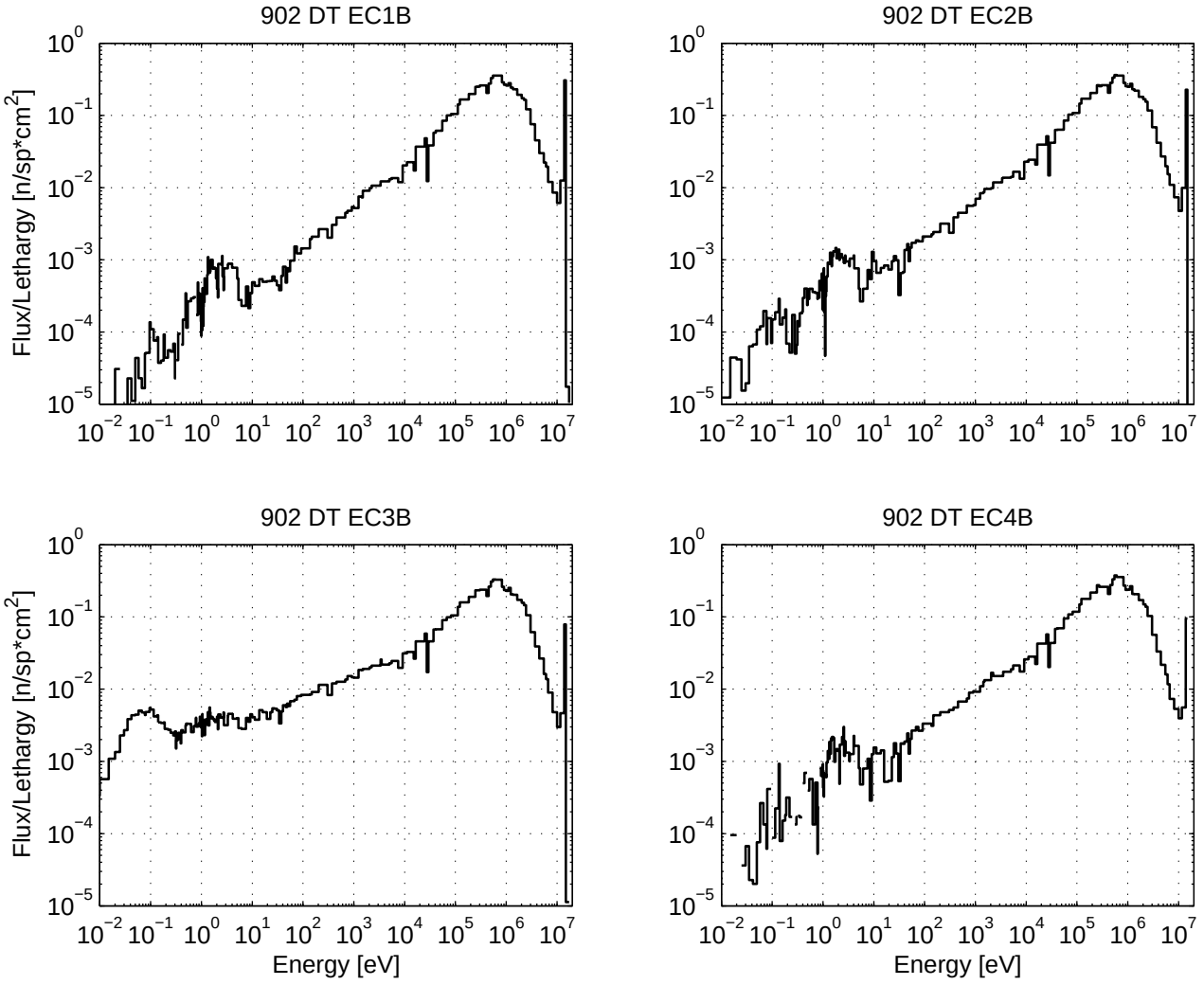

Figure 55. Neutron spectrum of the YALINA-Booster configuration with 902 EK-10 fuel rods in the experimental channels of the fast zone for the D-T neutron source calculated by MCNPX using 172 neutron energy group structure, The spectra were calculated at the center of the active fuel length and over 10 cm experimental channel length

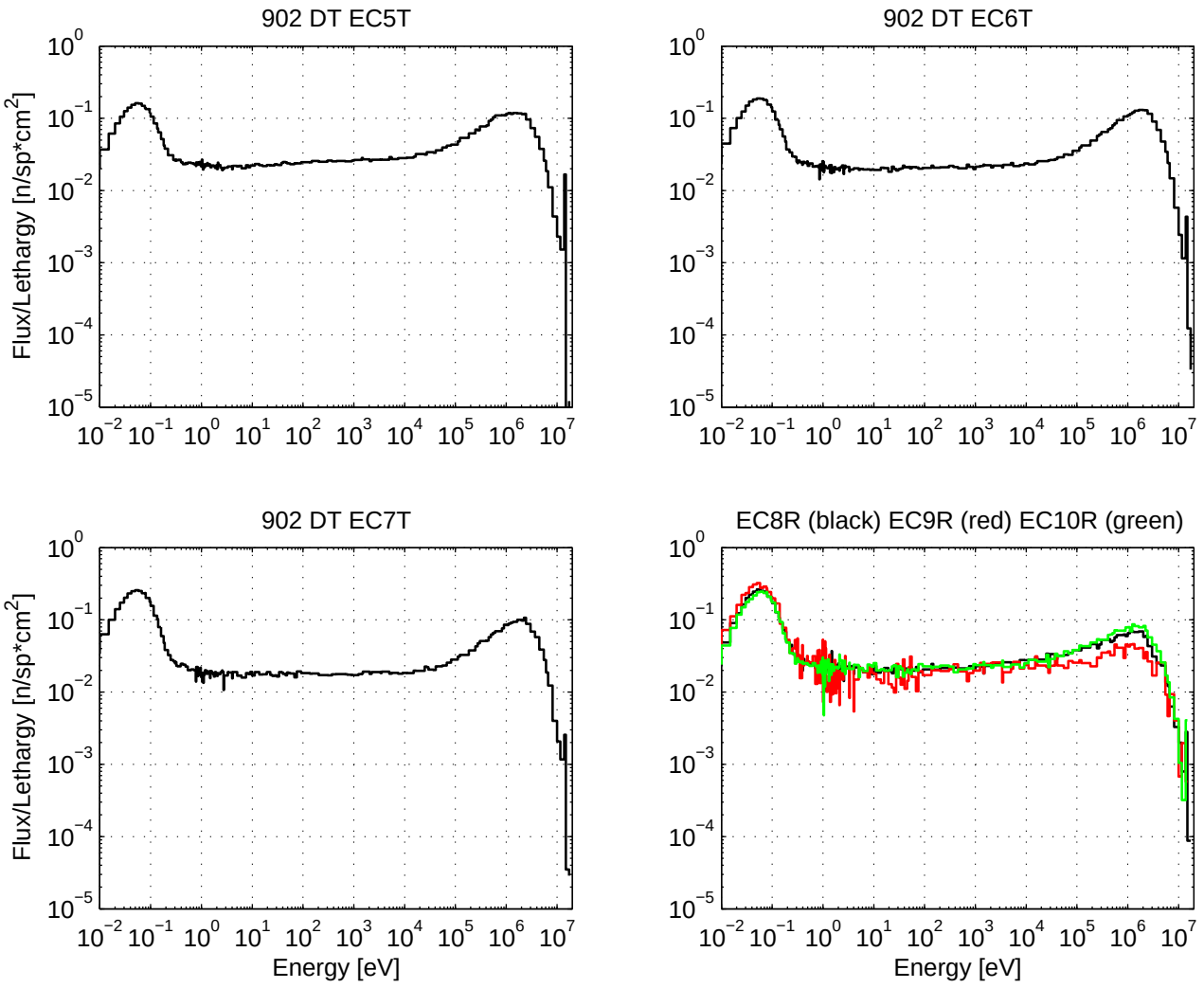

Figure 56. Neutron spectrum of the YALINA-Booster configuration with 902 EK-10 fuel rods in the experimental channels of the thermal and reflector zones for the D-T neutron source calculated by MCNPX using 172 neutron energy group structure, The spectra were calculated at the center of the active fuel length and over 10 cm experimental channel length for EC5T, EC6T, and EC7T, and 5 cm experimental channel length for EC10R

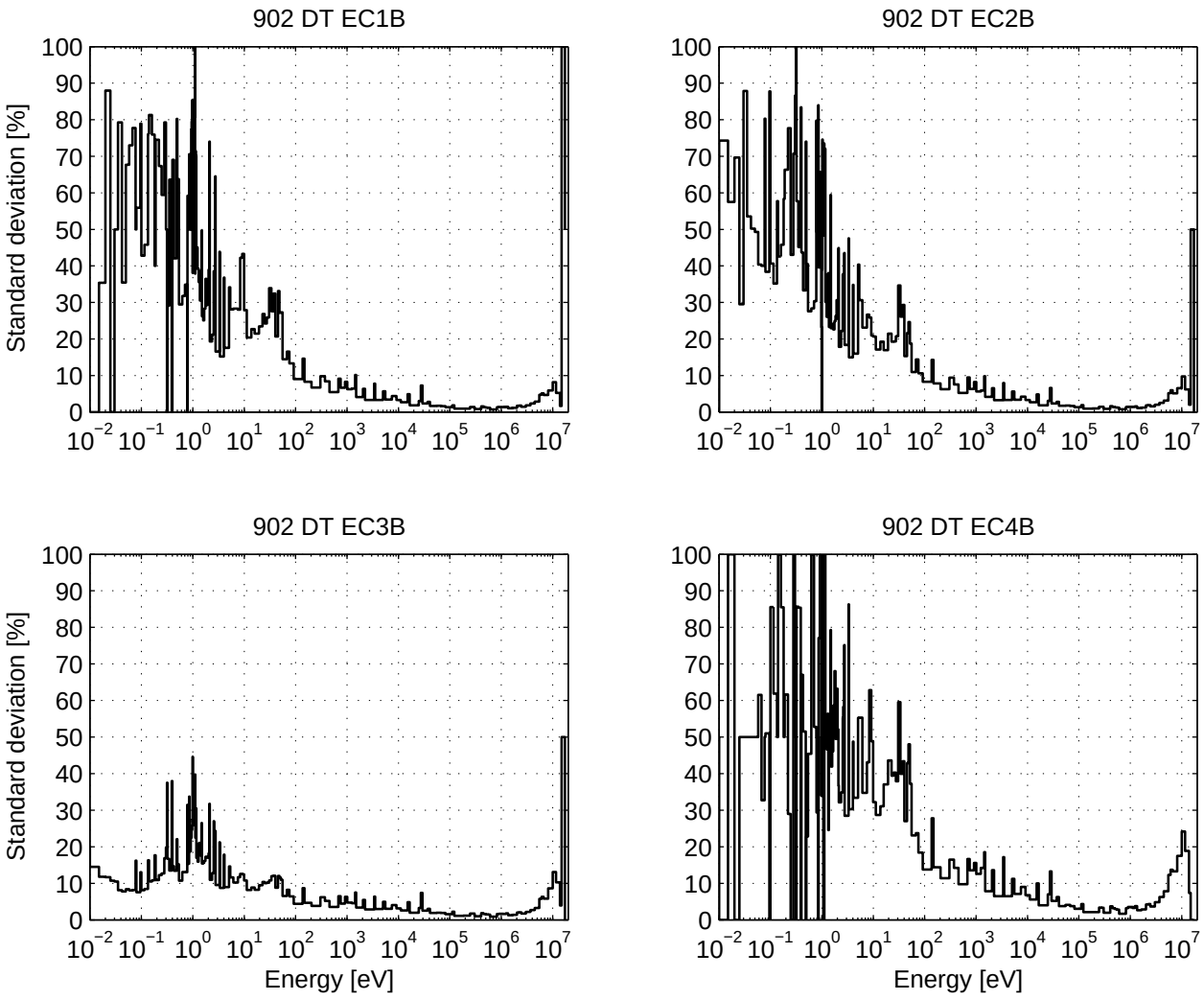

Figure 57. Standard deviation of the 172 groups neutron spectrum shown in Figure 55 in the experimental channels of the fast zone for the D-T neutron source calculated by MCNP

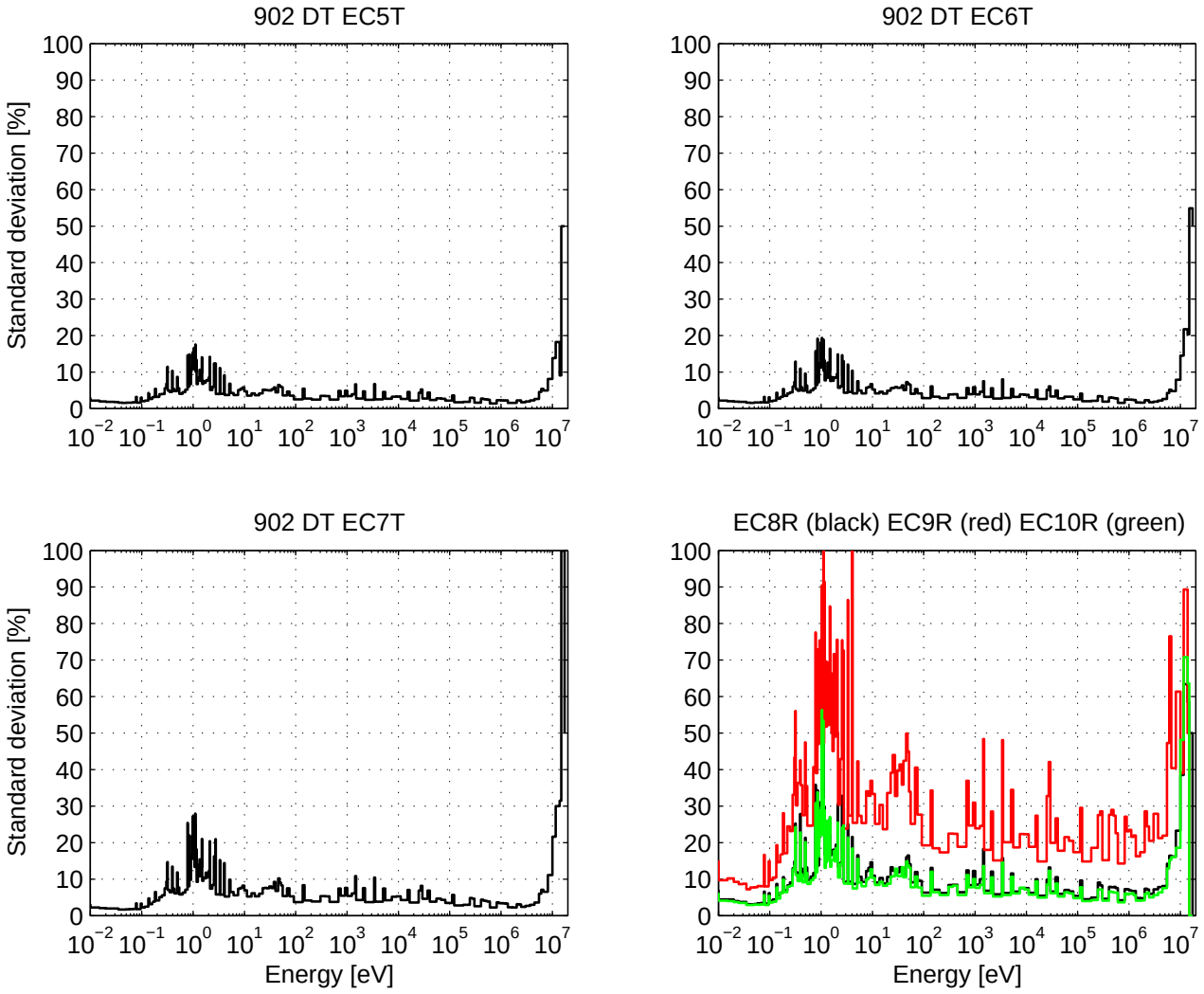

Figure 58. Standard deviation of the 172 groups neutron spectrum shown in Figure 56 in the experimental channels of the thermal and reflector zones for the D-T neutron source calculated by MCNPX

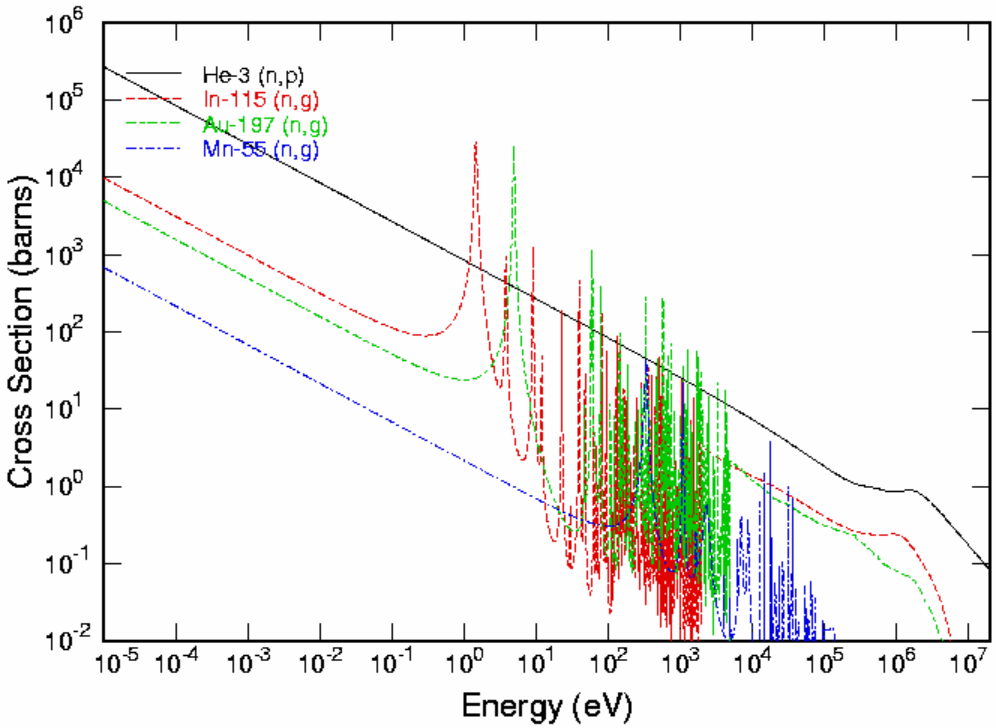

Figure 59. ^{3}He (n,p) microscopic cross sections and (n,γ) microscopic cross sections of ^{115}In, ^{197}Au and ^{55}Mn from JEFF-3.0

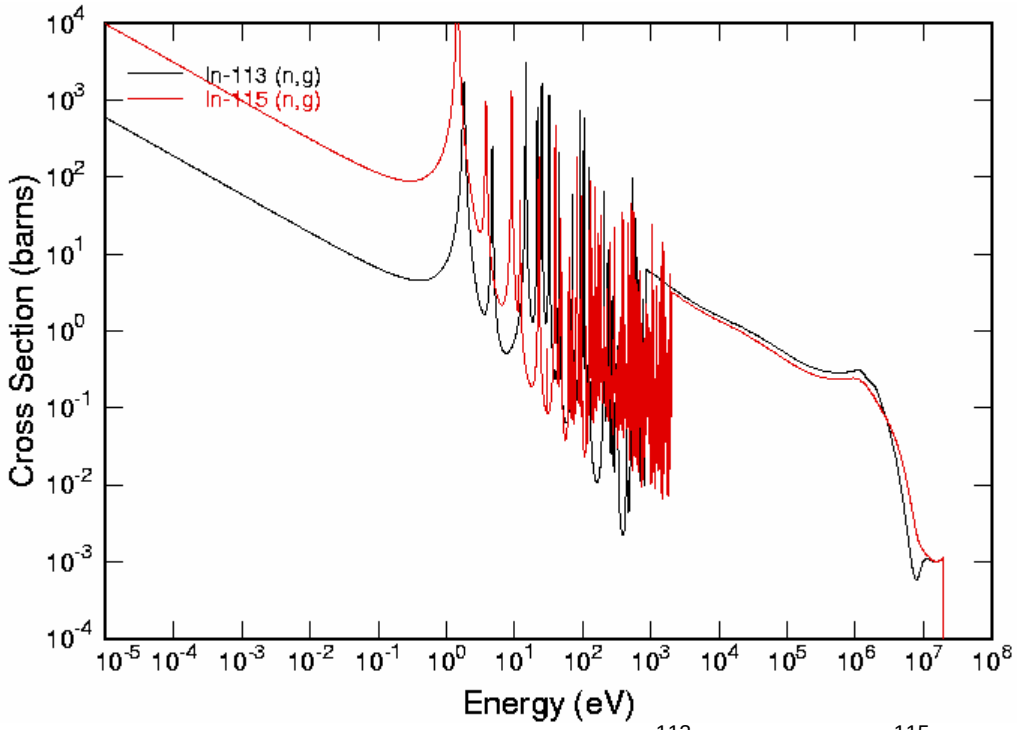

Figure 60. Natural In(n,γ) microscopic cross sections of ^{113}In (4.3%) and ^{115}In (95.7%) from JEFF-3.0

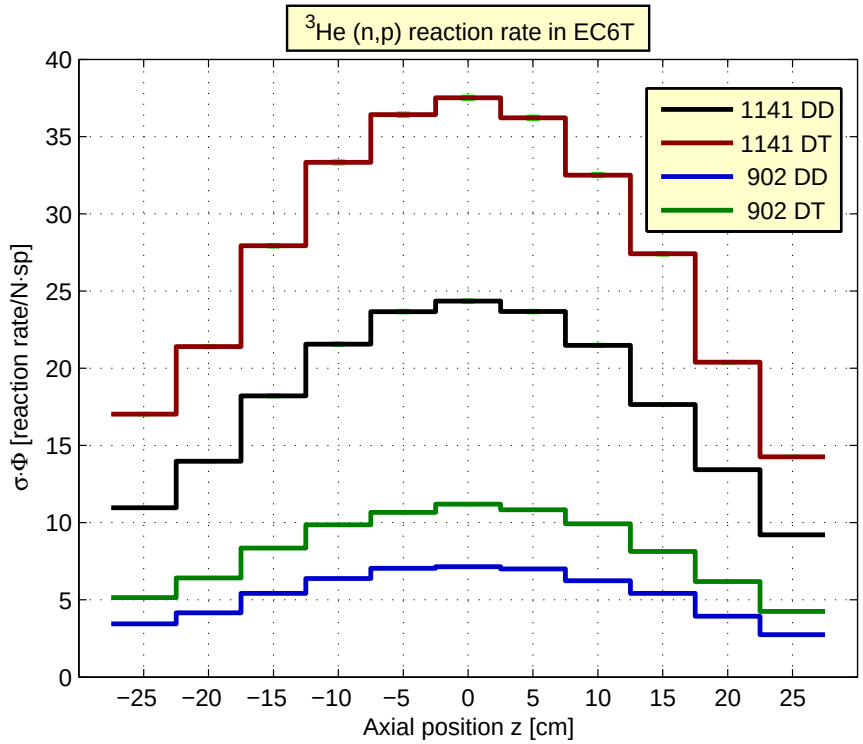

Figure 61. ^{3}He (n,p) reaction rate normalized per atom and source neutron in EC6T experimental channel

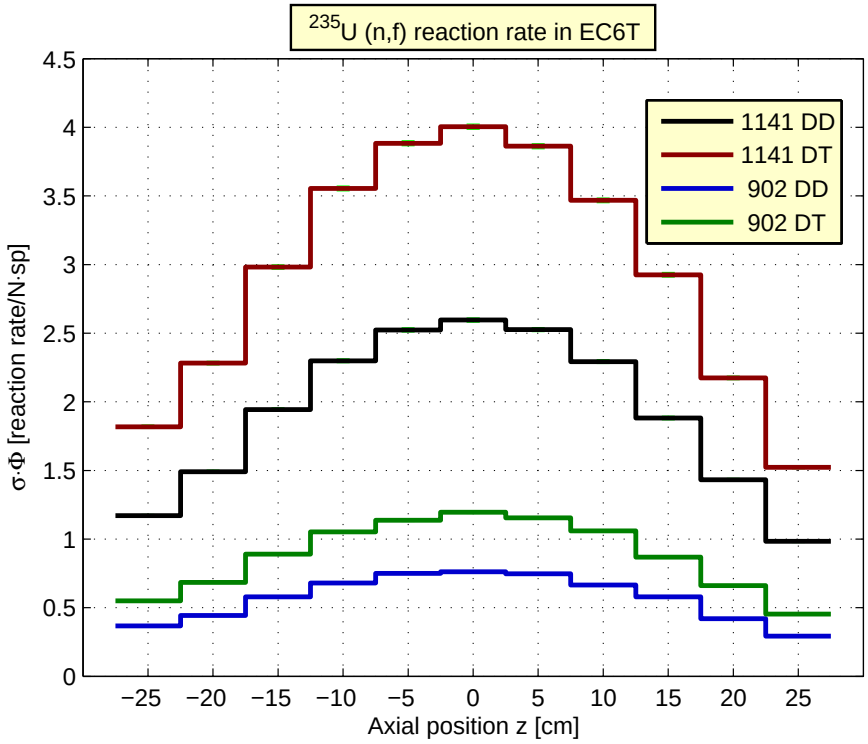

Figure 62. ^{235}U (n,f) reaction rate normalized per atom and source neutron in EC6T experimental channel

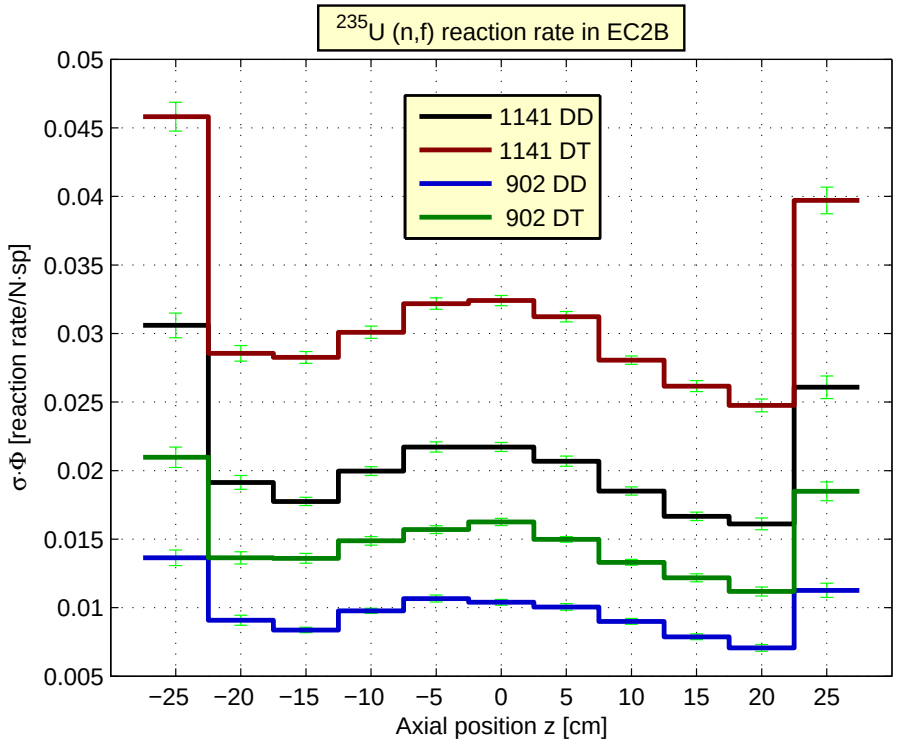

Figure 63. ^{235}U (n,f) reaction rate **normalized** per atom and source neutron in EC2B experimental channel

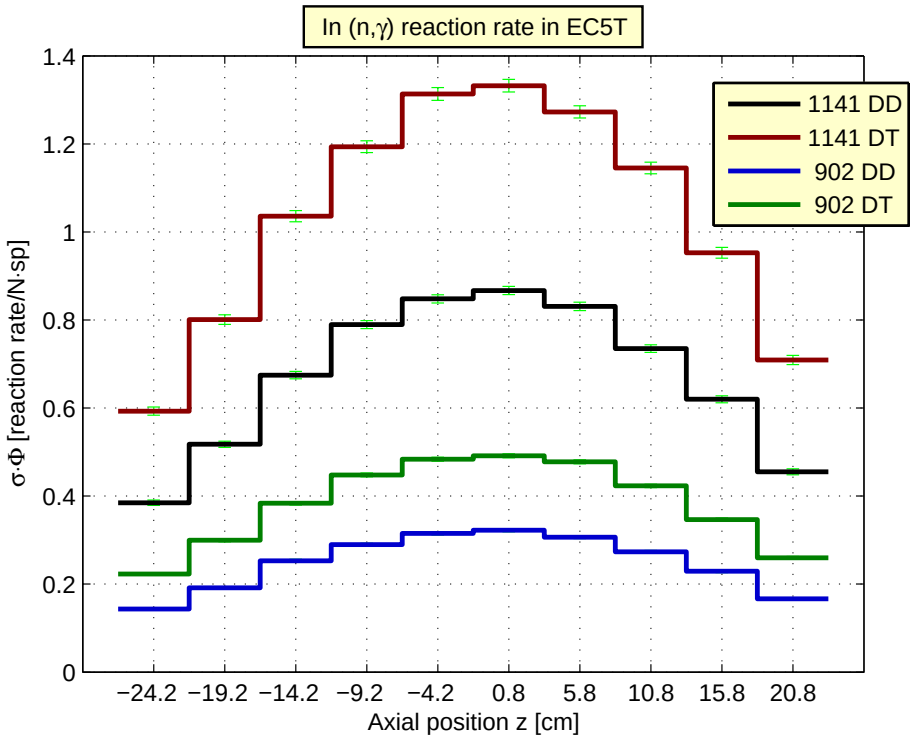

Figure 64. In (n,γ) reaction rate normalized per atom and source neutron in EC5T experimental channel

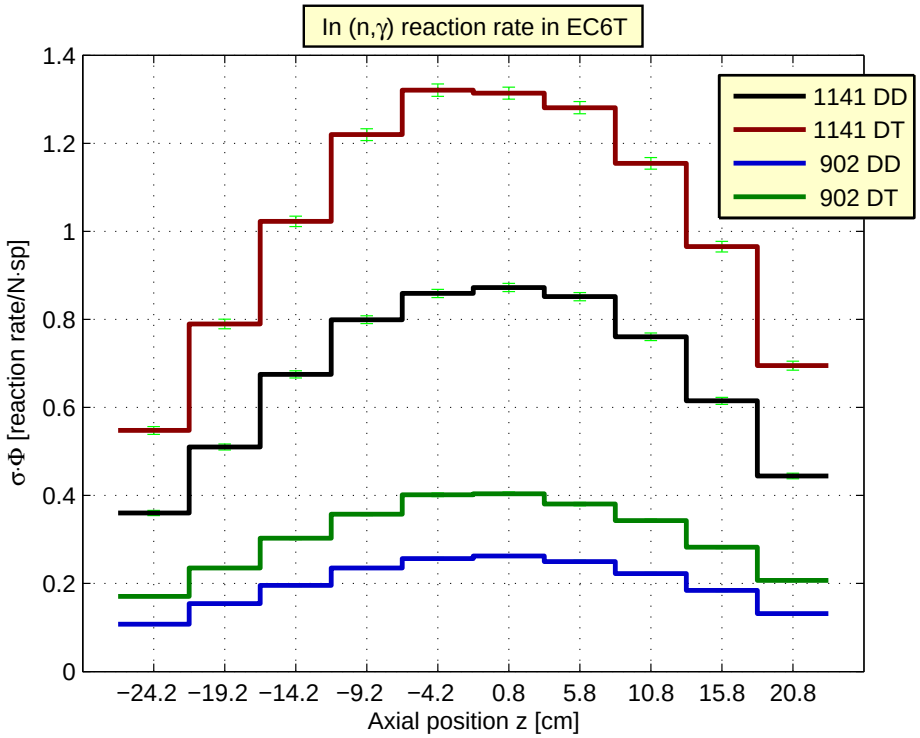

Figure 65. In atom (n,γ) reaction rate normalized per atom and source neutron in EC6T experimental channel

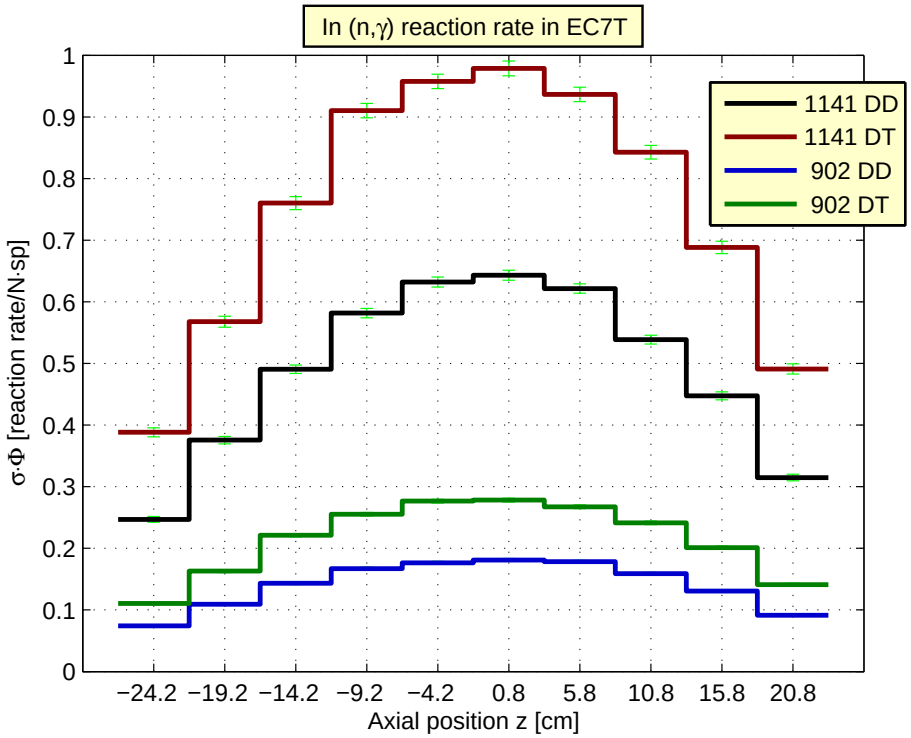

Figure 66. In (n,γ) reaction rate normalized per atom and source neutron in EC7T experimental channel

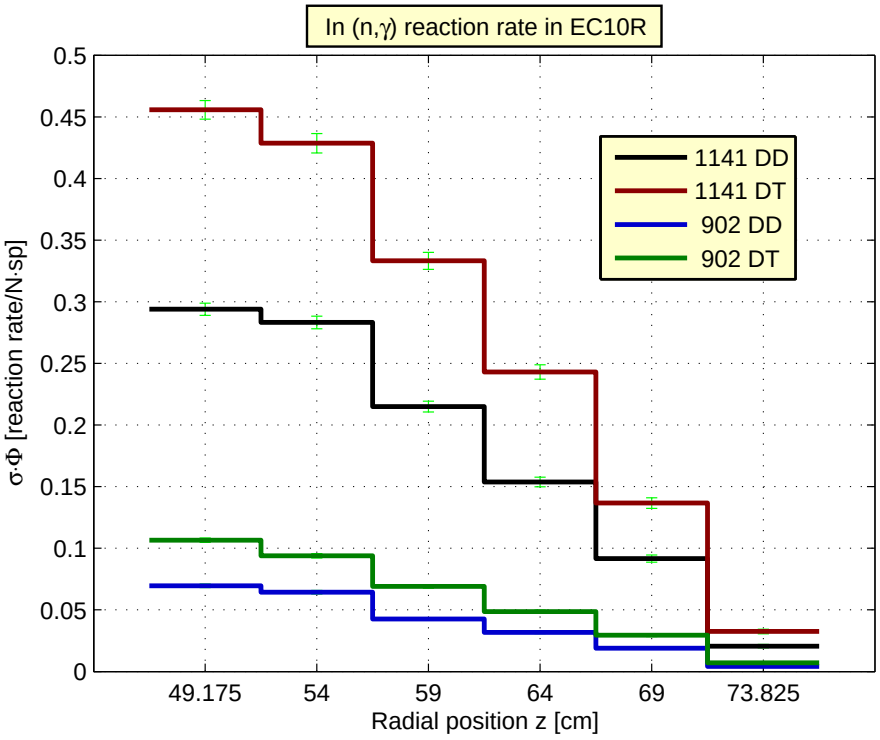

Figure 67. In (n,γ) reaction rate normalized per atom and source neutron in EC10R experimental channel

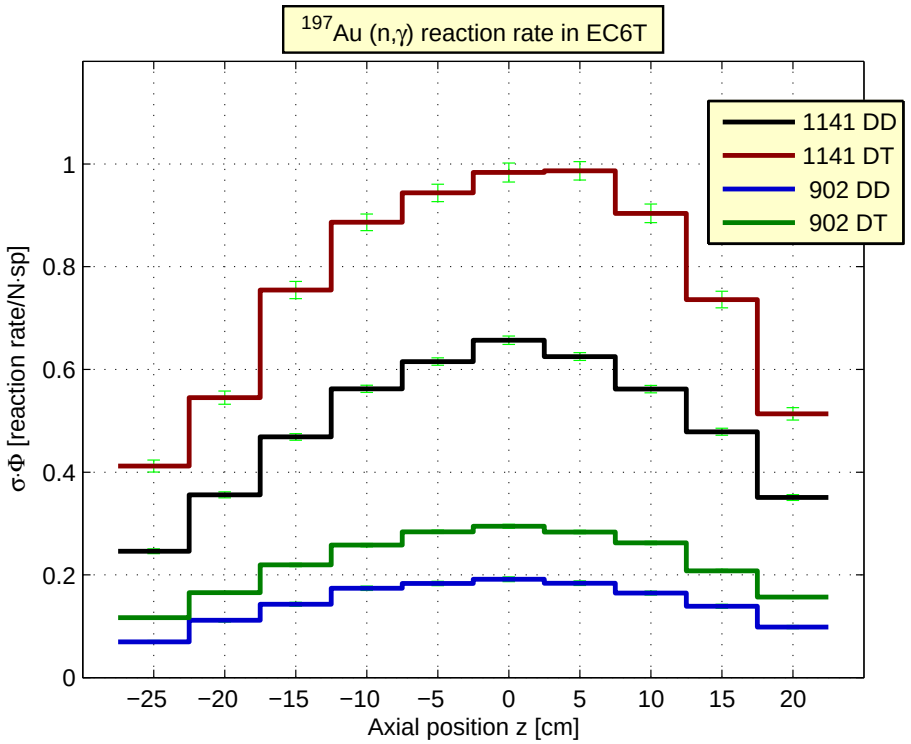

Figure 68. ^{197}Au (n,γ) reaction rate normalized per atom and source neutron and atom in EC6T experimental channel

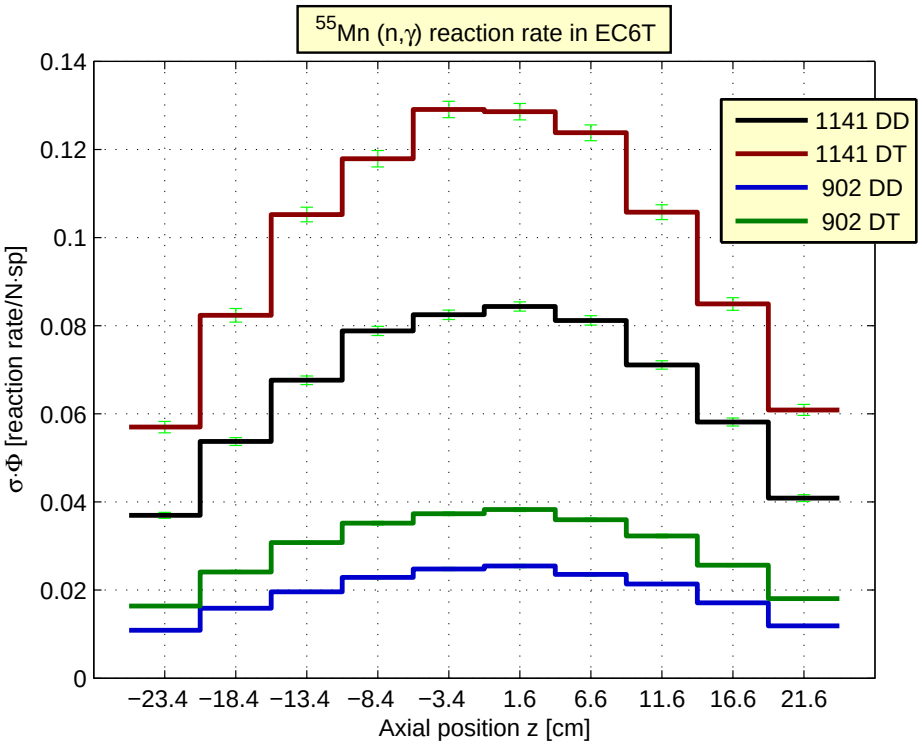

Figure 69. ^{55}Mn(n,γ) reaction rate normalized per atom and source neutron in EC6T experimental channel

Appendix A: Material Approximations

Missing nuclides (indicated in amaranth) and material approximations in MONK9a

Library	Isotope
BINGO JEF-2.2	**^{75}As; ^{209}Bi; ^{204}Pb; ^{66}Zn; ^{67}Zn; ^{68}Zn; ^{70}Zn** Ba modeled as ^{130}Ba, ^{132}Ba, ^{134}Ba, ^{135}Ba, ^{136}Ba, ^{137}Ba and ^{138}Ba ^{63}Cu and ^{65}Cu modeled as Cu ^{206}Pb, ^{207}Pb and ^{208}Pb modeled as Pb Sb modeled as ^{121}Sb and ^{123}Sb ^{28}Si, ^{29}Si and ^{30}Si modeled as Si
DICE JEF-2.2	**S(α,β) graphite; ^{75}As; ^{204}Pb** Ba modeled as ^{130}Ba, ^{132}Ba, ^{134}Ba, ^{135}Ba, ^{136}Ba, ^{137}Ba and ^{138}Ba ^{63}Cu and ^{65}Cu modeled as Cu ^{206}Pb, ^{207}Pb and ^{208}Pb modeled as Pb Sb modeled as ^{121}Sb and ^{123}Sb ^{28}Si, ^{29}Si and ^{30}Si modeled as Si
DICE ENDF/B-VI	**S(α,β) graphite; ^{75}As; ^{204}Pb** Ba modeled as ^{130}Ba, ^{132}Ba, ^{134}Ba, ^{135}Ba, ^{136}Ba, ^{137}Ba and ^{138}Ba Sb modeled as ^{121}Sb and ^{123}Sb ^{28}Si, ^{29}Si and ^{30}Si modeled as Si
WIMS JEF-2.2	**C always modeled by C in graphite** **H always modeled by H in water** **^{75}As; ^{209}Bi; ^{204}Pb; Sb** ^{50}Cr, ^{52}Cr, ^{53}Cr and ^{54}Cr modeled as Cr ^{63}Cu and ^{65}Cu modeled as Cu ^{54}Fe, ^{56}Fe, ^{57}Fe and ^{58}Fe modeled as Fe ^{58}Ni, ^{60}Ni, ^{61}Ni, ^{62}Ni and ^{64}Ni modeled as Ni ^{206}Pb, ^{207}Pb and ^{208}Pb modeled as Pb S modeled as ^{32}S, ^{33}S, ^{34}S and ^{36}S ^{28}Si, ^{29}Si and ^{30}Si modeled as Si

Missing nuclides in MCNPX2.6b, MCNP5, MCNP4c3

Library	Isotope
ENDF/B-VI	**^{204}Pb**
ENDF/B-VI	Ba modeled as ^{138}Ba

Missing data in MCB with JEF-2.2

Library	Data
JEF-2.2	**Update of all S(α,β) scattering functions to 2002 data**
JEF-2.2	Ba modeled as ^{138}Ba

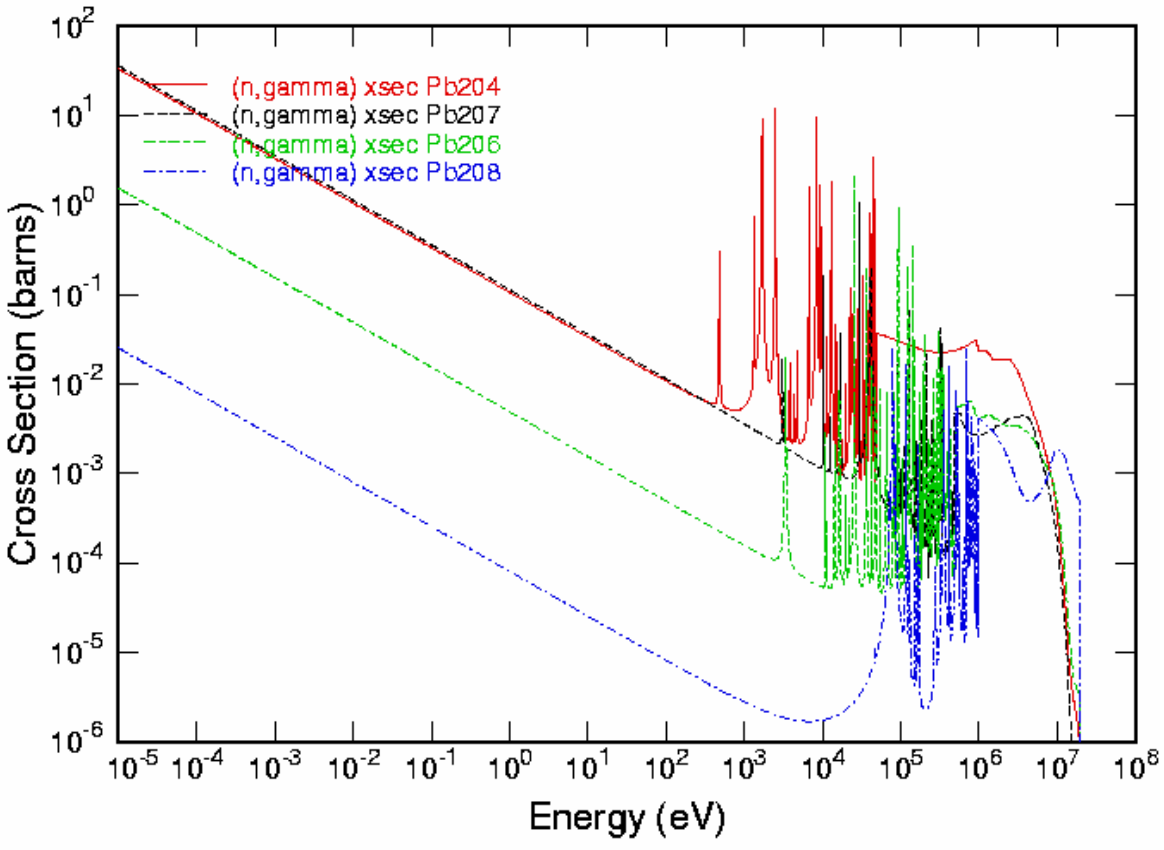

Capture cross sections of lead isotopes

Nuclear Engineering Division
Argonne National Laboratory
9700 South Cass Avenue, Bldg. 208
Argonne, IL 60439-4842

www.anl.gov

A U.S. Department of Energy laboratory managed by UChicago Argonne, LLC